Thesis for the Degree of Licentiate

Electron Transport Studies in Epitaxial Graphene on SiC

Michael Winters

Microwave Electronics Laboratory
Department of Microelectronics and Nanoscience (MC2)
Göteborg, Sweden
November 2013

Electron Transport Studies in Epitaxial Graphene on SiC
MICHAEL WINTERS

Technical Report MC2-267
ISSN 1652-0769

Chalmers University of Technology
Department of Microtechnology and Nanoscience (MC2)
Microwave Electronics Laboratory
SE-412 96 Göteborg, Sweden
Phone:+46 (0) 31 722 1000

Printed by Chalmers Reproservice
Göteborg, Sweden, November 2013

Abstract

Epitaxial graphene on SiC is a novel material which has attracted interest as an electronic material for application in high-frequency devices. This is due in part to the Fermi velocity in graphene $v_f = 1 \cdot 10^8 cm/s$. In a pristine, defect free graphene sheet *in vacuo* at zero temperature, one can expect $v_{sat} = v_f$. Furthermore, the dispersion in graphene $\epsilon_{\mathbf{k}}$ is light-like for graphene monolayers implying that electron transport would behave relativistically. If $v_{sat} = v_f$ could be achieved in the material, then it is theoretically possible to achieve THz performance in long channel devices. Despite the nice theoretical picture, Nature is hardly so forthcoming.

The prime objective of this work is to measure v_{sat} in both as-grown and H-intercalated epitaxial graphene on 4H-SiC and 6H-SiC substrates. Hall measurements indicate that electron transport in H-intercalated material is found to be limited by impurity scattering. In the impurity scattering limit, one can infer a speed limit on the saturated electron velocity of $v_{sat} \approx 2 \cdot 10^7 cm/s$ in epitaxial H-intercalated monolayers. This figure is definitive, as it sets epitaxial graphene on the same level as other semiconductor materials regarding the potential for frequency performance. In as-grown material it is possible to achieve a slightly higher v_{sat}, but the material is generally very non-uniform. Both materials also suffer from the absence of a band-gap making device design intractable.

In order to understand v_{sat} in epitaxial graphene, theoretical and experimental approaches are needed. The consolidated theoretical model of ideal graphene is presented in detail. Graphene's phonon spectrum, electronic band structure, and v_f are derived from first principles. Band structure in bilayer graphene is also addressed and compared to the monolayer case. A possible solution to the band-gap problem is provided in the description of a graphene bilayer with an applied vertical electric field. Useful calculations are also shown regarding the density of states in monolayers and bilayers. The low v_{sat} and high carrier density in epitaxial graphene motivate a semi-classical picture of electron transport via the Boltzmann Transport Equation. Special attention is directed towards the temperature dependence of phonon and long range and scattering mechanisms.

Also described is an experimental characterization of epitaxial graphene layers on SiC. Since graphene monolayers and bilayers demonstrate very different physical properties, a method to accurately determine the number of layers is needed. Layer characterization via Raman spectroscopy is described in the context of theoretical and experimental results. Hall measurements are also shown for as-grown and H-intercalated layers providing valuable information about the mobility μ, sheet resistivity ρ_{sh}, and carrier density n_{sh}. Experimental results obtained from pulsed IV measurements are also shown eventually bringing the discussion back to v_{sat}. The nature of velocity saturation is then described in the context of the temperature dependent transport and scattering processes.

In order to perform electrical measurements on graphene, a robust and minimally invasive fabrication strategy has been developed using both photolithography and electron beam lithography. These processes are designed in such a way as to preserve the quality of the epitaxial layer while providing outstanding contact resistance $\rho_c < 0.2\Omega \cdot mm$. Surface characterization is also performed via Scanning Electron Microscopy (SEM) and Atomic Force Microscopy (AFM) to provide intuition regarding sense morphology. Finally, some potential solutions are motivated from a device context. Future experimental work will implement these with the aim of fabricating a high speed device.

Contents

Preface

Graphene has attracted a tremendous amount of interest within the communities of materials physics, electronics, and condensed matter physics. The discovery of graphene in 2003 opened the investigation of an entirely new class of materials known as 2-dimensional materials. These materials have many interesting properties which may shed light on physical phenomena building from the fundamental properties of solids all the way through the investigation their potential application in high frequency electronics. The aim is to assess epitaxial graphene on SiC for application towards high frequency electronics.

In this investigation, we focus on graphene grown on 4H-SiC and 6H-SiC. This material is of particular interest because it allows for graphene to be grown on commerically available SiC substrates thus providing a route to integration of graphene devices into existing semiconductor fabrication shemes. Furthermore, graphene grown on SiC is a very interesting as the SiC substrate interacts strongly with the electron transport properties in graphene. This also allows for potential engineering solutions such as interface engineering via intercalation, bandgap engineering, and substrate engineering.

The essential core of these investigations focuses on electron transport properties in graphene, and attempts to connect substrate properties and graphene physics to the measured transport characteristics which are relevant for high frequency performance. Electronic test structures and transistors are fabricated on both as-grown and H-intercalated epitaxial graphene. Prior to characterization, the number of graphene layers is assessed in order to gauge the expected band structure and electron transport properties. Characterization techniques include Hall measurements at room temperature and at low temperature, measurements of the contact resistance via the TLM method, DC characterization of test structures, and pulsed IV measurements for the extraction of electron velocity versus electric field curves.

The experimental objective of the work is to measure the electron saturated velocity v_{sat}, electron mobility μ, and carrier density n in epitaxial graphene on SiC as these three parameters establish the fundamental high frequency limits of electron devices. In order to interpret measured results, it is important that these parameters are connected to the underlying physics of electron transport, band structure, phonon scattering and remote phonon scattering via the substrate. The parameter v_{sat} describes the maximum possible velocity that may be achieved in a graphene layer by a charge carrier (electron or hole state). This may be related to the transit frequency f_t, which describes frequency at which the current gain in a device is unity. f_t is one of the primary figures of merit regarding the high frequency performance of a device. f_t can be obtained by nodal admittance analysis of the familiar small signal model of a MOS structure shown below [1, 2].

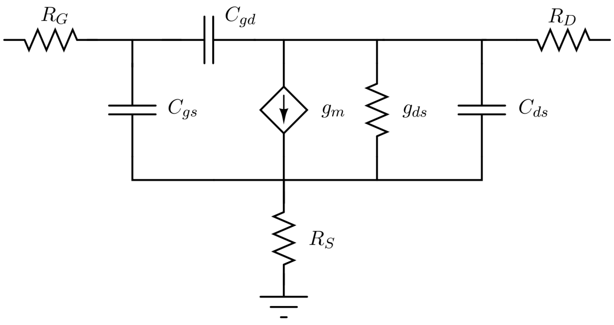

Figure P.1: A simplified small signal equivalent circuit for a general MOS transistor.

The transit frequency can be found as follows.

$$2\pi f_t = \frac{g_m}{(C_{gs} + C_{gd})(1 + g_{ds}R_s) + C_{gd}g_m R_s}$$

Here g_m is the device transconductance, C_{gs} is the gate/source capacitance per unit length, C_{gd} is the gate/drain capacitance per unit length, g_{ds} is the output conductance, and R_s is the extrinsic source resistance. The intrinsic f_t may be obtained by setting $R_s = 0$.

$$2\pi f_t^i = \frac{g_m}{(C_{gs} + C_{gd})}$$

Generally $R_s > 0$ such that $f_t < f_t^i$. Intuitively this is sensible as parasitic effects tend to degrade frequency performance. Here, R_s is connected to the electron mobility μ, sheet resistivity ρ_s, sheet carrier density n, and device geometry. Typically one has that $C_{gs} \gg C_{gd}$ such that the transit frequency is a simple ratio $2\pi f_t = g_m/C_{gs}$. Typically one is dealing with high carrier densities in epitaxial graphene on SiC. In this regime one is typically far from the Dirac Voltage (i.e. the gate voltage at which the carrier density is a minimum) such that the gate capacitance can be treated as constant $C_{gs} \approx C_{ox}l_g$. [3]

$$g_m = \left(\frac{\mu C_{ox}}{l_g}\right) V_{ds}$$

Substitution for f_t yields the the first order device scaling behavior in terms of mobility and gate length. The following applies in the linear region of operation.

$$f_t = \frac{\mu V_{ds}}{2\pi l_g^2}$$

The transit frequency f_t also reaches a fundamental limit due to velocity saturation effects. Expressing f_t in terms of the transit time τ_t, one has.

$$f_t = \frac{1}{2\pi\tau_t} = \frac{v}{2\pi l_g}$$

The transit time τ_t represents the time it takes for a carrier to traverse the gate. Here v is the electron velocity. The maximum f_t occurs at high field, where the v approaches the saturated electron velocity v_{sat}. The saturated electron velocity generally sets the upper limit on the intrinsic transit frequency of a transistor. Another figure of merit for device performance is the frequency at which the unilateral power gain drops to unity f_{max}. The quantity f_{max} is proportional to the intrinsic transit frequency f_t^i. [2]

$$f_{max} = \frac{f_t^i}{\sqrt{4g_{ds}(R_s + R_g) + \frac{4g_m R_g C_{gd}}{C_{gs}+C_{gd}}}}$$

It is important to note here that frequency dependence degrades for higher output conductance g_{ds} and therefore higher carrier density n. This is especially important for epitaxial graphene on SiC as n tends to be very high. The dependence on the source resistance R_s suggests that low mobility will also tend to degrade device performance.

From the small signal model one finds that device performance is critically dependent on transport properties. Good high frequency performance is expected from devices which have high v_{sat}, high μ, and low n. The physics of v_{sat} is ultimately related to the phonon spectrum of the material and the density of impurities in the graphene. Mobility μ may also be understood in terms of Boltzmann Transport analysis of phonon and impurity scattering. The carrier density n is related both to the fundamental band structure of the material and the relative uniformity and purity of graphene layers. Another fundamental problem that presents major difficulties regarding epitaxial graphene transistors on SiC is the weak modulation of carrier density by gate biasing. This can be attributed to two facts. First, graphene lacks a band gap, such that fairly high carrier densities can be expected even at the Dirac point for finite temperature. Second, all epitaxial layers demonstrate very high doping such that high gate voltages are needed in order to get any significant modulation at all.

In the context of devices, this manifests as a low I_{on}/I_{off} and transconductance g_m. Typical I_{on}/I_{off} ratios for monolayer graphene epitaxial graphene on SiC are about 7 [4, 5]. However, significant improvements can be achieved by opening a bandgap in bi-layer graphene layers by the application of a vertical electric field. It is therefore very important to have a scheme for characterizing the number of layers in epitaxial graphene non-destructively. Characterization by Raman spectroscopy is shown in Chapter 3, while the theoretical basis of the bilayer bandgap is addressed in extensive detail in Chapter 2. Lastly, the one redeeming feature of SiC and perhaps the sole motivation to continue work on epitaxial graphene on SiC lies in the fact that it is possible to do wafer scale processing on commerically available SiC substrates. [6, 7] This is an extreme luxury, as working with exfoliated flakes is very difficult in an laboratory environment. If the major issues are overcome via creative engineering, epitaxial material on SiC provides an avenue to high throughput processing of graphene devices using existing processing technology.

This work attempts to walk on fine boundary which separates the physical theory of the solid state from electronics engineering. Chapter 1 presents a summary of the physics of electron transport in graphene and attempts to provide a cursory yet informative picture of why graphene is of such interest. A variety of topics are considered including, the reciprocal lattice of graphene, energy and momentum considerations, graphene's phonon spectrum, and the electronic band structure of monolayer graphene. These topics serve as the fundamental building blocks of understanding electron physics in graphene. Chapter 2 serves as an extension to Chapter 1 and attempts to generalize the physics presented in Chapter 1 to that of a bilayer. Furthermore, the physics of electron transport is also reviewed in the context of graphene, and the Boltzmann transport equation is solved for the case of acoustic phonon scattering and charged impurity scattering. Chapter 3 describes how these results may be applied to epitaxial graphene in practice. A wide variety of measurements are presented from spectroscopic data, to mobility and velocity saturation data. The physics of the previous chapters is grounded in measurement in order to provide a clear understanding of the scope of possibilities for graphene based electronics. Finally, Chapter 4 summarizes the processing technology that has been developed for the fabrication of epitaxial graphene devices. All of the measurements and data analysis here presented were performed using Python and C, and a great deal of work has gone into solving the various computational problems presented by measurement data.

It is hoped that this treatise will be of value to the theorist, the experimentalist, and the engineer alike. For this reason tremendous effort has gone into reducing the theoretical complexity such that measurements can be understood without destroying the fundamental physics which motivates our observations. Lastly, this work is by no means complete, and I have attempted to select with utmost care from the vast body of graphene literature those ingredients which are essential for understanding graphene based electron devices in terms of the material presented here. Although the theoretical work presented is essential in order to understand the origins of the underlying limitations it should not detract from the experimental work itself.

Chapter 1

Fundamental Principles

Graphene is a two dimensional allotrope of Carbon atoms in a hexagonal arrangement as shown in Fig 1.1. The material properties of such a system may be entirely attributed to this two-dimensional periodic structure. The lattice structure of graphene is shown below, along with the primitive cell denoted by the basis vectors $\mathbf{a_1}$ and $\mathbf{a_2}$. Also shown is the interatomic spacing a_0. The lattice structure of graphene contains *two* carbon atoms per unit cell which form two sublattices. The sublattice of a atoms is shown in black, and the sublattice of b atoms is shown in grey.

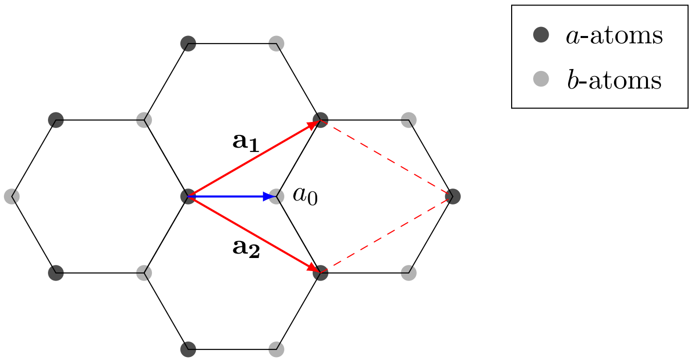

Figure 1.1: A diagram showing the essential structure of graphene in real space. The a and b sublattices are shown in grey and black respectively. The interatomic spacing is shown in blue and the primitive cell is shown in red.

By plane geometry the primitive lattice vectors can be derived [8]:

$$\mathbf{a_1} = a_0 \left[\frac{3}{2}, \frac{\sqrt{3}}{2}\right] \qquad \mathbf{a_2} = a_0 \left[\frac{3}{2}, -\frac{\sqrt{3}}{2}\right] \tag{1.1}$$

By the Pythagorean theorem, the magnitude of the primitive lattice vectors is given by the following

$$|\mathbf{a_1}| = |\mathbf{a_2}| = a_0\sqrt{3} \tag{1.2}$$

It is important to note that the Bravais lattice of the honeycomb lattice is not given by the basis vectors connecting nearest neighbors, but is instead given by the next to nearest neighbors. The Bravais lattice is hexagonal, and its unit cell is shown in red. Because the lattice is periodic, it follows that any physical property of the lattice $f(\mathbf{r})$ will inherit its periodicity. Mathematically, this means that $f(\mathbf{r})$ is invariant under translation.

$$f(\mathbf{r}) = f(\mathbf{r} + \mathbf{R}) \tag{1.3}$$

Here, the vector $\mathbf{R}$ is not arbitrary as it must represent the periodicity of the lattice. It is built via an integer sum over the primitive lattice vectors.

$$\mathbf{R} = \sum_i n_i \mathbf{a_i} \tag{1.4}$$

The inter-atomic spacing has been measured to be 1.42Å and is denoted a_0, and the magnitude of the corresponding lattice vectors $\mathbf{a_1}$ and $\mathbf{a_2}$ is 2.46Å. There are many techniques to arrive at these kinds of figures including, x-ray diffraction (XRD) [9], transmission electron microscopy (TEM) [10], Scanning tunneling microscopy (STM) [11], atomic force microscopy (AFM) etc.

1.1 The Reciprocal Lattice

In the previous section, it was stated that a physical property of the lattice $f(\mathbf{r})$ inherits the periodicity of the lattice. Any periodic function in space may be described a wavelength. In a lattice of atoms, the ionic cores may also be thought of as being described by a two dimensional periodic wave. The primitive lattice vectors $\mathbf{a_1}$ and $\mathbf{a_2}$ define crystal planes within the lattice. The lattice wavelengths λ_i are simply distances between crystal planes and can be calculated from the primitive lattice vectors. The construction of the lattice wavevectors from crystal planes is shown below.

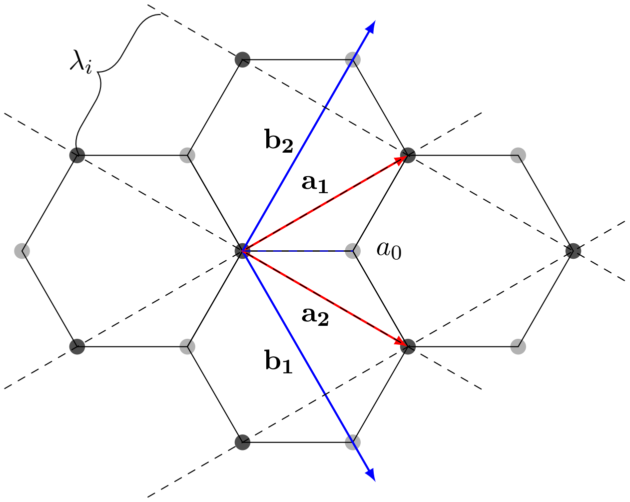

Figure 1.2: A diagram showing the primitive (red) and reciprocal (blue) lattice vectors in real space. Lattice planes (dashed) are also shown such that the directions of the reciprocal lattice vectors are intuitive. The associated reciprocal lattices wavelength is given by the distance between lattice planes.

A wave description of the lattice based on its crystal planes is equally tenable as the description by the primitive lattice vectors. This can be done by recognizing that the lattice planes define a spatial frequency defined by the lattice wavevectors $\mathbf{b_i}$. These vectors point in the direction of propagation of the wave, and its magnitude $|\mathbf{b}|$ is known as the wavenumber. The lattice wavenumbers may be related to lattice wavelengths in the following manner.

$$|\mathbf{b_i}| = \frac{2\pi}{\lambda_i} \tag{1.5}$$

Here the lattice wavelengths λ_i are simply the distances between crystal places. One can naively calculate wavenumbers corresponding the primitive lattice vectors in graphene. The wavelengths may be obtained from the primitive lattice vectors by geometry.

$$\lambda_i = |\mathbf{a_i} \times \hat{\mathbf{a_j}}| \tag{1.6}$$

Thus, for the graphene lattice, one has the following.

$$\begin{aligned} \lambda_1 = \lambda_2 &= \frac{3a_0}{2} \\ |\mathbf{b_1}| = |\mathbf{b_2}| &= \frac{4\pi}{3a_0} \end{aligned} \tag{1.7}$$

The vectors $\mathbf{b_1}$ and $\mathbf{b_2}$ are known as the *reciprocal lattice vectors.* The magnitudes of these vectors have units of *inverse* length. At this point, their magnitude is known, but their direction remains to be found. The direction of the wavevector is defined as the direction which is *perpendicular to lines or planes of surfaces of constant phase.* The surfaces of constant phase in a lattice are simply the crystal planes. Because the lattice vectors $\mathbf{a_1}$ and $\mathbf{a_2}$ define lines or planes through lattice points, their associate wavevectors should be normal to them. In this way, one begins with *unit* primitive vectors.

$$\hat{\mathbf{a}}_1 = \left[\frac{\sqrt{3}}{2}, \frac{1}{2}\right] \quad \hat{\mathbf{a}}_2 = \left[\frac{\sqrt{3}}{2}, -\frac{1}{2}\right] \tag{1.8}$$

Rotating these by 90° and multiplying by the wavenumber yields the wavevectors associated with the primitive lattice vectors.

$$\mathbf{b_1} = \frac{4\pi}{3a_0}\left[\frac{1}{2}, \frac{\sqrt{3}}{2}\right] \quad \mathbf{b_2} = \frac{4\pi}{3a_0}\left[\frac{1}{2}, -\frac{\sqrt{3}}{2}\right] \tag{1.9}$$

In summary, lattice wavevectors have been defined which describe the spatial frequency of the lattice on the basis of spacing λ_i of crystal planes. In the same way that the primitive lattice vectors build up the lattice in terms of the positions of atoms, the reciprocal lattice vectors build a *reciprocal lattice* in terms of the spacings of crystal planes. The primitive lattice represents position space, while the reciprocal lattice represents momentum space (**k**-space). [*] The vectors of the reciprocal lattice are related to momentum and energy in our crystal structure and will be used extensively in derivations of the electronic band structure. The reciprocal lattice is also invariant under translation such that for any physical property in **k**-space $g(\mathbf{k})$. [12]

$$g(\mathbf{k}) = g(\mathbf{k} + \mathbf{G}) \tag{1.10}$$

Where the translation vector **G** is the integer sum of the reciprocal lattice vectors.

$$\mathbf{G} = \sum_i n_i \mathbf{b}_i \tag{1.11}$$

1.1.1 The Reciprocal Lattice and Brillouin Zone in Graphene

Fig. 1.3 shows the reciprocal lattice points of graphene, as well as its reciprocal lattice vectors. Also is shown the primitive cell (blue) of the reciprocal lattice and its first Brillouin zone (light blue) in the reciprocal lattice as well as the irreducible path (green) in the Brillouin zone. [†] The diagram may be thought of as living in **k**-*space* where where $\hat{\mathbf{k_x}}$ and $\hat{\mathbf{k_y}}$ serving as unit vectors in the space. It should be stated at the outset that two points in **k**-space are considered equivalent if they can be reached by translation via a reciprocal lattice vector.

---

[*] This description is designed in order to introduce the reciprocal lattice in an intuitive way. From a purely mathematical perspective, the reciprocal lattice is the Fourier transform of the primitive lattice.

[†] In a later section, the band structure of graphene will be plotted along the irreducible path.

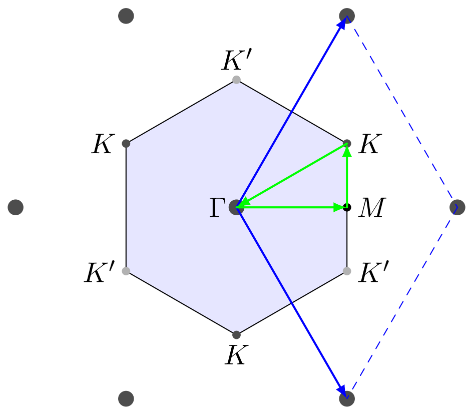

Figure 1.3: A diagram showing the reciprocal lattice in graphene along with the first Brillouin zone (shaded blue). Special *high symmetry points* are also shown which will become important in later derivations. The *irreducible path* also appears in green.

The importance of the Brillouin zone arises when one considers the elastic reflection of waves from a periodic structure. This wave could represent a photon, or an electron via the deBroglie hypothesis. The Bragg reflection hypothesis states that reflection from a periodic structure only occurs when the the incident wave **k** and reflected wave **k**′ interfere constructively. Constructive interference only occurs when the difference between the incident and reflected waves is equal to a reciprocal lattice vector **G**.

$$\mathbf{\Delta k} = \mathbf{k} - \mathbf{k}' = \mathbf{G} \tag{1.12}$$

In other words, the phase difference between incident and reflected waves is zero only when the path of reflection reflects the periodicity of lattice planes. The relation above is clear as **G** is a reciprocal lattice vector. It represents a wavevector that is associated with the periodicity of lattice planes by definition. Furthermore, An elastic scattering event is one in which the direction of the momentum is changed, yet the magnitude remains constant.

$$|\mathbf{k}| = |\mathbf{k}'| \tag{1.13}$$

Combining these two conditions, the conditions of elastic reflection of a wave from a periodic structure may be summarized as follows. [12]

$$\mathbf{k} \cdot \mathbf{G} = \frac{1}{2}|\mathbf{G}|^2 \tag{1.14}$$

The above relation is simply a vector definition of the familiar one dimensional Bragg condition $n\lambda = 2d\cos\theta$ where d is the lattice spacing, λ is the wavelength of the incident beam, and θ is the angle of incidence with respect to the normal. Geometrically, the above relation describes boundaries of volumes in **k**-space. These volumes are Brillouin zones. The smallest of these volumes is known as the first Brillouin zone. Although the notion of Brillouin zones first arises in an analysis of Bragg reflections, it appears ubiquitously in the physical theory of solids.

The Brillouin zone of graphene has several points of interest which will become important in the analysis of its band structure and in the discussion of its electronic properties. The points of symmetry are listed below in Table 1.1.

Table 1.1: A list of the special points in the Brillouin Zone along with their associated vector in **k**-space. The points K and K' are not equivalent as one cannot reach K' from K via translation by a reciprocal lattice vector. The Γ point is typically referred to as the *zone center.*

Point	K	K'	M	Γ
k-vector	$\frac{2\pi}{3a_0}\left[1, \frac{1}{\sqrt{3}}\right]$	$\frac{2\pi}{3a_0}\left[1, -\frac{1}{\sqrt{3}}\right]$	$\frac{2\pi}{3a_0}[1, 0]$	$[0, 0]$

From the diagram, one can see a fundamental difference between the points labeled K and K'. The points labeled K are considered to be equivalent as one can move between K points by translation via reciprocal lattice vector. Therefore any physical property of the lattice will be equivalent at the K points. * However, one cannot however translate from K to K' via a reciprocal lattice vector, such that these points are inequivalent giving rise to the possibility of different physics at K and K'. This difference between the points K and K' will ultimately build a degeneracy into the band structure of graphene known as *valley isospin.*

1.2 Lattice Dynamics: Graphene's Phonon Spectrum

> *Physics is that subset of human experience which can be reduced to coupled harmonic oscillators.*
> -Michael Peskin

It is useful to consider lattice dynamics in graphene. Generally, the lattice will not be static, and atoms may move together in a harmonic fashion. Lattice vibrations of a harmonic nature are known as *phonons.* Later, we will see that lattice vibrations can influence the transport properties in graphene and will give rise to temperature dependent transport phenomena. Phonons also play a major role in characterizing graphene both in terms of defects, and in terms of the number of layers. [13]

The graphene honeycomb lattice is shown again below along with its primitive basis vectors $\mathbf{a_1}$ and $\mathbf{a_2}$ along with its nearest neighbor vectors labeled $\delta_\mathbf{0}$, $\delta_\mathbf{1}$, and $\delta_\mathbf{2}$.

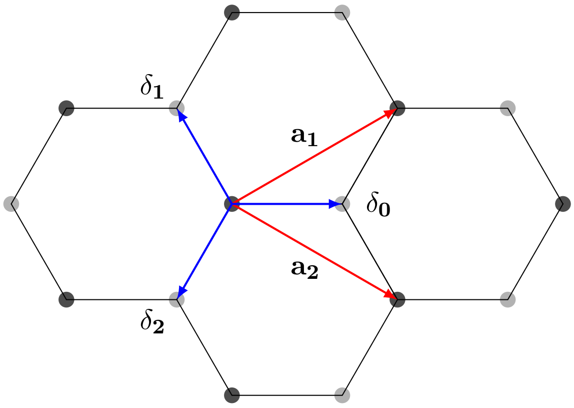

Figure 1.4: A diagram of the real space lattice in graphene with the primitive lattice vectors (red) and the nearest neighbor vectors $\delta_\mathbf{n}$ (blue). The nearest neighbor vectors will appear in both the calculation of the phonon spectrum and in the calculation of the band structure.

The nearest neighbor vectors should be understood in the context of sp_2 hybridization as discussed in a later section. They may be calculated as follows. [14, 15]

$$\delta_\mathbf{0} = a_0\,[1,0] \qquad \delta_\mathbf{1} = a_0\left[-\frac{1}{2},\frac{\sqrt{3}}{2}\right] \qquad \delta_\mathbf{2} = a_0\left[-\frac{1}{2},-\frac{\sqrt{3}}{2}\right] \tag{1.15}$$

The argument for phonons begins by considering the geometry of graphene which is dictated by the chemistry of bonding. When an atom i in the primitive cell is displaced by a small distance U_i it will

---

[*] The same holds for translation between the K' points.

experience a restoring force from its neighbors which tends to bring it back into its equilibrium position. If the interatomic restoring forces $\mathbb{G}$ are treated as harmonic then they may be modeled as massless springs which connect the atoms of the lattice. In this case the equation of motion for collective harmonic excitations of the lattice is as follows.

$$M_i \frac{d^2\mathbf{U}}{dt^2} = -\mathbb{G} \cdot \mathbf{U} \tag{1.16}$$

Here the vector $\mathbf{U}$ represents the displacements of the atoms in the unit cell and their nearest neighbors. In analogy to Hooke's Law $\mathbb{G}$, should be the product of a constant (α) and all of the displacements in the system. In momentum space, one has the following.

$$\mathbb{G}_{ij} = \alpha_{ij}(U_i - U_j e^{i\mathbf{q}\cdot\delta_{ij}}) \tag{1.17}$$

Here δ is the vector defining the relative distance between atoms i and j. We expect that the motion of the atoms is harmonic, such that for the i-th atom one has $U_i = e^{i\omega t}$. By substitution, one has the following for the i-th row of the equation of motion. [12, 16]

$$\omega^2 M_i U_i = -\sum_j \alpha_{ij}(U_i - U_j e^{i\mathbf{q}\cdot\delta}) \tag{1.18}$$

The above equation describes the i-th row of a matrix such that, the problem of finding the frequencies of lattice oscillations is ultimately an eigenvalue problem. The dynamical matrix takes the following form.

$$\begin{vmatrix} n\alpha_{11} - M_i\omega^2 & \dots & e^{i\mathbf{q}\cdot\delta_n} \\ \vdots & \ddots & \vdots \\ e^{-i\mathbf{q}\cdot\delta_n} & \dots & n\alpha_{nn} - M_i\omega^2 \end{vmatrix} = 0 \tag{1.19}$$

In the case of graphene, is convenient to solve the eigenvalue problem in term of the a and b sublattices. In order to get the full phonon spectrum, we must include both sublattices. Because the graphene unit cell has two atoms, one expects there to be two modes of oscillation per degree of freedom. In the xy plane, we can expect two *acoustic* branches in which neighboring atoms move in the same direction, and two *optical branches* in which neighboring atoms move in opposite directions. The acoustic modes will be denoted LA and TA for the transverse and longitudinal polarizations, and the optical modes will be denoted LO and TO in the same manner. In graphene we can also expect two more modes (labeled ZA and ZO) corresponding to atomic oscillations *perpendicular* to the xy plane. This gives a total of *six* phonon branches. For every value $\mathbf{q}$ in the first Brillouin zone, there will be six energies, each corresponding to one of the six modes of vibration [15].

First taking the z phonons, one places the a sublattice and b sublattices themselves on the diagonal, and the relative displacements on the off diagonal. For the relative displacements one must sum over all of the nearest neighbors. One then has for the Dynamical equation.[14]

$$\begin{vmatrix} 3\alpha_z - \omega^2 & \sum_n e^{i\mathbf{q}\cdot\delta_n} \\ \sum_n e^{-i\mathbf{q}\cdot\delta_n} & 3\alpha_z - \omega^2 \end{vmatrix} = 0 \tag{1.20}$$

Here the mass constant M of each carbon atom is identical, such that it can be absorbed into α_z. For the xy phonons, the situation is similar. One has the dynamical equation.

$$\begin{vmatrix} 3\alpha - \omega^2 & 0 & \beta\sum_n e^{i\mathbf{q}\cdot\delta_n} & \beta\sum_n e^{i\mathbf{q}\cdot\delta_n^r} \\ 0 & 3\alpha - \omega^2 & \beta\sum_n e^{i\mathbf{q}\cdot\delta_n^r} & \beta\sum_n e^{i\mathbf{q}\cdot\delta_n} \\ \beta\sum_n e^{-i\mathbf{q}\cdot\delta_n} & \beta\sum_n e^{-i\mathbf{q}\cdot\delta_n^r} & 3\alpha - \omega^2 & 0 \\ \beta\sum_n e^{-i\mathbf{q}\cdot\delta_n^r} & \beta\sum_n e^{-i\mathbf{q}\cdot\delta_n} & 0 & 3\alpha - \omega^2 \end{vmatrix} = 0 \tag{1.21}$$

Here the term involving δ^r is a peculiarity to the sublattice approach. It indicates is symmetric by a rotation of $2\pi/3$ or a reflection about the y-axis. It arises due to the fact that the lattice is symmetric under rotation by $2\pi/3$ such that two of the relative position vectors are considered equivalent. [14] δ^r is constructed by taking the inverse of the y value of the relative position vectors. [*]

---

[*] Notice how this operation only affects the position vectors with y components δ_1 and δ_2

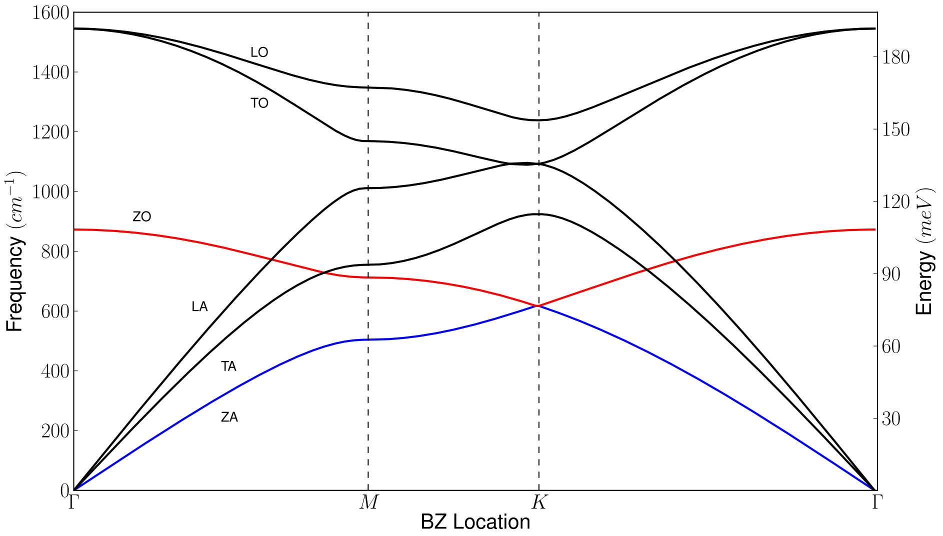

Figure 1.5: A plot of the graphene phonon spectrum as calculated by Eq. 1.21 simulated in Python. In this simple model only nearest neighbor coupling is considered. More accurate models may be obtained by including more neighbors. The four in-plane modes (LA, TA, LO, TO)are shown in black while the out of plane acoustic (ZA) and optical (ZO) modes are shown in blue and red respectively. [14, 15, 17]

It should be noted that the force constants have been measured to be $\alpha_z = -1.270e5$, $\alpha = -3.980e5$, and $\beta = -1.132e5$ respectively [14, 15]. Fig 1.5 shows the phonon spectrum in graphene as calculated via the above eigenvalue equations for $\mathbf{q}$ as one traverses the path of the irreducible zone previously introduced in Fig 1.3. [*]

1.3 Bloch Waves and Periodic Potentials

No discussion on the topic of periodic structures could be complete without an introductory description of the Bloch theorem. The essence of the Bloch theorem concerns the behavior of electron wavefunctions in the potential of a periodic structure. Later the Bloch theorem will be applied to the problem of electrons in graphene. It is important to cite the fundamental theorem of periodic structures.

> All physical properties of a periodic structure inherit the periodicity of that structure.

Since the length scales of periodicity in crystals is on the order of Ångstroms (and thus is less the deBroglie wavelength of electrons), a quantum mechanical approach is needed. The time independent Schrödinger equation expresses the notion of classical energy conservation in a quantum mechanical context. It takes the following form.

$$\mathcal{H}\left|\psi(\mathbf{r})\right\rangle = \left[\frac{\mathcal{P}^2}{2m} + V(\mathbf{r})\right]\left|\psi(\mathbf{r})\right\rangle = E\left|\psi(\mathbf{r})\right\rangle \tag{1.22}$$

---

[*] A more rigorous derivation of the phonon spectrum may is available in [15]. The nearest neighbor result is identical to what is presented above. Higher order simulations are also presented (including second, third and fourth nearest neighbors) and discussed in the context of deviations from the nearest neighbor case.

Here $\mathcal{P} = -i\hbar\nabla$ is the quantum momentum operator, and $|\psi(\mathbf{r})\rangle$ is the eigenfunction of an electron. [*] Consider an arbitrary periodic structure with a lattice defined by the primitive lattice vectors $\mathbf{a_i}$. For a lattice vector $\mathbf{R}$ the potential energy of a periodic structure must satisfy the following relation.

$$V(\mathbf{r}+\mathbf{R}) = V(\mathbf{r}) \tag{1.23}$$

At this point it is useful to introduce the *translation operator* $\mathcal{T}$. Let $\mathcal{T}_R$ describe a translation along the vector $\mathbf{R}$

$$\mathcal{T}_R\,|\psi(\mathbf{r})\rangle = |\psi(\mathbf{r}+\mathbf{R})\rangle \tag{1.24}$$

In the case of a periodic potential, the commutator of $\mathcal{H}$ and $\mathcal{T}$ is zero.

$$[\mathcal{T}_R, \mathcal{H}] = [\mathcal{T}_R\mathcal{H}(\mathbf{r}) - \mathcal{H}(\mathbf{r})\mathcal{T}_R]\,|\psi(\mathbf{r})\rangle = 0 \tag{1.25}$$

Therefore eigenfunctions of $\mathcal{T}_R$ are simultaneously eigenfunctions of $\mathcal{H}$. In the end, one is interested in two things, the eigenfunctions of $\mathcal{T}_R$ and the energy eigenvalues of $\mathcal{H}$. *The eigenvalues of $\mathcal{T}_R$ are known as Bloch waves, and their corresponding energy eigenvalues of $\mathcal{H}$ generate a band structure.* The eigenvalues of $\mathcal{T}_R$ are found by projection of $|\psi\rangle$ onto the momentum basis.

$$\mathcal{T}_R\,|\psi\rangle = \mathcal{T}_R \sum_q |\mathbf{q}\rangle\,\langle\mathbf{q}|\,\mathbf{r}\rangle \tag{1.26}$$

Here $|\mathbf{q}\rangle$ is simply the basis of momentum eigenstates (i.e. plane waves). Setting the inner product to c_q and noting that $|\mathbf{q}\rangle = e^{i\mathbf{q}\cdot\mathbf{r}}$ one has the following.

$$\mathcal{T}_R\,|\psi\rangle = \mathcal{T}_R \sum_q c_q e^{i\mathbf{q}\cdot\mathbf{r}} = \sum_q c_q e^{i\mathbf{q}\cdot\mathbf{r}} e^{i\mathbf{q}\cdot\mathbf{R}} = t_R \sum_q c_q e^{i\mathbf{q}\cdot\mathbf{r}} \tag{1.27}$$

Here t_R is the eigenvalue of the translation operator and therefore must be a constant.

$$t_R = e^{i\mathbf{q}\cdot\mathbf{R}} = \text{const} \tag{1.28}$$

By evaluating $\mathbf{q} = \mathbf{G} + \mathbf{k}$ one finds the argument of the exponent becomes $2\pi n + \mathbf{k}$. Here the identity $\mathbf{R}\cdot\mathbf{G} = 2\pi n$ is applied where $\mathbf{G}$ is a recipoical lattice vector. The eigenvalue is then $t_R = e^{i\mathbf{k}\cdot\mathbf{R}}$. It is important to note that different $\mathbf{G}$ vectors yield the same eigenvalue (i.e. t_R is degenerate). The corresponding *eigenvector* is then found by substitution of $\mathbf{G}+\mathbf{k}$ for $\mathbf{q}$ in Eq 1.27.

$$\mathcal{T}_R\,|\psi\rangle = t_R e^{i\mathbf{k}\cdot\mathbf{r}} \left\{ \sum_{\mathbf{G}} c_{\mathbf{G}+\mathbf{k}} e^{i\mathbf{G}\cdot\mathbf{r}} \right\} = t_R e^{i\mathbf{k}\cdot\mathbf{r}}\,|u_k(\mathbf{r})\rangle \tag{1.29}$$

Such that one has the following

$$\begin{gathered} |\psi\rangle = e^{i\mathbf{k}\cdot\mathbf{r}}\,|u_k(\mathbf{r})\rangle \\ u_k(\mathbf{r}) = \sum_{\mathbf{G}} c_{\mathbf{G}+\mathbf{k}} e^{i\mathbf{G}\cdot\mathbf{r}} \end{gathered} \tag{1.30}$$

The values of $\mathbf{k}$ which are important are those which are uniquely determined (i.e. those first Brillouin zone). By construction $u_k(\mathbf{r})$ is periodic in both $\mathbf{G}$ and $\mathbf{R}$. Finally, the action of the translation operator on $|\psi\rangle$ is summarized as follows.

$$\mathcal{T}_R\,|\psi(\mathbf{r})\rangle = e^{i\mathbf{k}\cdot\mathbf{R}}\,|\psi(\mathbf{r})\rangle \tag{1.31}$$

Equations 1.30 and 1.31 are two different statements of the famous Bloch theorem. Physically, they state that the wavefunctions of a periodic potential inherit the periodicity of the potential.

---

[*] This definition of the momentum operation becomes clear when considering its action on a plane wave. $\mathcal{P}\,|e^{i\mathbf{k}\cdot\mathbf{r}}\rangle = -i\hbar\nabla\,|e^{i\mathbf{k}\cdot\mathbf{r}}\rangle = \hbar\sum k_i\hat{\mathbf{x}}_{\mathbf{i}}\,|e^{i\mathbf{k}\cdot\mathbf{r}}\rangle = \mathbf{p}\,|e^{i\mathbf{k}\cdot\mathbf{r}}\rangle$

1.4 Momentum and Energy of Bloch Waves

In the previous section, it was shown that the wavefunctions of electrons in a periodic potential inherit the periodicity of the potential. Additional insight can be obtained by removing the periodic potential such that $V(r) = 0$. The Schrödinger equation then represents a free electron, and its solutions are plane waves.

$$\begin{aligned} \frac{\mathcal{P}^2}{2m} \left|\psi_{\mathbf{k}}(\mathbf{r})\right\rangle &= \epsilon_{\mathbf{k}} \left|\psi_{\mathbf{k}}(\mathbf{r})\right\rangle \\ \left|\psi_{\mathbf{k}}\right\rangle &= e^{i\mathbf{k}\cdot\mathbf{r}} \\ \epsilon_{\mathbf{k}} &= \frac{\hbar^2|\mathbf{k}|^2}{2m} \end{aligned} \tag{1.32}$$

Adding in a periodic potential simply binds the free electron plane wave solutions to the periodicity of that potential. Plane waves may be thought of as Bloch states with $u_k(\mathbf{r}) = 1$. The Bloch phase is simply the phase of a free electron with wavevector $\mathbf{k}$.

1.4.1 The Momentum Operator

Generally, all of the electronic properties of a given lattice can be reduced to the study of the Bloch waves of that lattice. It is interesting to consider the momentum and energy of Bloch waves. Let $|\psi_k(\mathbf{r})\rangle$ be a Bloch wave describing the state of an electron in an arbitrary lattice.

$$\left|\psi_{\mathbf{k}}(\mathbf{r})\right\rangle = e^{i\mathbf{k}\cdot\mathbf{r}} \left|u_{\mathbf{k}}(\mathbf{r})\right\rangle \tag{1.33}$$

The momentum of a Bloch wave is given by the momentum operator $\mathcal{P} = -i\hbar\nabla$.

$$\begin{aligned} \mathcal{P}\left|\psi_{\mathbf{k}}(\mathbf{r})\right\rangle &= -i\hbar\nabla e^{i\mathbf{k}\cdot\mathbf{r}} \left|u_{\mathbf{k}}(\mathbf{r})\right\rangle \\ &= e^{i\mathbf{k}\cdot\mathbf{r}} \left[\mathcal{P} + \hbar\mathbf{k}\right] \left|u_{\mathbf{k}}(\mathbf{r})\right\rangle \end{aligned} \tag{1.34}$$

Thus, Bloch states are *not* eigenfunctions of the momentum operator. This is of course expected as the eigenstates of the momentum operator are *plane waves*. From the above relation one has the useful identity.

$$\left\langle\psi_{\mathbf{k}}(\mathbf{r})\right| \mathcal{P}\psi_{\mathbf{k}}(\mathbf{r})\rangle = \left\langle u_{\mathbf{k}}(\mathbf{r})\right| \left[\mathcal{P} + \hbar\mathbf{k}\right] u_{\mathbf{k}}(\mathbf{r})\rangle \tag{1.35}$$

Upon further inspection, the fact that Bloch waves are not eigenstates of the momentum operator may be understood in terms of the uncertainty principle.

$$\sigma_x\sigma_p \geq \hbar/2 \tag{1.36}$$

A plane wave has infinite spatial extent, and a perfectly defined momentum. The fact that Bloch waves are not eigenstates of the momentum operator implies a finite spatial extent (i.e. a localization of electrons). * The quantity $\hbar\mathbf{k}$ is known as the *crystal momentum.* Substituting a Bloch wave into the time independent Schrödinger equation gives the following.

$$\left[\frac{1}{2m}\left(\mathcal{P} + \hbar\mathbf{k}\right)^2 + V(\mathbf{r})\right] \left|u_{\mathbf{k}}(\mathbf{r})\right\rangle = \epsilon_k \left|u_{\mathbf{k}}(\mathbf{r})\right\rangle \tag{1.37}$$

Where $u_k(\mathbf{r})$ inherits the periodicity of the lattice in question. The solutions to the Schrödinger equation are what yield *band structure* in a material.

---

[*] In fact, it can be shown that a plane wave is minimum uncertainty state. such that $\sigma_x\sigma_p = \hbar/2$

1.4.2 Velocity of Bloch States and the Effective Mass

It is useful to examine the Hamiltonian of Bloch states via perturbation theory. Let us assume a Hamiltonian $\mathcal{H}_0$ where eigenvalues and eigenfunctions $\mathcal{H}_0$ are known.

$$\mathcal{H}_0 \left|\psi_{0,n}\right\rangle = \epsilon_{0,n} \left|\psi_{0,n}\right\rangle \tag{1.38}$$

Now consider the case where $\mathcal{H}_0$ is perturbed by a small variation $\mathcal{H}'$. One would like to discover the new eigenvalues ϵ_n associated with the new Hamiltonian.

$$\mathcal{H} \left|\psi_n\right\rangle = \left[\mathcal{H}_0 + \mathcal{H}'\right] \left|\psi_n\right\rangle = \epsilon_n \left|\psi_n\right\rangle \tag{1.39}$$

Because $\mathcal{H}'$ is small, one should expect the new eigenvalues and eigenfunctions to be very similar to the old ones. To first order, the new eigenvalues and eigenfunctions are given by the following.

$$\delta\epsilon_n = \left\langle \psi_{0,n} \right| \mathcal{H}' \psi_{0,n} \rangle \tag{1.40}$$

In the previous section, the Hamiltonian for a Bloch state took the following form.

$$\mathcal{H}_{\mathbf{k}} = \left[\frac{1}{2m} \left(\mathcal{P} + \hbar\mathbf{k}\right)^2 + V(\mathbf{r})\right] \tag{1.41}$$

By considering a small change in momentum $\mathbf{k} \rightarrow \mathbf{k} + \mathbf{\Delta k}$ one can deduce the velocity of a Bloch state.

$$\mathcal{H}_{\mathbf{k}+\mathbf{\Delta k}} = \mathcal{H}_{\mathbf{k}} + \frac{\mathbf{\Delta k}}{m} \cdot \left[\mathcal{P} + \hbar\mathbf{k}\right] + \mathcal{O}(\mathbf{\Delta k}^2) \tag{1.42}$$

Treating the second term as a perturbation, one has that the first order correction to the energy is given by the following.

$$\begin{aligned} \delta E(\mathbf{p}) &= \langle u_{\mathbf{k}} | \left[\mathcal{P} + \hbar\mathbf{k}\right] u_{\mathbf{k}} \rangle \cdot \frac{\mathbf{\Delta k}}{m} \\ \nabla_{\mathbf{k}} \epsilon(\mathbf{k}) \cdot \frac{\mathbf{\Delta k}}{\hbar} &= \langle \psi_{\mathbf{k}} | \mathcal{P} \psi_{\mathbf{k}} \rangle \cdot \frac{\mathbf{\Delta k}}{m} \\ &= \frac{\langle \mathbf{p} \rangle}{m} \cdot \mathbf{\Delta k} \\ &= \langle \mathbf{v} \rangle \cdot \mathbf{\Delta k} \end{aligned} \tag{1.43}$$

Such that the velocity of a Bloch state is proportional to the first derivative of the energy. [*]

$$\langle \mathbf{v} \rangle = \frac{1}{\hbar} \nabla_{\mathbf{k}} \epsilon(\mathbf{k}) \tag{1.44}$$

For a free electron (i.e. a Bloch state in which $u_{\mathbf{k}}(\mathbf{r}) = 1$) Bloch waves become plane waves. In this case the velocity is exactly one would expect.

$$\langle \mathbf{v} \rangle = \frac{\hbar|\mathbf{k}|}{m} = \frac{\mathbf{p}}{m} \tag{1.45}$$

Given the velocity of a Bloch wave, it is straightforward to write an expression of second Newton's Law for a Bloch state subject to an external force such as an electric field.

$$\frac{\mathbf{F}}{m} = \frac{d\langle \mathbf{v} \rangle}{dt} = \frac{\hbar}{m} \frac{d\mathbf{k}}{dt} \tag{1.46}$$

---

[*] This result can be understood as a quantum mechanical analog of a familiar classical derivation. If the kinetic energy is $E = p^2/2m$ then the velocity may be found as follows. $\frac{dE}{dp} = \frac{1}{\hbar}\frac{dE}{dk} = \frac{p}{m} = v$

Substituting in the velocity and being careful with differentiation for one of the components of the force, one has the following.

$$\frac{\hbar}{m}\frac{dk_i}{dt} = \frac{1}{\hbar}\frac{d}{dt}\frac{\partial \epsilon(\mathbf{k})}{\partial k_i} = \left[\frac{1}{\hbar}\sum_j \frac{\partial^2 \epsilon(\mathbf{k})}{\partial k_i \partial k_j}\right]\frac{dk_i}{dt} \tag{1.47}$$

This allows one to solve for the mass m.

$$\frac{1}{m} = \sum_j \frac{1}{\mathcal{M}_{ij}} = \left[\frac{1}{\hbar^2}\sum_j \frac{\partial^2 \epsilon(\mathbf{k})}{\partial k_i \partial k_j}\right] \tag{1.48}$$

Simply, this means that the mass must be interpreted as a tensor whereby.

$$\frac{1}{\mathcal{M}(\mathbf{k})_{ij}} = \left[\frac{1}{\hbar^2}\frac{\partial^2 \epsilon(\mathbf{k})}{\partial k_i \partial k_j}\right] \tag{1.49}$$

This $\mathcal{M}(\mathbf{k})_{ij}$ tensor is known as the *effective mass tensor*. In this case the Newton's law looks as follows.

$$\mathbf{F} = \mathcal{M}(\mathbf{k})\frac{d\langle \mathbf{v}\rangle}{dt} \tag{1.50}$$

The direct interpretation is that the velocity associated with a Bloch state (e.g. an electron) may not be parallel to the applied force (e.g. an electric field). In the case where the effective mass tensor contains off-diagonal elements, electrical resistance will differ along different crystal axes.

1.5 Second Quantization

> *First quantization is a mystery, but second quantization is a functor.* -Edward Nelson

Until now, we have been working explicitly in the world of *first quantization.* In other words, classical electrons have been treated as wave amplitudes $|\psi\rangle$, and their dynamical degrees of freedom (position and momentum) have been promoted to *operators*. One can find the energy associated with a given wave amplitude by solving the Schrödinger equation. [*] Generally, a particle is described by a state $|\psi\rangle$ that lives in Hilbert space $\mathbb{H}$. The problem is that Hilbert space only contains states for one particle! The need for the second quantization formalism arises out of three facts; electrons are *identical particles*, there are many of them, and they often interact. In second quantization, the wave amplitudes themselves are treated as discrete quanta [18, 19].

The essential idea behind second quantization is that the one particle Hilbert space is extended to accommodate more particles in the same way one expands 1-dimensional space into higher dimensions. A space $\mathcal{F}$ which accommodates n particles may be formed by taking a *direct product* of n Hilbert spaces $\mathcal{F} = \mathbb{H} \otimes \cdots \otimes \mathbb{H}$. Here $\mathcal{F}$ (the Fock space) is a Hilbert space of Hilbert spaces. Mathematically, the process of second quantization transforms a Hilbert space (a category) into a Hilbert space of Hilbert spaces (another category). Since the process of second quantization transforms a category into another category, it is a *functor* by definition. The eigenfunctions of $\mathcal{F}$ are symmetric (Bosons) or anti-symmetric (Fermions) tensor products of single particle states $|\psi\rangle$. The objective is to apply the foundations of second quantization to obtain a clean derivation of the electronic band structure in graphene.[†]

---

[*] This is the mystery of first quantization. There is no *a priori* reason or rigorous mathematical justification to motivate the transition from classical mechanics to a quantum description.

[†] In all of these derivations, the spin of the particles is neglected. In general, what follows is a very cursory overview of second quantization.

One begins by introducing the vacuum state $|0\rangle$ which contains no particles and therefore no energy. In order to add and remove electrons from the vacuum state one applies the creation $c_k^\dagger$ and annihilation operators c_k. Because we are interested in electrons, we must work with the fermionic operators. Consider the operation of the creation operator on the vacuum state $|0\rangle$. [*]

$$\begin{aligned} c_k^\dagger |0\rangle &= |1_k\rangle \\ c_{k'}^\dagger c_k^\dagger |0\rangle &= |1_{k'}, 1_k\rangle \end{aligned} \tag{1.51}$$

The notation $|1_k\rangle$ indicates a one electron state with momentum k. For a two particle fermionic system, the two particle state is resolved into one particle states in the following manner.

$$|1_{k'}, 1_k\rangle = \frac{1}{\sqrt{2}} \left[|1_{k'}\rangle \otimes |1_k\rangle - |1_k\rangle \otimes |1_{k'}\rangle \right] \tag{1.52}$$

Notice that one has $|1_{k'}, 1_k\rangle = 0$ for $k = k'$. This is none other than the Pauli exclusion principle. No two fermions can live in the same state. The wavefunction is antisymmetric under exchange $|1_{k'}\rangle \leftrightarrow |1_k\rangle$ such that one has the following.

$$|1_{k'}, 1_k\rangle = - |1_k, 1_{k'}\rangle \tag{1.53}$$

The antisymmeterization property can be written in terms of creation operators.

$$\begin{aligned} c_{k'}^\dagger c_k^\dagger |0\rangle &= -c_k^\dagger c_{k'}^\dagger |0\rangle \\ \left\{ c_{k'}^\dagger, c_k^\dagger \right\} &= 0 \end{aligned} \tag{1.54}$$

Here the curly brackets indicate *anti*-commutation. $\left\{ \hat{A}, \hat{B} \right\} = \hat{A}\hat{B} + \hat{B}\hat{A}$. [†] The identity $|1_{k'}, 1_k\rangle + |1_{k'}, 1_k\rangle = 0$ is the source of anti-commutation. It is also useful to evaluate the following anticommutator.

$$\begin{aligned} \left\{ c_{k'}, c_k^\dagger \right\} |1_{k'}, 1_k\rangle &= \left[c_{k'} c_k^\dagger + c_k^\dagger c_{k'} \right] |1_{k'}, 1_k\rangle \\ &= 0 + \delta_{k,k'} |1_{k'}, 1_k\rangle \end{aligned} \tag{1.55}$$

One has that $c_{k'}$ and $c_k^\dagger$ anticommute except when $k = k'$. The anti-commutation relations of the fermionic operators are summarized below.

$$\left\{ c_i^\dagger, c_j^\dagger \right\} = 0 \qquad \{ c_i, c_j \} = 0 \qquad \left\{ c_i, c_j^\dagger \right\} = \delta_{ij} \tag{1.56}$$

The first two relationships encode the anti-symmetry of fermionic states (i.e. Pauli exclusion). The third relation is ultimately inherited from the fact that position and momentum do not commute in first quantization. It is also useful to see how a change of basis operation happens in second quantization. Let us assume we have an electron state in momentum space $|\mathbf{k}\rangle$ and we would like to express it terms of the position space eigenfunctions $|\mathbf{r}\rangle$. In the first quantized formalism, one simply applies the projection operator.

$$|\mathbf{k}\rangle = \sum_r |\mathbf{r}\rangle \langle \mathbf{r}| \, \mathbf{k}\rangle \tag{1.57}$$

One can substitute for $|\mathbf{k}\rangle$ and $|\mathbf{r}\rangle$ with creation operators.

$$c_k^\dagger |0\rangle = \sum_r \langle \mathbf{r}| \, \mathbf{k}\rangle \, c_r^\dagger |0\rangle \tag{1.58}$$

---

[*] Mathematically $\mathcal{H}|0\rangle = 0\,|0\rangle$. Here we make no redress to the implied ultraviolet divergence and need for renormalization associated with the vacuum state in field theory. We just assume that it is possible to define such a state with no energy. In this light, the introduction of $c_k^\dagger$ and c_k is somewhat heuristic insofar as we assume that it is possible to define such operators.

[†] Commutators in quantum theory are the equivalent of Poisson brackets in classical mechanics.

Here the inner product evaluates as $\langle \mathbf{r} | \, \mathbf{k} \rangle = e^{i\mathbf{r}\cdot\mathbf{k}}$. The change of basis operations in terms of creation and annihilation operators between position and momentum space are then.

$$\begin{aligned} c_k^\dagger &= \sum_r e^{i\mathbf{r}\cdot\mathbf{k}} c_r^\dagger \\ c_r^\dagger &= \sum_k e^{-i\mathbf{r}\cdot\mathbf{k}} c_k^\dagger \end{aligned} \tag{1.59}$$

Here the sums are taken over all allowed positions and momenta (i.e. they are integrals). It is interesting to note that both position and momentum here have been demoted to parameters to be summed over. Furthermore, there are an infinite number of creation and annihilation operators (one for every position and momentum) such that the number of dynamical degrees of freedom has somehow become infinite. * In solid state theory one handles this infinity by cutting the integral off at the boundary of the first Brillouin zone. The last issue is to outline how to handle an observable such as the energy in the second quantized formalism. Operators involving a sum over single particles are known as single particle operators.

$$\mathcal{A} = \sum_i \mathcal{A}_i(x_i, k_i) \tag{1.60}$$

Here the operator $\mathcal{A}_i$ is defined in phase space and acts on the i-th particle in the system. In the above case, $\mathcal{A}$ may be taken as the total energy. The sum simply states that the total energy is the sum over the energies of all the particles in the system. In the second quantization formalism, the operator can be written in the following way.

$$\hat{A} = \sum_{ij} \langle i | \, \mathcal{A}_j \, | j \rangle \, c_i^\dagger c_j \tag{1.61}$$

This can be directly applied to obtain the single particle Hamiltonian. This is the equation that must be solved in order to obtain the band structure of graphene.

$$\begin{aligned} \mathcal{H} &= \sum_{k'k} \langle k' | \, \mathcal{H}_k \, | k \rangle \, c_{k'}^\dagger c_k \\ &= \sum_{k'k} \epsilon_k \langle k' | \, k \rangle \, c_{k'}^\dagger c_k \\ &= \sum_k \epsilon_k c_k^\dagger c_k \end{aligned} \tag{1.62}$$

Here ϵ_k is the energy of an electron with momentum k. The operator $n_k = c_k^\dagger c_k$ is often referred to as the number operator. For a given quantum state in Fock space $|\ldots\rangle$ then $n_k \, |\ldots\rangle$ returns the number of particles with momentum k. For a fermionic system, this will be either 1 or 0. The operation of the Hamiltonian on a single particle state gives $\mathcal{H} \, |k\rangle = \epsilon_k \, |k\rangle$. This is identical to the case of first quantization.

1.6 Wannier Functions and the Tight Binding Model

Because our lattice is periodic, its wavefunctions must be Bloch waves. However, nothing has been said regarding the potential energy of the system. In order to make progress towards solving the Schrödinger equation for our lattice, a simplifying assumption must be made regarding the nature of the potential. Let us consider the case where electrons remain close to their ionic cores in *real space. Such an assumption, known as a tight-binding model, makes sense when the physical extent of the atomic wavefunctions is much less than the inter atomic spacing.* [12]

---

[*] Here it is implied that an electron is behaving as a classical *field* If one has electron, it is defined at every point in position space and at every point momentum space

The Bloch states $|\mathbf{k}\rangle$ are the eigenstates of $\mathcal{H}$ defined in *momentum space.* However, it is also possible to construct eigenstates of $\mathcal{H}$ in *position space* which are relatively localized around the ionic cores. These functions are known as Wannier functions after the Swiss physicist Gregory Wannier. For the atom located at position $\mathbf{R}_i$, the associated Wannier function $|\mathbf{R}_i\rangle$ can be written as a linear combination of the Bloch states $|\mathbf{k}\rangle$.

$$|\mathbf{R}_i\rangle = \frac{1}{\sqrt{N}} \sum_k e^{-i\mathbf{k}\cdot\mathbf{R_i}} |k\rangle \tag{1.63}$$

Under a tight binding assumption, one expects that the Wannier functions should look very much like the localized atomic orbitals of the lattice atoms. Usually they are assumed to take the form of a linear combination of the atomic orbitals (LCAO). It is easy to see that the Wannier functions form an orthonormal basis and are therefore an equally viable description of the system. Here the sum over k indicates that one must sum over all of the values in the first Brillouin zone. Mathematically, the Wannier functions are simply an inverse Fourier transform of the Bloch states. The normalization factor N indicates the number of atoms in the lattice. In analogy to Eq. 1.59, it is possible to write the Wanner functions in terms creation and annihilation operators.

$$\begin{aligned} c_k^\dagger &= \frac{1}{\sqrt{N}} \sum_i e^{i\mathbf{k}\cdot\mathbf{R}_i} c_i^\dagger \\ c_i^\dagger &= \frac{1}{\sqrt{N}} \sum_k e^{-i\mathbf{k}\cdot\mathbf{R}_i} c_k^\dagger \end{aligned} \tag{1.64}$$

The tight binding Hamiltonian is then derived by substitution of the Wannier creation and annihilation operators into the single particle Hamiltonian (Eq. 1.62).

$$\mathcal{H} = \sum_k \epsilon_k c_k^\dagger c_k = \sum_{ij} \left[\frac{1}{N} \sum_k \epsilon_k e^{i\mathbf{k}\cdot(\mathbf{R}_i - \mathbf{R}_i)} \right] c_i^\dagger c_j = \sum_{ij} \gamma_{ij} c_i^\dagger c_j \tag{1.65}$$

The term in square brackets has been assigned a new variable γ_{ij} known as the hopping amplitude for an electron to move from the atom at $\mathbf{R}_j$ to $\mathbf{R}_i$. Identifying the cases of $i = j$ and $i \neq j$ then one has the following.

$$\mathcal{H} = \sum_i \epsilon_i c_i^\dagger c_i + \sum_{i \neq j} \gamma_{ij} c_i^\dagger c_j \tag{1.66}$$

The term ϵ_i represents the self-energy of an electron living with atom $\mathbf{R}_i$. Generally this term is set to zero for the equilibrium case. In the following chapter, the consequences a non-zero self energy term will be explored in problem of bi-layer graphene with an applied vertical field. For the derivation of the band structure we will take $\epsilon_i = 0 \quad \forall i$

1.7 Band Structure in Graphene

With the formalism of second quantization along with Wannier functions one gains a very intuitive picture of the band strucutre. Here we will work with the a and b sublattices. We begin by writing down creation operators for the sublattices $a_i^\dagger$ and $b_i^\dagger$. By operating on the vacuum state one has the following for the sublattices.

$$\begin{aligned} a_i^\dagger |0\rangle &= |\mathbf{R}_i^a\rangle \\ b_i^\dagger |0\rangle &= \left|\mathbf{R}_i^b\right\rangle \end{aligned} \tag{1.67}$$

Note that we are here working in the basis of Wannier functions (i.e. we are in real space). These relations may be interpreted as creating an electron on the a or b atom of the unit cell indexed by the position vector $\mathbf{R}_i$. Now, the tight binding Hamiltonian takes the following form.

$$\mathcal{H} = -\gamma \sum_{\langle ij \rangle} b_j^\dagger a_i + a_j^\dagger b_i \tag{1.68}$$

The exact solution is given by allowing the sum is taken to run over all $i \neq j$. However, for such a problem an analytic solution is intractable. As a first approximation, the sum will be taken to run only over the *nearest neighbors*. This is indicated by the notation $\langle ij \rangle$. Looking at the first term in the sum one can see that an electron is annihilated at position $\mathbf{R}_i^a$ and subsequently created at a nearest neighbor atom $\mathbf{R}_j^b$. This is known as a/b hopping. Similarly the second term indicates hopping from the b sublattice to the a sublattice. Given the symmetry of the problem the hopping energy γ is equivalent in both cases. Experimental measurements have shown that $\gamma = 3.033eV$[20, 17].

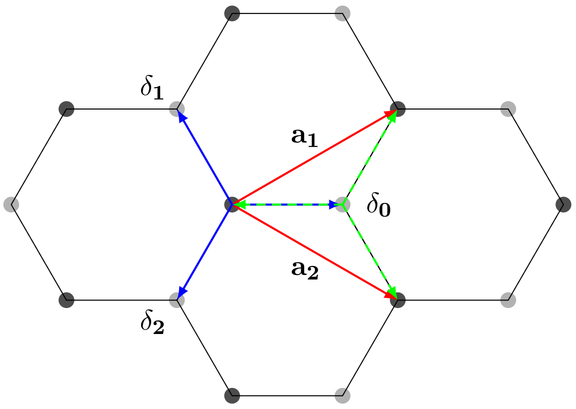

Figure 1.6: A reproduction of the diagram 1.4 for the purposes of the derivation of the band structure. The nearest neighbor vectors $\delta_\mathbf{n}$ for the a sublattice (blue/labeled) and b sublattice (green/dashed) are shown. In this case, we are working with Wannier functions, such that the real space picture is appropriate.

As in all quantum mechanical problems, our objective is to find the eigenvalues of the Hamiltonian. Particularly, one is interested in $\epsilon(\mathbf{k})$ such that a change of basis to momentum space is needed.

$$\begin{aligned} a_i^\dagger &= \sum_k e^{-i\mathbf{R_i^a}\cdot\mathbf{k}} a_k^\dagger \\ b_i^\dagger &= \sum_k e^{-i\mathbf{R_i^b}\cdot\mathbf{k}} b_k^\dagger \end{aligned} \tag{1.69}$$

Here we isolate the a/b hopping term. The b/a hopping term is then found by taking the complex conjugate of the a/b term. This follows from the fact that $\mathcal{H}$ is Hermitian. Performing a change of basis for $\mathcal{H}$ one finds the following.

$$\begin{aligned} \mathcal{H} &= -\gamma \sum_k \sum_{\langle ij \rangle} e^{i(\mathbf{R_j^a}-\mathbf{R_i^b})\cdot\mathbf{k}} b_k^\dagger a_k \\ &= -\gamma \sum_k \left\{ \sum_n e^{i\delta_n\cdot\mathbf{k}} \right\} b_k^\dagger a_k \end{aligned} \tag{1.70}$$

The sum in k should be taken over all values in the first Brillouin zone (i.e. it is actually an integral). Here we identify the following term in the momentum space Hamiltonian. The result for b/a hopping is also shown.[21]

$$\begin{aligned} f(\mathbf{k}) &= -\gamma \sum_n e^{i\delta_\mathbf{n}\cdot\mathbf{k}} \\ f^*(\mathbf{k}) &= -\gamma \sum_n e^{-i\delta_\mathbf{n}\cdot\mathbf{k}} \end{aligned} \tag{1.71}$$

The full Hamiltonian in k space can be constructed in terms of sums over the nearest neighbor vectors. This Hamiltonian can be represented by a 2x2 anti-diagonal matrix. The anti-diagonality comes from the fact that we are working in the basis of sublattices. The only interaction that occurs is between the a and b sublattices (i.e. off diagonal elements).

$$\begin{aligned}\mathcal{H} &= -\gamma \sum_k f(\mathbf{k}) b_k^\dagger a_k + f^*(\mathbf{k}) a_k^\dagger b_k \\ &= \begin{bmatrix} 0 & f(\mathbf{k}) \\ f^*(\mathbf{k}) & 0 \end{bmatrix}\end{aligned} \tag{1.72}$$

Solving the secular equation gives the energy momentum relationship $\epsilon_{\mathbf{k}}$.

$$\begin{aligned}|\mathcal{H} - \epsilon_{\mathbf{k}} \mathbb{I}| &= 0 \\ \epsilon(\mathbf{k}) &= \pm |f(\mathbf{k})|\end{aligned} \tag{1.73}$$

Substituting in for nearest neighbor vectors $\delta_{\mathbf{n}}$ one has for $f(\mathbf{k})$ and $\epsilon(\mathbf{k})$ [22, 21]

$$\begin{aligned}f(\mathbf{k}) &= -\gamma \left[e^{i\mathbf{k}\cdot\delta_{\mathbf{0}}} + 2e^{i\mathbf{k}\cdot(\delta_{\mathbf{1}}+\delta_{\mathbf{2}})/2} \cos\left(\frac{\mathbf{k}\cdot(\delta_{\mathbf{1}}-\delta_{\mathbf{2}})}{2}\right)\right] \\ &= -\gamma \left[e^{ik_x a_0} + 2e^{-ik_x a_0/2} \cos\left(\frac{\sqrt{3}a_0}{2} k_y\right)\right] \\ \epsilon_{\mathbf{k}} &= \pm\gamma \sqrt{3 + 2\cos\left(\sqrt{3}a_0 k_y\right) + 4\cos\left(\frac{3a_0}{2}k_x\right)\cos\left(\frac{\sqrt{3}a_0}{2}k_y\right)}\end{aligned} \tag{1.74}$$

The eigenvalues of the Hamiltonian $\epsilon_{\mathbf{k}}$ is the band structure. With a bit of linear algebra, it is possible to show that the corresponding *normalized* eigenvectors are as follows [23]

$$\begin{aligned}|+\rangle &= \frac{1}{\sqrt{2}} \begin{bmatrix} 1 \\ e^{-i\theta(\mathbf{k})} \end{bmatrix} \\ |-\rangle &= \frac{1}{\sqrt{2}} \begin{bmatrix} 1 \\ -e^{-i\theta(\mathbf{k})} \end{bmatrix}\end{aligned} \tag{1.75}$$

The Hamiltonian can be rewritten in terms of $\epsilon(\mathbf{k})$ by noticing that $f(\mathbf{k}) = |\epsilon(\mathbf{k})| e^{i\theta(\mathbf{k})}$. Here $\theta(\mathbf{k})$ describes the phase that is associated with the Bloch eigenstates composing our wavefunction.

$$\mathcal{H} = |\epsilon(\mathbf{k})| \begin{bmatrix} 0 & e^{i\theta(\mathbf{k})} \\ e^{-i\theta(\mathbf{k})} & 0 \end{bmatrix} \tag{1.76}$$

Near the special Brillouin zone points K and K' the energy $\epsilon_{\mathbf{K}+\delta\mathbf{K}} = \epsilon_{\mathbf{K}'+\delta\mathbf{K}}$ so that a measurement of the energy of an electron near $\mathbf{K}$ or $\mathbf{K}'$ will not determine whether it is in the $|+\rangle$ state or $|-\rangle$ state. It was mentioned previously that the points $\mathbf{K}$ and $\mathbf{K}'$ are *not* equivalent, as $\mathbf{K}$ cannot be mapped to $\mathbf{K}'$ by translation via reciprocal lattice vectors. Thus there is a *twofold valley degeneracy* associated with the points K and K'. Furthermore, in all of these calculations, electrons have been treated as *spin zero* particles in order preserve the cogency of logic. It is important to remember that an electron can live in two spin states giving rise to a *twofold spin degeneracy.*

It is no surprise that both the derivation of the phonon spectrum and the derivation of the band structure in graphene both involve sums over the nearest neighbor vectors. In both problems, the result comes from considering the coupling between sublattices. In the former, this coupling comes from considering a harmonic restoring force between nearest neighbors, and in the latter the coupling comes from the assumption that a tightly bound electron has some finite coupling with his nearest neighbors. The physics of the phonon spectrum and the band structure ultimately has its origin in the periodic arrangement of the carbon atoms which make up the lattice. Here, the phonon properties are completely general to any honeycomb lattice with the exception of the magnitudes of the components of the force tensor. The band structure, however, is a consequence of the fact that the hexagonal arrangement is formed of sp_2 *Carbon* atoms. The idea of *silicine*, a honeycomb arrangement of Silicon atoms, has also been explored theoretically and would have nearly identical properties to graphene[24]. It is debated whether such an arrangement is stable, as Silicon is only found in nature in the sp_3 or diamondlike configuration. This is different from Carbon which plentiful in Nature in its sp_2 form as graphite.

1.7.1 Visualizing Grapehene's Band Structure

Because so many of the interesting properties of graphene may be deduced from a study of its band structure, it is very helpful to visualize the band structure. Various visualiations of the band structure (Eq. 1.74) are shown below. The band structure is plotted in the first Brillouin zone and the special *high symmetry points* points are noted in the diagram. Also a plot is shown of the energy along the irreducible path in the Brillouin zone. Conduction states $|+\rangle$ are shown in blue, and valence states $|-\rangle$ are shown in red.

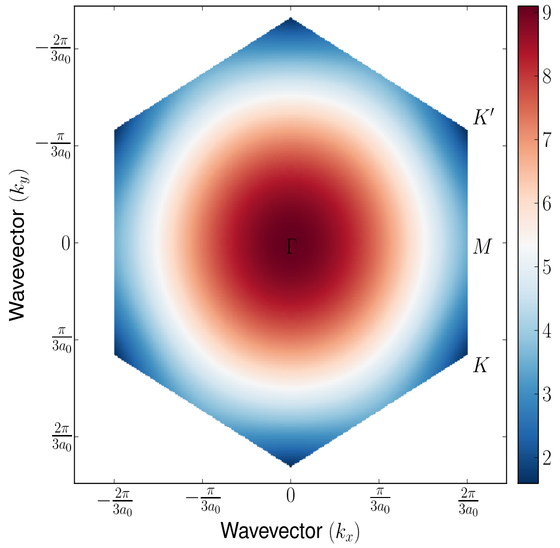

Figure 1.7 *(left)*: A diagram of the conduction band structure plotted in the first Brillouin Zone in graphene. The special points K, K',M and Γ are also shown. Analogous simulations in the first Brillouin zone band structure and phonon energy are available in [17].

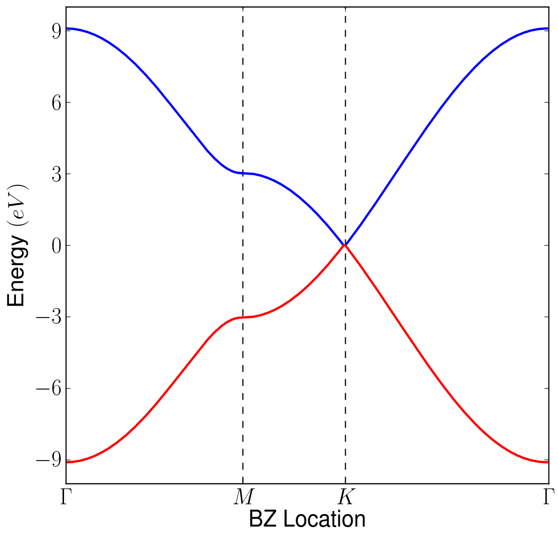

Figure 1.8 *(right)*: A diagram of the valence (red) and conduction (blue) bands in graphene plotted along the irreducible path in the first Brillouin Zone in graphene.

To interpret the plots, all electrons in the graphene have an associated wavevector $\mathbf{k}$ which may be taken to lie in the first Brillouin zone in the reduced zone scheme. The results of the tight binding approximation give an energy associated with each of these vectors $\epsilon_{\mathbf{k}}$. The plot of $\epsilon_{\mathbf{k}}$ is by definition, the band structure. Figures 1.9 and 1.10 show the band structure visualized in three dimensions. The bandstructure of epitaxial graphene on SiC has also been measured experimentally near the Dirac point by Angle Resolved Photo Electron Spectroscopy [25] and also along the irreducible path [26].

It is important to note that the solution for $\epsilon_{\mathbf{k}}$ includes two values for every value of $\mathbf{k}$. The values are equal in magnitude and opposite in sign. In this way, the three dimensional plot of the band structure is symmetric about the plane $\epsilon(\mathbf{k}) = 0$. This is the direct result of taking the self energy to be zero in the tight-binding approximation.The band structure around the special points in the Brillouin zone labeled K and K' is approximately conical. Geometrically $\epsilon(\mathbf{k})$ is flat in this region, such that all of its second derivatives vanish. [*] Thus one comes to a most interesting property of ideal graphene, namely *The effective mass of a Bloch state is zero at K and K' points.* Because electrons in the K and K' valleys are massless a relativistic quantum mechanical model is needed (i.e. the Dirac equation must be used). It is for this reason that electrons near the K and K' points are termed *massless Dirac fermions.* The K and K' points themselves are known as *Dirac Points.* [27, 28]

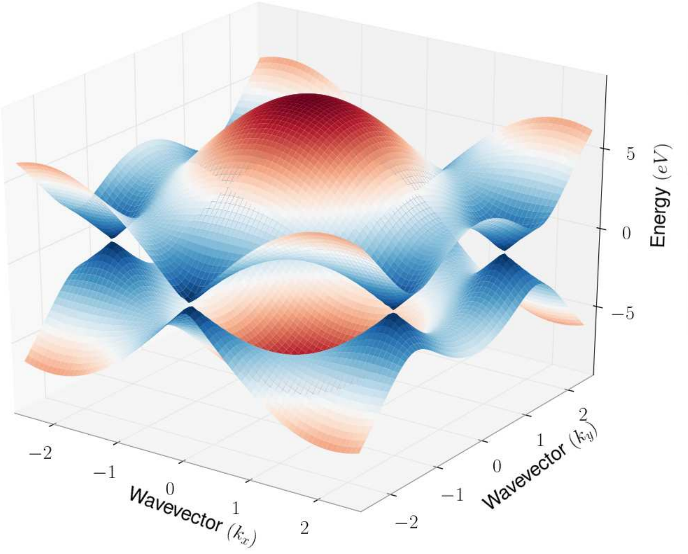

Figure 1.9 *(left)*: A three dimensional simulation of the band structure of monolayer graphene. The conduction and valence bands are symmetric around the $\epsilon = 0$ plane. The hexagonal structure reflects the geometry of the first Brillouin zone.

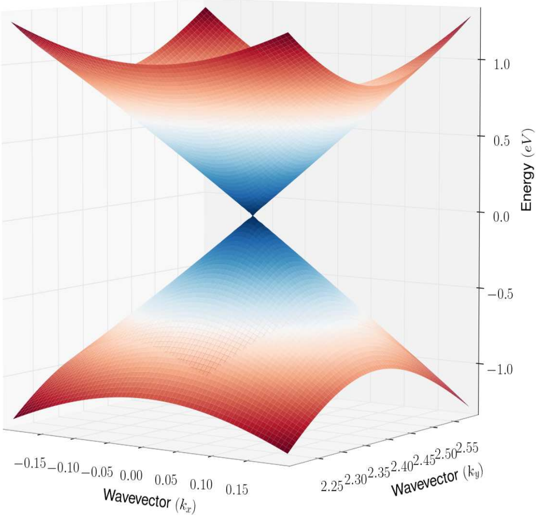

Figure 1.10 *(right)*: A three dimensional visualization of the band structure as it approaches $E = 0$. This occurs at the special points K and K' in the first Brillouin zone. The band structure is conical, and the dispersion $\epsilon_{\mathbf{k}})$ is linear in this region.

1.7.2 The Low Energy Hamiltonian

It is interesting to linearize the band structure around the K or K' points. To do this, one begins by evaluating $f_D(\mathbf{K}^* + \delta\mathbf{k})$. Here $\mathbf{K}^*$ is taken to represent either $\mathbf{K}$ or $\mathbf{K}'$. The subscript D indicates that one is investigating the behavior around the Dirac point. [22, 21]

$$f_D(\mathbf{K}^* + \delta\mathbf{k}) = -\gamma\left[e^{i(\mathbf{K}^*+\delta\mathbf{k})\cdot\boldsymbol{\delta_0}} + 2e^{i(\mathbf{K}^*+\delta\mathbf{k})\cdot(\boldsymbol{\delta_1}+\boldsymbol{\delta_2})/2}\cos\left(\frac{(\mathbf{K}^*+\delta\mathbf{k})\cdot(\boldsymbol{\delta_1}-\boldsymbol{\delta_2})}{2}\right)\right] \tag{1.77}$$

Linearizing around $f(\mathbf{K} + \delta\mathbf{k})$ one obtains the behavior of the band structure near the Dirac points.

$$f_D(\mathbf{K}^* + \delta\mathbf{k}) = -\frac{3\gamma a_0}{2}\left[\xi\delta k_y + i\delta k_x\right] \tag{1.78}$$

Here $\xi = 1$ for the K valley and $\xi = -1$ for the K' valley. By substitution, one obtains the low energy Hamiltonian.

$$\mathcal{H} = -\frac{3\gamma a_0}{2}\begin{bmatrix} 0 & \xi\delta k_y + i\delta k_x \\ \xi\delta k_y - i\delta k_x & 0 \end{bmatrix} \tag{1.79}$$

---

[*] *A cone is flat everywhere except at the tip.* In other words, the scalar curvature of the cone is zero except at the tip where it is infinite. It is interesting that this concept, which is often discussed in the context of general relativity, appears in the physics of a microscopic system.

The band structure near the Dirac point may be expressed as follows.

$$\begin{aligned}\epsilon_D(\delta\mathbf{k}) &= |f_D(\mathbf{K}+\delta\mathbf{k})| \\ &= \pm\frac{3\gamma a_0}{2}\left[\delta k_x^2+\delta k_y^2\right] \\ &= \pm\frac{3\gamma a_0}{2}|\delta\mathbf{k}|\end{aligned} \tag{1.80}$$

The energy near the Dirac point is typically expressed in terms of the Fermi velocity v_f

$$\epsilon_D(\delta\mathbf{k}) = \pm v_f\cdot\hbar|\delta\mathbf{k}| = \pm v_f|\mathbf{p}| \tag{1.81}$$

Here v_f is the Fermi velocity which can be calculated from the interatomic spacing a_0 and the coupling energy between orbitals γ.

$$v_f = \frac{3\gamma a_0}{2\hbar} \approx 1e8(cm/s) \tag{1.82}$$

The term v_f relates the momentum of an electron near the points K and K' to its energy [*]. The low energy Hamiltonian is often written compactly in terms of a phase angle.

$$\mathcal{H} = \hbar v_f|\delta\mathbf{k}|\begin{bmatrix} 0 & e^{i\xi\theta(\delta\mathbf{k})} \\ e^{-i\xi\theta(\delta\mathbf{k})} & \end{bmatrix} \tag{1.83}$$

Where the angle $\theta(\delta\mathbf{k})$ is the angle of the vector $\delta\mathbf{k}$ with respect to the k_y axis [†].

$$\theta(\delta\mathbf{k}) = \arctan\frac{\delta k_x}{\delta k_y} \tag{1.84}$$

This is the form of the Hamiltonian which is most useful for calculations relevant to electronics. A spin formulation of the Hamiltonian is also used in certain contexts. [23]

$$\begin{aligned}\mathcal{H}_\xi &= \hbar v_f\left[\xi\sigma^1\delta k_y - \sigma^2\delta k_x\right] \\ &= \hbar v_f\sigma\cdot\mathbf{p}\end{aligned} \tag{1.85}$$

Where σ^1 and σ^2 are two of the Pauli spin matrices.

$$\sigma^1 = \begin{bmatrix} 0 & 1 \\ 1 & 0\end{bmatrix} \quad \sigma^2 = \begin{bmatrix} 0 & -i \\ i & 0\end{bmatrix} \quad \sigma^3 = \begin{bmatrix} 1 & 0 \\ 0 & -1\end{bmatrix} \tag{1.86}$$

Thus we find that the low energy Hamiltonian describes a superposition of two spin-like states. The term ξ is known as the *valley isospin.* At the K point, the Hamiltonian behaves like a symmetric combination of two spin states, while at the K' point, the Hamiltonian behaves like an anti-symmetric combination of two spin states. This shows that there is a *mathematical* difference between K and K' in terms of the band structure.

When calculating the density of states, one must account for the fact that every energy level can contain four electrons, two for the ordinary spin of the electron, and two for valley isospin. Electrons in graphene will always live in the Dirac cones at equilibrium. In even the most heavily doped graphene, the highest energy electron will typically have $\epsilon_f < 300meV$. From the plots of the band structure, one can see that these energies are well within the conical regions of the band structure which generally extend up to $2eV$. Thus in all calculations regarding electronic properties at equilibrium or near equilibrium, the low energy physics outlined here applies.

---

[*] In special relativity one has the energy momentum relation $\epsilon^2 = (|\mathbf{p}|c)^2 + (mc^2)^2$. When $m = 0$ then one has $\epsilon = c|\mathbf{p}|$. This is analogous to the situation of low energy electrons in graphene where the speed of light c is replaced by the Fermi velocity v_f

[†] In a sense the angle here reflects our choice of coordinate system.

1.7.3 Berry's Phase and the Adiabatic Approximation

As a final characterization of the bandstructure of graphene, it is useful to consider what happens to the eigenfunctions around the points K and K'. This can be done by imagining a time dependent behavior of the Hamiltonian. Near the Dirac point, the Hamiltonian reads.[*]

$$\mathcal{H} = \hbar v_f |\delta\mathbf{k}| \begin{bmatrix} 0 & e^{i\xi\theta(\delta\mathbf{k})} \\ e^{-i\xi\theta(\delta\mathbf{k})} & \end{bmatrix} \tag{1.87}$$

It is interesting to evaluate what happens to the eigenfunctions of the Hamiltonian if the Hamiltonian is allowed to evolve in time.

$$\mathcal{H} = \mathcal{H}(t) \tag{1.88}$$

If the Hamiltonian varies very slowly then a particle in nth eigenstate $|n(0)\rangle$ of the initial Hamiltonian $\mathcal{H}(\mathbf{x}, 0)$ should remain in the nth eigenstate $|n(t)\rangle$ of the Hamiltonian at a later time $\mathcal{H}(\mathbf{x}, t)$. Here the vector $\mathbf{x}$ describes the parameters which the Hamiltonian depends (e.g. position, angle, etc.). This is the basis of the so-called *adiabatic approximation.* [†] Given the adiabatic approximation, it is possible to show that the following $|n(t)\rangle$ may be related to $|n(0)\rangle$. [29]

$$|n(t)\rangle = e^{i[\theta_n t + \gamma_n(t)]}\, |n(0)\rangle \tag{1.89}$$

Here $|n(t)\rangle$ only picks up a few phase factors.

$$\begin{aligned} \theta_n(t) &= \frac{-1}{\hbar} \int_0^t \epsilon_n(t')dt \\ \gamma_n(t) &= i \int_0^t \left\langle n \middle| \frac{\partial}{\partial t} n \right\rangle dt \end{aligned} \tag{1.90}$$

Here $\theta_n(t)$ is the *dynamic phase factor* which accounts for the the time evolution of the state $|n\rangle$, and $\gamma_n(t)$ is the geometric phase factor which accounts for the time evolution of the Hamiltonian $\mathcal{H}$. [‡] Expanding the partial derivative in the inner product in the geometric phase, one arrives at the following

$$\gamma_n(t) = i \int_{\mathbf{x_i}}^{\mathbf{x_f}} \langle n|\, \nabla_{\mathbf{x}} n\rangle\, d\mathbf{x} \tag{1.91}$$

Here $\mathbf{x_i}$ and $\mathbf{x_f}$ describe the initial and final states of the Hamiltonian. If a closed path C is taken in parameter space, then the integral above becomes.

$$\gamma_n(t) = i \oint_C \langle n|\, \nabla_{\mathbf{x}} n\rangle\, d\mathbf{x} \tag{1.92}$$

This describes the Berry phase of a particle, and it is in general not zero. If a particle in state $|n\rangle$ is brought on a closed loop through various positions in parameter space it picks up a phase factor which is related to the geometry of that space.

For the case of graphene, it is interesting to evaluate the Berry's phase on a path through phase space which compasses the points K and K'. Consider an electron in an eigenstate of the tight binding Hamiltonian $|\pm\rangle$ which is near a Dirac point described by the vector δk. If δk is allowed to rotate around the Dirac point and brought back to its original position, then its Berry phase may be calculated as follows. [30]

$$\gamma_n = i \oint_C \langle\pm|\, \frac{d}{d\theta}\, |\pm\rangle \cdot d\theta \tag{1.93}$$

---

[*] This is simply the full Hamiltonian with $\epsilon_D(\delta\mathbf{k})$ substituted for $\epsilon(\delta\mathbf{k})$

[†] It should be stated that such a system does not conserve energy. By changing the Hamiltonian slowly, and allowing the particle to adjust to its surroundings, work is being done. Mathematically $\mathcal{H}(\mathbf{x}, t)\, |n(t)\rangle \neq \mathcal{H}(\mathbf{x}, 0)\, |n(0)\rangle$

[‡] Note that in the case of a single particle $|n\rangle$ in a static system, then $|n(t)\rangle = e^{i\epsilon_n t/\hbar}\, |n(t=0)\rangle$. The dynamic phase factor is only a generalization of this concept.

Evaluating the inner product, one has that

$$\begin{aligned}\langle\pm|\frac{d}{d\theta}|\pm\rangle &= \frac{1}{2}\left[1, \pm e^{-i\xi\theta}\right]\frac{d}{d\theta}\begin{bmatrix}1\\ \pm e^{-i\xi\theta}\end{bmatrix}\\ &= \frac{1}{2}\left[1, \pm e^{-i\theta(\mathbf{k})}\right]\left[\ 0, \mp i\xi e^{i\theta(\mathbf{k})}\ \right]\\ &= \frac{-\xi i}{2}\end{aligned} \tag{1.94}$$

Substituting into the integral, one has

$$\gamma_n = i\oint_0^{2\pi}\frac{-i\xi}{2}d\theta = \xi\pi \tag{1.95}$$

Thus one finds that the points K and K' states have opposite Berry phase. The Berry phase of $\pm\pi$ is ultimately what is responsible for the famous *half integer Quantum Hall Effect* which has been observed in mono-atomic graphene [28, 31]. A full treatment of the physics QHE may be obtained with perturbation theory of the low energy Hamiltonian in the case of a strong magnetic field.

Chapter 2

Electronics in Graphene Like Systems

In order to fully grasp the field graphene, one is forced to widen ones scope from the study of the ideal graphene system. Most of the physics in graphene or graphene like systems can be readily understood by generalizing the results of the monolayer structure studied in the previous chapter. In this chapter, we will encounter bi-layer graphene, the macroscopic electronic properties of graphene, and some remarks regarding electron transport in both monolayer and bilayer graphene. The bilayer case will be treated by considering two monolayers and allowing them to couple. The aim of this section is to understand the underlying theoretical concepts motivating current areas of research. Therefore quantum mechanical description will ultimately meet with statistical mechanics to provide a sketch of the macroscopic physical properties as they relate to the microscopic description. Microscopic processes will be related to macroscopic measurable quantities.

2.1 Bi-layer Graphene

A bilayer can be formed by placing two monolayer lattices (denoted A and B) in the manner shown in Figure 2.1.

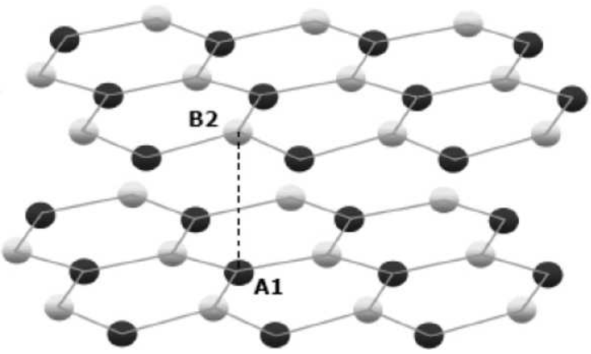

Figure 2.1: A diagram showing the structure of a graphene bilayer. The a and b sublattices are shown in black and grey as before. The layer stacking here shows the a atoms of the first layer under the b atoms of the second layer. This stacking arrangement is energetically favorable, and is known as ab-stacking (or Bernal stacking).

This is known as $A \to B$ stacking. Again black atoms represent the a sublattices of the layers, and grey atoms represent the b sublattices of the layers. In the discussion that follows, the layers will be referred to with capital letters and the sublattices with lowercase letters. In this section, we will generalize the case of the single layer graphene Hamiltonian to the case of of bi-layer graphene. In this way it will be possible to calculate the band structure of a graphene bi-layer .

2.1.1 The Bi-layer Low Energy Hamiltonian

Now because the A and B lattices are both monolayer graphene lattices they have identical low-energy Hamiltonians $\mathcal{H}_m$. Here the valley index has been chosen such that $\xi = 1$.

$$\mathcal{H}_m = \hbar v_f \delta\mathbf{k} \begin{bmatrix} 0 & e^{i\theta(\mathbf{k})} \\ e^{-i\theta(\mathbf{k})} & 0 \end{bmatrix} \tag{2.1}$$

The Hamiltonian for two *non-interacting* monolayers can be constructed by creating a block diagonal matrix

$$\mathcal{H}_b = |\epsilon_{\mathbf{k}}| \begin{bmatrix} \mathcal{H}_{mA} & 0 \\ 0 & \mathcal{H}_{mB} \end{bmatrix} \tag{2.2}$$

Here the indicies A and B indicate the first and second layers. Expanding the Hamiltonian above yields $4x4$ Hamiltonian. It should be noted that matrix elements on the *block diagonal* indicate interactions *within* layers, and matrix elements off the block diagonal indicate interactions *between* layers.

$$\mathcal{H} = \begin{bmatrix} 0 & v_f\hbar|\delta\mathbf{k}|e^{i\theta(\delta\mathbf{k})} & 0 & 0 \\ v_f\hbar|\delta\mathbf{k}|e^{-i\theta(\delta\mathbf{k})} & 0 & 0 & 0 \\ 0 & 0 & 0 & v_f\hbar|\delta\mathbf{k}|e^{i\theta(\delta\mathbf{k})} \\ 0 & 0 & v_f\hbar|\delta\mathbf{k}|e^{-i\theta(\delta\mathbf{k})} & 0 \end{bmatrix} \tag{2.3}$$

The first column/row represents the sublattice of a atoms in the layer A, the second column/row the sublattice of b atoms in the layer A, the third column/row the sublattice of a atoms in the layer B and the fourth column/row the sublattice of b atoms in the layer B. The matrix below illustrates this schematically. Each matrix element describes an interaction energy between the a sublattice and the b sublattice in both layers.

$$\mathcal{H} = \begin{bmatrix} A_a \leftrightarrow A_a & A_b \leftrightarrow A_a & B_a \leftrightarrow A_a & B_b \leftrightarrow A_a \\ A_a \leftrightarrow A_b & A_b \leftrightarrow A_b & B_a \leftrightarrow A_b & B_b \leftrightarrow A_b \\ A_a \leftrightarrow B_a & A_b \leftrightarrow B_a & B_a \leftrightarrow B_a & B_b \leftrightarrow B_a \\ A_a \leftrightarrow B_b & A_b \leftrightarrow B_b & B_a \leftrightarrow B_b & B_b \leftrightarrow B_b \end{bmatrix} \tag{2.4}$$

It should be noted the the diagonal elements of the matrix represent the *self-energy* of each atom (e.g. $(A_a \leftrightarrow A_a) = \epsilon_A a$ is the self energy of atom a in layer A). This will become important in the following section in which a vertical electric field is considered. In this preliminary treatment, the self energy of all atoms will be taken to be zero. Interaction between the layers can be modeled by introducing a term $\gamma_\perp \approx 0.4eV$ which describes a coupling between atom A_b and B_a [23]. Although this is a simple model of the bi-layer system, it will yield most of the essential physics for understanding bi-layers in the context of electronics.

$$\mathcal{H} = \begin{bmatrix} 0 & v_f\hbar|\delta\mathbf{k}|e^{i\theta(\delta\mathbf{k})} & 0 & 0 \\ v_f\hbar|\delta\mathbf{k}|e^{-i\theta(\delta\mathbf{k})} & 0 & \gamma_\perp & 0 \\ 0 & \gamma_\perp & 0 & v_f\hbar|\delta\mathbf{k}|e^{i\theta(\delta\mathbf{k})} \\ 0 & 0 & v_f\hbar|\delta\mathbf{k}|e^{-i\theta(\delta\mathbf{k})} & 0 \end{bmatrix} \tag{2.5}$$

The eigenvalues of this modified Hamiltonian yields the band structure of a bi-layer near the Dirac points K and K'. Solving the secular equation yields.

$$\epsilon_{\delta\mathbf{k}} = \left(\pm\frac{\gamma_\perp}{2} \pm \frac{\gamma_\perp}{2}\sqrt{1 + \frac{4(v_f\hbar|\delta\mathbf{k}|)^2}{\gamma_\perp^2}} \right) \tag{2.6}$$

This describes a splitting of the energy levels into two bands. Notice that as $\gamma \to 0$ the expression reduces to the monolayer case $\epsilon_{\delta\mathbf{k}} = \hbar v_f|\delta\mathbf{k}|$. In the case where the momentum is small $v_f\hbar|\delta\mathbf{k}| \ll \gamma_\perp$ then one finds four parabolic bands.

$$\epsilon_{\delta\mathbf{k}\to 0} = \begin{cases} +\frac{v_f^2\hbar^2|\delta\mathbf{k}|^2}{\gamma} + \gamma_\perp \\ -\frac{v_f^2\hbar^2|\delta\mathbf{k}|^2}{\gamma} - \gamma_\perp \\ \pm\frac{v_f^2\hbar^2|\delta\mathbf{k}|^2}{\gamma} \end{cases} \tag{2.7}$$

At high momentum, then the bands become linear and the dispersion resembles that of the monolayer case.

$$\epsilon_{\delta\mathbf{k}\to\infty} = \pm v_f\hbar|\delta\mathbf{k}| \pm \frac{\gamma_\perp}{2} \tag{2.8}$$

The effect of a bilayer is to split the band structure such that each momentum has four allowed energies near the Dirac point rather than two. Another interesting feature is that *electrons are no longer massless near the Dirac point.* The effective mass may be calculated by evaluating the second derivative of the energy momentum dispersion.

$$m^* = \pm\frac{\gamma_\perp}{2v_f^2} \tag{2.9}$$

The effective mass is identical in all four bands. [*] The positive sign indicates electron states, while the negative sign indicates hole states.[†] The plots below show the behavior of the dispersion of monolayer graphene (left) and bilayer graphene (right) near the K and K' points.

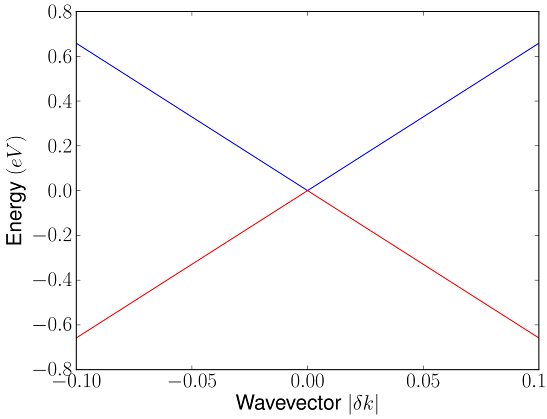

Figure 2.2 *(left)*: The low energy band structure of a monolayer. Note that the dispersion is linear indicating massless Dirac fermions near the K point.

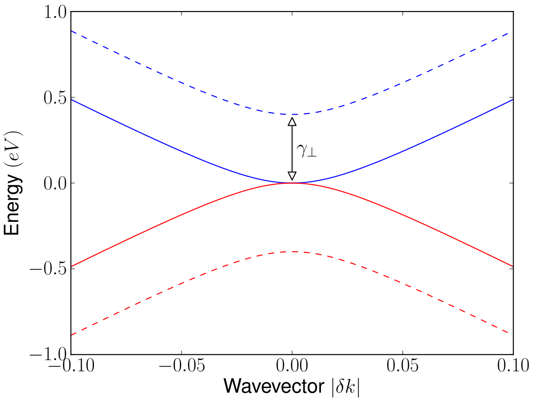

Figure 2.3 *(right)*: The low energy band structure of a bilayer near the K point. There are four bands corresponding to the four energy eigenvalues of the bilayer Hamiltonian. The bands are parabolic for very low energies and linear at higher energies.

2.1.2 Quasi-Degenerate Perturbation Theory of a Graphene Bilayer

It is interesting to further examine what occurs in the massive regime of the bilayer Hamiltonian where $\delta\mathbf{k} \to 0$. To do this, one can use a scheme known as *Lödwin Partitioning.* We begin noticing that the Hamiltonian consists of high energy and low energy terms. One begins by considering two new eigenfunctions $|\theta\rangle$ and $|\chi\rangle$

---

[*] This is not the case in all semiconductors. In *Si* for example, there are several valence bands with different effective masses. They are termed *light holes*, *heavy holes* and *split-off holes.*

[†] A hole is after all an absence of an electron. In this way it is reasonable that its mass should be negative.

which represent the states associated low energy and high energy interactions. Now the initial Hamiltonian can be reorganized to reflect these two new eigenfunctions.

$$\mathcal{H} = \begin{bmatrix} h_\theta & u \\ u^\dagger & h_\chi \end{bmatrix} \tag{2.10}$$

The question then arises as to how to construct the submatricies of $\mathcal{H}$. This is done by discriminating between *low-energy* and *dimer* matrix elements. The dimer matrix h_χ elements are those which deal with the atoms involved in interlayer coupling ($A_b \leftrightarrow B_a$), and the low energy matrix elements h_θ account for the atoms which do not participate in interlayer coupling ($A_a \leftrightarrow B_b$). The matrix u is formed out of the remaining matrix elements. * [8]

$$h_\chi = \begin{bmatrix} A_b \leftrightarrow A_b & B_a \leftrightarrow A_b \\ A_b \leftrightarrow B_a & B_a \leftrightarrow B_a \end{bmatrix} h_\theta = \begin{bmatrix} A_a \leftrightarrow A_a & B_b \leftrightarrow A_a \\ A_a \leftrightarrow B_b & B_b \leftrightarrow B_b \end{bmatrix} \quad u = \begin{bmatrix} B_a \leftrightarrow A_a & A_b \leftrightarrow A_a \\ A_a \leftrightarrow A_b & A_a \leftrightarrow B_a \end{bmatrix} \tag{2.11}$$

Where the matrix elements of $\mathcal{H}$ are constructed from the original Hamiltonian.

$$h_\chi = \begin{bmatrix} 0 & \gamma_\perp \\ \gamma_\perp & 0 \end{bmatrix} h_\theta = \begin{bmatrix} 0 & 0 \\ 0 & 0 \end{bmatrix} \quad u = \begin{bmatrix} 0 & v_f|\mathbf{p}|e^{-i\theta(\delta\mathbf{k})} \\ v_f|\mathbf{p}|e^{i\theta(\delta\mathbf{k})} & 0 \end{bmatrix} \tag{2.12}$$

It follows that $\mathcal{H}$ must satisfy the Schrödinger equation.

$$\begin{bmatrix} h_\theta & u \\ u^\dagger & h_\chi \end{bmatrix} \begin{bmatrix} |\theta\rangle \\ |\chi\rangle \end{bmatrix} = \epsilon_\mathbf{k} \begin{bmatrix} |\theta\rangle \\ |\chi\rangle \end{bmatrix} \tag{2.13}$$

This gives two sets of linear equations, the second row reads as follows.

$$\begin{aligned} |\chi\rangle &= [\epsilon_\mathbf{k} - h_\chi]^{-1} u^\dagger |\theta\rangle \\ &\approx -h_\chi^{-1} u^\dagger |\theta\rangle \end{aligned} \tag{2.14}$$

Here the substitution $[\epsilon_\mathbf{k} - h_\chi]^{-1} \approx -h_\chi^{-1}$ reflects the low energy approximation. Substituting into the first row, one has that.

$$[h_\theta + u h_\chi^{-1} u^\dagger] |\theta\rangle = \epsilon_\mathbf{k} |\theta\rangle \tag{2.15}$$

This is simply an effective Schrödinger equation for the low energy regime of the form.

$$\mathcal{H}_{eff} |\theta\rangle = \epsilon_\mathbf{k} |\theta\rangle \tag{2.16}$$

Substituting in for u,h_θ, and h_χ gives the following effective Hamiltonian. The calculation is eased by the fact that low energy Hamiltonian of monolayer graphene and is therefore Hermetian.

$$\mathcal{H}_{eff} = -\frac{v_f^2|\mathbf{p}|^2}{\gamma_\perp} \begin{bmatrix} 0 & e^{-2i\theta(\delta\mathbf{k})} \\ e^{2i\theta(\delta\mathbf{k})} & 0 \end{bmatrix} \tag{2.17}$$

Where the energy eigenvalues are given by the following.

$$\epsilon_\mathbf{p} = \frac{v_f^2|\mathbf{p}|^2}{\gamma_\perp} \tag{2.18}$$

Here, the low energy Hamiltonian is picking up the two low energy bands of the full Hamiltonian. The high energy bands do not appear because the Hamiltonian was approximated near $\epsilon = 0$. In terms of the effective mass m^*, the Hamiltonian takes a familiar form.

$$\mathcal{H}_{eff} = \frac{|\mathbf{p}|^2}{2m^*} \begin{bmatrix} 0 & e^{-2i\theta(\delta\mathbf{k})} \\ e^{2i\theta(\delta\mathbf{k})} & 0 \end{bmatrix} \tag{2.19}$$

where the prefactor simply gives the classical kinetic energy $T = p^2/2m^*$. In this way, electrons in a bilayer near the points K and K' behave have as classical free electrons. The structure of the low-energy bi-layer Hamiltonian is identical to that of the monolayer case with the exception of the prefactor and a factor of two in the exponent of the phase. In this case, the eigenstates will also pick up the factor of two in their phases. The leads to a Berry Phase of 2π [30].

---

[*] This is only a change of basis from the basis of layers to the basis of low-energies/dimers

2.1.3 Self-Energy, Bandgaps, and Vertical Electric Fields

With the effective Hamiltonian, it becomes possible to estimate the effects of a vertical electric field on a bilayer. Naturally, this only applies when electrons are in the low energy regime. Going back to the full Hamiltonian, one can consider the application of an electric field $\mathbf{E}$ which points vertically from layer A to layer B. Generally, the conduction between layers is poor, such that layer A will be at higher potential than layer B. Let the potential difference between layer A and layer B be Δ such that the self energy of the layer A atoms is $\Delta/2$ and the self energy of the B atoms is $-\Delta/2$. If this is the case, then the full Hamiltonian of a bi-layer can be written.

$$\mathcal{H} = \begin{bmatrix} \Delta/2 & v_f\hbar|\delta\mathbf{k}|e^{i\theta(\delta\mathbf{k})} & 0 & 0 \\ v_f\hbar|\delta\mathbf{k}|e^{-i\theta(\delta\mathbf{k})} & \Delta/2 & \gamma_\perp & 0 \\ 0 & \gamma_\perp & -\Delta/2 & v_f\hbar|\delta\mathbf{k}|e^{-i\theta(\delta\mathbf{k})} \\ 0 & 0 & v_f\hbar|\delta\mathbf{k}|e^{i\theta(\delta\mathbf{k})} & -\Delta/2 \end{bmatrix} \tag{2.20}$$

It is of interest to write a new effective Hamiltonian in the case of an applied electric field proceeding in the same manner as in the last section, the submatricies of the Hamiltonian describing high and low energy interactions take the following form.

$$h_\theta = \begin{bmatrix} \Delta/2 & 0 \\ 0 & -\Delta/2 \end{bmatrix} \quad u = \begin{bmatrix} 0 & v_f|\mathbf{p}|e^{-i\theta(\delta\mathbf{k})} \\ v_f|\mathbf{p}|e^{i\theta(\delta\mathbf{k})} & 0 \end{bmatrix} \quad h_\chi = \begin{bmatrix} -\Delta/2 & \gamma_\perp \\ \gamma_\perp & \Delta/2 \end{bmatrix} \tag{2.21}$$

The effective Hamiltonian calculated on a basis of these new submatricies is given by the following for large values of Δ.

$$\mathcal{H}_{eff} = -\frac{|\mathbf{p}|^2}{2m^*} \begin{bmatrix} 0 & e^{-2i\theta(\delta\mathbf{k})} \\ e^{2i\theta(\delta\mathbf{k})} & 0 \end{bmatrix} + \begin{bmatrix} \Delta/2 & 0 \\ 0 & -\Delta/2 \end{bmatrix} \tag{2.22}$$

From which the energy eigenvalues can be calculated from $\mathcal{H}_{eff}\,|\theta\rangle = \epsilon_{\mathbf{k}}\,|\theta\rangle$. [32]

$$\epsilon_{\mathbf{p}} = \pm\sqrt{\left(\frac{\Delta}{2}\right)^2 + \left(\frac{|\mathbf{p}|^2}{2m^*}\right)^2} \tag{2.23}$$

This describes a splitting of the two parabolic low energy bands in bi-layer graphene. The band gap is then simply given by the difference in the self-energies the A layer and the B layer. At $|\mathbf{p}| = 0$.

$$\epsilon_g = \epsilon_0^+ - \epsilon_0^- = \Delta \tag{2.24}$$

Perhaps most importantly, the band gap in a bi-layer scales linearly with the difference in self-energy between two layers. The possibility of a band gap in a bilayer is a large contrast to the monolayer case. The source of the band gap is ultimately the difference in self energy terms of the arises when two layers are considered to live at different potentials. A bilayer is fundamentally much different than an ordinary semi-conductor insofar as its bandgap scales with the vertical field applied. The plot below shows the band structure of the low energy Hamiltonian with $\Delta = 150meV$ [24, 33, 34].

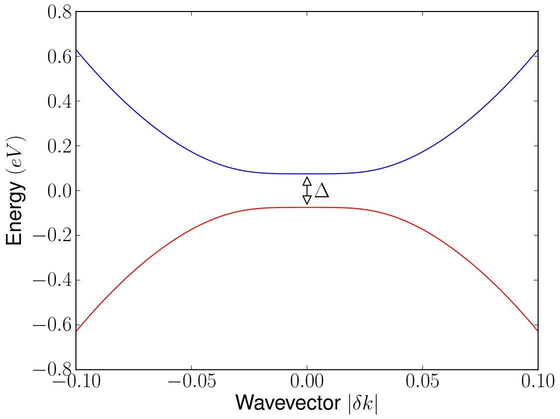

Figure 2.4: A diagram showing the structure of a graphene bilayer under the influence of a vertical electric field. The symmetry breaking in the self energies of the top and bottom layers induces a narrow band gap in the low energy bilayer bandstructure. Band gaps of up to $250meV$ have been reported in the literature on exfoliated bilayers on SiO_2 [33]. A more advanced theoretical treatment predicts a maximum opening of $300meV$ [35, 36].

In a monolayer, it is not possible to induce a band gap with a vertical field. A gap would only occur in a monolayer if the a and b sublattices had different self energies, a condition which cannot be created simply by the application of a vertical field. The absence of a bandgap in monolayer graphene can be seen by calculating the eigenvalues of the monolayer Hamiltonian with the inclusion of self energy terms. The Hamiltonian for a monolayer with equivalent self energies Δ of a and b sublattices takes the following form.

$$\mathcal{H}_m = \begin{bmatrix} \Delta & \hbar v_f \delta \mathbf{k} e^{i\theta(\mathbf{k})} \\ \hbar v_f \delta \mathbf{k} e^{-i\theta(\mathbf{k})} & \Delta \end{bmatrix} \tag{2.25}$$

The eigenvalues are then given by solving the secular equation.

$$\epsilon_{\mathbf{k}} = \pm \hbar v_f |\delta \mathbf{k}| + \Delta \tag{2.26}$$

One has that the whole band structure is shifted by an amount Δ, but its overall form is the same. Thus it can be said that the electronic properties of a bilayer are fundamentally different than that of a monolayer.

2.2 The Density of Electronic States in Graphene

The density of states is a quantity which describes the number of electronic states per unit of **k**-space. Each energy ϵ has a number of states associated in **k**-space associated with it.

$$\rho(\epsilon) = \frac{g_s g_v}{A} \sum_{\mathbf{k}} \delta(\epsilon - \epsilon_{\mathbf{k}}) \tag{2.27}$$

The sum can be evaluated via conversion to an integral. The integral is carried out radially away from the Dirac point in **k**-space.

$$\rho(\epsilon) = \frac{g_s g_v}{A} \frac{A}{(2\pi)^2} \int \delta(\epsilon - \epsilon_{\mathbf{k}}) k dk d\theta \tag{2.28}$$

Here we will calculate the density of states for monolayer and bi-layer graphene. The differential dk can be easily evaluated via the dispersion, and the integral over $d\theta$ will contribute a factor of 2π. In the vicinity of the Dirac point one has the dispersion relation $\epsilon_{\mathbf{k}} = \hbar v_f k$. The differential with respect to the magnitude of $\mathbf{k}$ is then.

$$kdk = \frac{\epsilon_k d\epsilon_k}{(\hbar v_f)^2} \tag{2.29}$$

Substituting and carrying out the integral yields the following for the density of states. A similar calculation from the low energy Hamiltonian of a bilayer is also included.

$$\begin{aligned} \rho(\epsilon)_m &= \frac{g_s g_v}{2\pi} \frac{\epsilon}{(\hbar v_f)^2} \\ \rho(\epsilon)_b &= \frac{g_s g_v}{2\pi} \frac{\gamma_\perp}{(\hbar v_f)^2} \end{aligned} \tag{2.30}$$

Because the bilayer is has a parabolic dispersion, its density of states is constant. From this point is straightforward to obtain the carrier concentration for electrons in graphene. The total carrier concentration is the product number of states in at a given energy ϵ and the probability that a given state is occupied summed over all energies. The Fermi-Dirac distribution determines the probability that a given state at some energy ϵ is occupied.

$$n = \int_0^\infty \rho(\epsilon) f(\epsilon) d\epsilon \tag{2.31}$$

One has for a monolayer and a bilayer respectively [23, 37]

$$\begin{aligned} n_m &= \frac{g_s g_v}{2\pi} \frac{1}{(\hbar v_f)^2} \int_0^\infty \epsilon \cdot f(\epsilon : \epsilon_f, T) d\epsilon \\ n_b &= \frac{g_s g_v}{2\pi} \frac{\gamma_\perp}{(\hbar v_f)^2} \int_0^\infty f(\epsilon : \epsilon_f, T) d\epsilon \end{aligned} \tag{2.32}$$

Plots of the monolayer (left) and bilayer (right) carrier density versus Fermi Energy are shown below in Figures 2.5 and 2.6 for $T = \{100K, 200K, 300K\}$ [37]. The key feature of the bilayer is that it demonstrates carrier densities which are about a factor of two higher than monolayer graphene when the carrier density is high. This is especially important in epitaxial graphene on SiC as the carrier density is usually high. *Generally, a measurement of the carrier density can serve as a preliminary assessment to distinguish between monolayer and bilayer material*

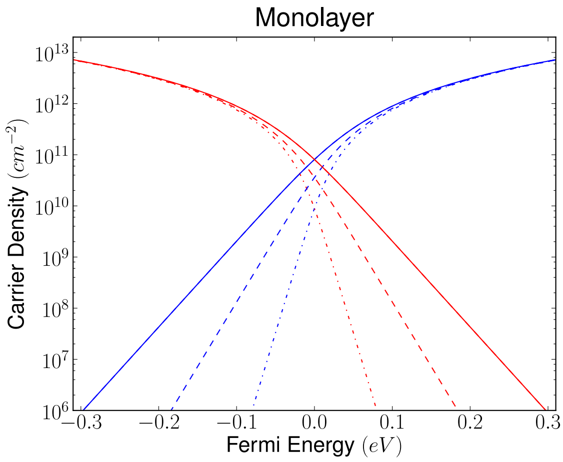

Figure 2.5 *(left)*: A plot of the calculated carrier density versus Fermi Energy in a monolayer for different temperatures. The solid line shows the room temperature carrier density. Lower temperatures give steeper curves. Electron conduction is shown in blue, and hole conduction is shown in red.

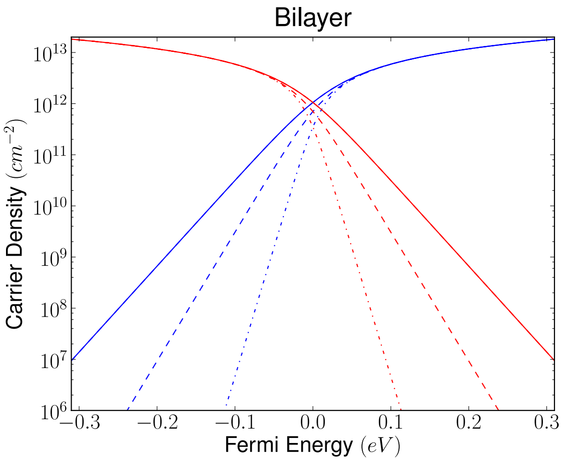

Figure 2.6 *(right)*: A plot analogous to Figure 2.5 for a bilayer. It is important to note that carrier densities in a bilayer are somewhat higher in a bilayer than in a monolayer for the same Fermi Energy.

In the case of zero temperature, the Fermi-Dirac distribution becomes a step function and is unity up to ϵ_f and 0 otherwise. In this case, the carrier densities may be approximated in the following way. Electron conduction is shown in blue, and hole conduction is shown in red.

$$\begin{aligned} n_m &= \frac{g_s g_v}{4\pi} \frac{\epsilon_f^2}{(\hbar v_f)^2} \\ n_b &= \frac{g_s g_v}{2\pi} \frac{\gamma_\perp \epsilon_f}{(\hbar v_f)^2} \end{aligned} \tag{2.33}$$

It is helpful to write explicitly the Fermi-Dirac distribution, as it will return in later examinations.

$$f(\epsilon : \epsilon_f, T) = \left[\frac{1}{1 + e^{(\epsilon - \epsilon_f)/k_b T}}\right] \tag{2.34}$$

The result for hole conduction is similar and differs only by a minus sign from that of electron conduction in the argument of the exponent of the Dirac integral. It is important to note that the term of the $\hbar v_f$ comes directly out of the Hamiltonian, where v_f is proportional to the nearest neighbor energy from the tight binding model γ and the interatomic a_0 spacing. Similarly, the term $\gamma_\perp$ enters into the bilayer result. As a last look at carrier densities, it is useful to plot the intrinsic carrier density ($\epsilon_f = 0$) as a function of temperature.

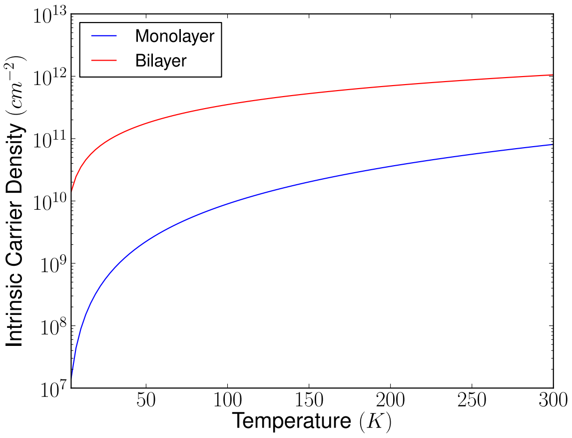

Figure 2.7: A diagram showing the *intrinsic* (zero doping) carrier density as a function of temperature in a monolayer (blue) and in a bilayer (red). Notice how the parabolic dispersion relation gives rise to higher intrinsic carrier densities in bilayer graphene.

2.3 Electron Transport in Graphene

In this section, we examine electron transport in graphene. The objective is to determine how electron transport builds a conductivity within graphene. From the conductivity and the carrier density, it is possible to determine the carrier mobility in graphene by the following relation.

$$\mu = \frac{\sigma}{en} \tag{2.35}$$

It is possible to determine the current density **J** when an electric field **E** is applied via the conductivity σ. The conductivity is generally a tensor indicating that the current may be different along different directions for a given applied field (anisotropy). An example of this is in bilayer graphene where conductivity between layers is typically much lower than within layers. Here we will consider only the current within layers, in which case σ may treated as a scalar quantity.

$$\mathbf{J} = \sigma \mathbf{E} \tag{2.36}$$

In this section, we restrict our attention to the case of very high carrier concentrations. This case is relevant in the treatment epitaxial graphene on SiC. In this regime, a semi-classical approach is justified. This is in contrast to the case of free standing ideal graphene sheets where a quantum conductance model is needed.

2.3.1 The Boltzmann Transport Equations

Transport is a phenomenon which is by definition *non-equilibrium* situation. When an electric field is applied, then electrons will acquire a drift velocity which is proportional to the electric field. Similarly, when the electric field is turned off, there is no current. It should be stated *a priori* that the equilibrium dynamics are given by the Fermi-Dirac distribution. An electron in a material is uniquely described by a position $\mathbf{r}$ and a momentum $\mathbf{k}$ (i.e. a point in phase space) *. and under an external force, these parameters will change. After a time dt one has for the position and momentum of an electron via the classical equations.

$$\begin{aligned} \mathbf{r} + \delta\mathbf{r} &= \mathbf{r} + \langle \mathbf{v} \rangle dt \\ \mathbf{k} + \delta\mathbf{k} &= \mathbf{k} + \frac{\mathbf{F}}{\hbar} dt \end{aligned} \tag{2.37}$$

As our electron charts its course in phase space it occupies various states successively with probability $f(\mathbf{k}, \mathbf{r})$. The wisdom of Boltzmann states that the probability that our electron occupies a given place in phase space $f(\mathbf{r}, \mathbf{k})$ is equal to the probability that it arrives at its next location $f(\mathbf{k} + \delta\mathbf{k}, \mathbf{r} + \delta\mathbf{r})$. †

$$f(\mathbf{r}, \mathbf{k}) = f(\mathbf{k} + \delta\mathbf{k}, \mathbf{r} + \delta\mathbf{r}) = f(\mathbf{r} + \langle \mathbf{v} \rangle dt, \mathbf{k} + \langle \mathbf{v} \rangle dt) \tag{2.38}$$

And thus based on the above equality one has that the total time derivative of f is zero (i.e. the canonical relation of equilibrium dynamics).

$$\frac{df(\mathbf{r}, \mathbf{k})}{dt} = 0 \tag{2.39}$$

Evaluating the total derivative, one finds the following.

$$\frac{df_{\mathbf{k}}(\mathbf{r})}{dt} = \frac{\partial f_{\mathbf{k}}(\mathbf{r})}{\partial t} + \langle \mathbf{v} \rangle \cdot \nabla_{\mathbf{r}} f_{\mathbf{k}}(\mathbf{r}) + \frac{\mathbf{F}}{\hbar} \cdot \nabla_{\mathbf{k}} f_{\mathbf{k}}(\mathbf{r}) \tag{2.40}$$

If our electron is somehow impeded from arriving on its orbit in phase space at its next location (via scattering with other electrons or phonons for example) then we must account for its absence.

$$\frac{df_{\mathbf{k}}(\mathbf{r})}{dt} = \left(\frac{\partial f_{\mathbf{k}}(\mathbf{r})}{\partial t} \right)_{coll} \tag{2.41}$$

Such that the derivative equation reads as follows.

$$\left(\frac{\partial f_{\mathbf{k}}(\mathbf{r})}{\partial t} \right)_{coll} = \frac{\partial f_{\mathbf{k}}(\mathbf{r})}{\partial t} + \langle \mathbf{v} \rangle \cdot \nabla_{\mathbf{r}} f_{\mathbf{k}}(\mathbf{r}) + \frac{\mathbf{F}}{\hbar} \cdot \nabla_{\mathbf{k}} f_{\mathbf{k}}(\mathbf{r}) \tag{2.42}$$

This is the general *Boltzmann Transport Equation*‡. Although the transport equation is in general very difficult to solve, some simplifying approximations can yield valuable physical insight.

---

[*] Phase space is the space of possible potions $\mathbf{r}$ and wavevectors $\mathbf{k}$ in a graphene sheet. The problem is two dimensional, such that there an electron can be uniquely described by its position $\mathbf{r} = [x, y]$ and wavevector $\mathbf{k} = [k_x, k_y]$. Thus, the phase space in graphene is four dimensional. Mathematically, phase space is a closed non-degenerate differentiable 2-form i.e. a simplectic manifold. Any differentiable function $\mathcal{H}$ which lives on a symplectic manifold can serve as an energy function (i.e. a classical Hamiltonian)

[†] This is best describes as causal transport. The assumption is that the initial conditions of the electron determine its path through phase space.

[‡] The Boltzmann Equation should be revered of the most beautiful insights of modern physics.

2.3.2 Near Equilibrium: The Collision Term and the Relaxation Time Approximation

Let us consider a *near equilibrium case*, such that for the distribution function one can write the following.

$$f_{\mathbf{k}}(\mathbf{r}) = f_0 + \delta f \tag{2.43}$$

Here one should have that the perturbative term is small $\delta f \ll f_0$. Now, one should expect that the Boltzmann equation should react *negatively* to such a perturbation such that system has a tendency to return to thermodynamic equilibrium. In the case of spatial uniformity and no external forces, then the transport equation reads.

$$\frac{df_{\mathbf{k}}(\mathbf{r})}{dt} = \left(\frac{\partial f_{\mathbf{k}}(\mathbf{r})}{\partial t}\right)_{coll} \tag{2.44}$$

Now in order to have the system return to equilibrium after some time, one can write for the collision term.

$$\left(\frac{\partial f_{\mathbf{k}}(\mathbf{r})}{\partial t}\right)_{coll} = -\frac{\delta f}{\tau} \tag{2.45}$$

Combining these assumptions, one obtains a simple exponential decay for the time evolution of δf.

$$\delta f(t) = \delta f(0) e^{-\frac{t}{\tau}} \tag{2.46}$$

This is core of the relaxation approximation, that under a small perturbation a system should return to equilibrium. What remains is then to calculate the characteristic time τ which describes the relaxation. Ultimately, this is a quantum mechanical problem, which must be treated with Fermi's Golden Rule. Different relaxation times can be be attributed to different scattering processes. With the relaxation time approximation, the Boltzmann equation can be expressed in the following form. [*]

$$-\frac{\delta f}{\tau} = \frac{\partial f_0}{\partial t} + \langle \mathbf{v} \rangle \cdot \nabla_{\mathbf{r}} f_0 + \frac{\mathbf{F}}{\hbar} \cdot \nabla_{\mathbf{k}} f_0 \tag{2.47}$$

Thus the perturbation from equilibrium δf can be calculated in terms of the distribution at equilibrium f_0. At steady state, the $\partial_t f_0 = 0$ such that the final form that one needs to work with is the following.

$$-\frac{\delta f}{\tau} = \langle \mathbf{v} \rangle \cdot \nabla_{\mathbf{r}} f_0 + \frac{\mathbf{F}}{\hbar} \cdot \nabla_{\mathbf{k}} f_0 \tag{2.48}$$

On the left hand side, one has a the quantum mechanical problem of calculating scattering lifetimes, while on the right hand side one has something resembling Newton's laws.

2.3.3 Solving the Boltzmann Transport Equation

In the steady state and near equilibrium case, it is possible to write a tractable expression for the Boltzmann Transport Equation. This is a matter of evaluating the derivatives of the Fermi Dirac distribution f_0 and invoking the relaxation time approximation. From the perturbation δf it is possible to interpret a wide range of macroscopic phenomena such as carrier mobility, electrical current, and energy transport. These macroscopic problems will of course depend of the relaxation time τ which can be estimated in a variety of cases. Evaluating the derivatives one has the following.

$$\begin{aligned} \nabla_{\mathbf{r}} f_0 &= k_b T \frac{\partial f_0}{\partial \epsilon} \left\{ \frac{\nabla_{\mathbf{r}}\epsilon - \nabla_{\mathbf{r}}\epsilon_f}{k_b T} + [\epsilon - \epsilon_f] \nabla_{\mathbf{r}} \left(\frac{1}{k_b T}\right) \right\} \\ \nabla_{\mathbf{k}} f_0 &= k_b T \frac{\partial f_0}{\partial \epsilon} \mathbf{F} \cdot \langle \mathbf{v} \rangle \end{aligned} \tag{2.49}$$

---

[*] Here we assume that under near equilibrium conditions that $\nabla_{\mathbf{r}} f(\mathbf{r}, \mathbf{k}) = \nabla_{\mathbf{r}} f_0$ and $\nabla_{\mathbf{k}} f(\mathbf{r}, \mathbf{k}) = \nabla_{\mathbf{k}} f_0$

Substituting into the transport equality and recognizing $\mathbf{F} = -\nabla_{\mathbf{r}}\epsilon$ one finds that.

$$\frac{\delta f}{\tau(\epsilon)} = \langle \mathbf{v} \rangle \left(\frac{\partial f_0}{\partial \epsilon} \right) \left\{ -\nabla_{\mathbf{r}}\epsilon_f + T \left[\epsilon - \epsilon_f \right] \nabla \frac{1}{T} \right\} \tag{2.50}$$

Such that the term in braces behaves as a generalized force.

$$\frac{\delta f}{\tau(\epsilon)} = \left(\frac{\partial f_0}{\partial \epsilon} \right) \langle \mathbf{v} \rangle \cdot \mathcal{F} \tag{2.51}$$

The transport equation also picks up a very interesting dependence on the gradient of temperature such that temperature gradients in a material will have a direct effect on electron transport properties. In the case where the sample is at thermal equilibrium, one has that the above reduces to.

$$\delta f = \tau(\epsilon) \left(\frac{\partial f_0}{\partial \epsilon} \right) \langle \mathbf{v} \rangle \cdot -\nabla_r \epsilon_f \tag{2.52}$$

Interestingly, one finds that external force terms do not appear in the above expression. Instead, gradients of the Fermi energy yield the important information. The Fermi energy is nothing more than the product of the electrical potential energy with the fundamental charge. $\epsilon_f = -e\phi$. From electrostatics, one has that.

$$\nabla_{\mathbf{r}}\epsilon_f = -e\nabla_{\mathbf{r}}\phi = e\mathbf{E} \tag{2.53}$$

Thus in the case of an applied electric field, the Boltzmann equation reads as follows.

$$\delta f = -\tau(\epsilon) \left(\frac{\partial f_0}{\partial \epsilon} \right) \langle \mathbf{v} \rangle \cdot e\mathbf{E} \tag{2.54}$$

The current can be then directly obtained from the perturbation δf via the density of states. The physical insight here is that the perturbation is the source of currents in our material. If the external field does not exist, then there are no currents. To obtain the current, one simply sums over all of the states in the first Brillouin zone. The can easily be converted to an integral in energy space via the density of states yielding the *average current*.

$$\begin{aligned} \mathcal{J} &= \frac{1}{A} \sum_k -e\mathbf{v}\delta f \\ &\approx \left[e^2 \int \tau(\epsilon)\rho(\epsilon)\langle \mathbf{v} \rangle^2 \left(\frac{\partial f_0}{\partial \epsilon} \right) d\epsilon \right] \cdot \mathbf{E} \end{aligned} \tag{2.55}$$

One is interested purely in the current along the direction of the electric field. One can make the approximation that $\langle \mathbf{v} \rangle \cdot E \approx |\mathbf{E}| v_f/\sqrt{2}$ such that the integral above becomes.

$$\mathcal{J} \approx \left[\frac{e^2 v_f^2}{2} \int \tau(\epsilon)\rho(\epsilon) \left(\frac{\partial f_0}{\partial \epsilon} \right) d\epsilon \right] |\mathbf{E}| \tag{2.56}$$

From the relation above, the terms in brackets behaves like a scalar conductivity.

$$\sigma = \left[\frac{e^2 v_f^2}{2} \int \tau(\epsilon)\rho(\epsilon) \left(\frac{\partial f_0}{\partial \epsilon} \right) d\epsilon \right] \tag{2.57}$$

A quick solution can be obtained by taking the graphene to be at zero temperature. At zero temperature, the Fermi-Dirac distribution becomes a step function, such that its derivative is a delta function. In this approximation the conductivity is given by the following. [23]

$$\sigma = \left(\frac{e^2 v_f^2}{\epsilon_f} \right) \tau(\epsilon_f)\rho(\epsilon_f) \tag{2.58}$$

In this case, it is possible to write an analytic expression for the mobility.

$$\mu = \frac{\sigma}{en} = \frac{ev_f^2}{\epsilon_f}\tau(\epsilon_f) \tag{2.59}$$

At different temperature regimes, different scattering processes will dominate. Matthiessen's rule can be used to calculate the total effective mobility.

$$\frac{1}{\mu} = \left(\frac{\epsilon_f}{ev_f^2}\right)\sum_i \frac{1}{\tau_i(\epsilon_f)} \tag{2.60}$$

Here, the term $\tau(\epsilon_f)$ will take care of the temperature dependence of the mobility. For acoustic phonon driven relaxation, $\tau(\epsilon_f)$ will introduce a decreasing mobility for increasing temperature. For ionized impurity scattering $\tau(\epsilon_f)$ does *not* introduce dependence such that the mobility is expected to be constant with temperature. Interestingly, the conductivity σ is independent of ϵ_f if the scattering lifetime is independent of ϵ_f. Higher Fermi-levels will tend to give increased conductivity (as well as increased carrier density) indicating that $\tau(\epsilon_f)$ introduces a dependence on the Fermi energy. The mobility carries an inverse dependence on ϵ_f and will thus tend to decrease at higher carrier density. Furthermore, at higher carrier densities there will be more scattering events, such that one can expect shorter relaxation times which will also tend to decrease μ. This will be clarified with experimental results in the following chapter.

2.3.4 Calculating $\tau(\epsilon_f)$: High Temperature Acoustic Phonon Scattering

It is useful to sketch the effects of acoustic phonon scattering in graphene in the high temperature regime in order to provide an example of how $\tau(\epsilon_f)$ can be calculated. In order to calculate the scattering lifetime, one must sum over all possible scattering events. Thus, the Boltzmann equation is an *integrodifferential stochastic equation*. The side dealing with collision events requires an integral, while the side dealing with transport from state to state involves derivatives of a statistical distribution (the Fermi-Dirac function). Here we consider transitions from the state $\mathbf{k}$ to $\mathbf{k}'$ via phonon scattering. The collision derivative may be expressed in the following form.

$$\left(\frac{\partial f}{\partial t}\right)_{coll} = \sum_{\mathbf{k}'} f_{\mathbf{k}'}(1-f_{\mathbf{k}})W_{\mathbf{k}}^{\mathbf{k}'} - f_{\mathbf{k}}(1-f_{\mathbf{k}'})W_{\mathbf{k}'}^{\mathbf{k}} \tag{2.61}$$

The term $W_{\mathbf{k}}^{\mathbf{k}'}$ indicates scattering rate from $\mathbf{k}$ to $\mathbf{k}'$, $f_{\mathbf{k}'}$ indicates the probability that $\mathbf{k}'$ is occupied, and $[1-f_{\mathbf{k}}]$ indicates the probability that $\mathbf{k}$ is unoccupied. The sum indicates that all states must be included. Here we consider the case of microscopic reversibility.

$$W_{\mathbf{k}}^{\mathbf{k}'} = W_{\mathbf{k}'}^{\mathbf{k}} \tag{2.62}$$

Such that the right hand side can be written in terms of the perturbations to the potential.

$$\sum_{\mathbf{k}'} W_{\mathbf{k}}^{\mathbf{k}'}\left[\delta f_{\mathbf{k}} - \delta f_{\mathbf{k}'}\right] \tag{2.63}$$

By the relaxation time approximation, one can recognize

$$\sum_{\mathbf{k}'} W_{\mathbf{k}}^{\mathbf{k}'}\left[\delta f_{\mathbf{k}} - \delta f_{\mathbf{k}'}\right] = \frac{\delta f_{\mathbf{k}}}{\tau(\epsilon)} \tag{2.64}$$

Expanding the δf in the constant electric field case and canceling terms yields the following for $\tau(\epsilon)$.

$$\frac{1}{\tau(\epsilon)} = \sum_{\mathbf{k}'} W_{\mathbf{k}}^{\mathbf{k}'}\left[1 - \frac{\langle \mathbf{v}_{\mathbf{k}'}\rangle \cdot \mathbf{E}}{\langle \mathbf{v}_{\mathbf{k}}\rangle \cdot \mathbf{E}}\right] \tag{2.65}$$

Finally, if $|\langle \mathbf{v}_{\mathbf{k}'} \rangle| = |\langle \mathbf{v}_{\mathbf{k}'} \rangle|$ the ratio of dot products in the sum defines the scattering angle. One can see that events with small scattering angles $\theta_{\mathbf{k}\mathbf{k}'} \sim 0$ do not contribute much to $\tau(\epsilon)$

$$\frac{1}{\tau(\epsilon)} = \sum_{\mathbf{k}'} W_{\mathbf{k}}^{\mathbf{k}'} \left[1 - \cos(\theta_{\mathbf{k}\mathbf{k}'})\right] \tag{2.66}$$

The scattering rate $W_{\mathbf{k}}^{\mathbf{k}'}$ may be calculated by Fermi's Golden rule.

$$W_{\mathbf{k}}^{\mathbf{k}'} = \frac{2\pi}{\hbar} \sum_{\mathbf{q}} |\left\langle \mathbf{k}' \right| \mathcal{H}_{\mathbf{q}} \mathbf{k} \rangle|^2 \Delta(\epsilon, \epsilon') \tag{2.67}$$

The Hamiltonian $\mathcal{H}_{\mathbf{q}}$ is the describes an electron scattering from $\mathbf{k}$ to $\mathbf{k}'$ by a phonon with momentum $\mathbf{q}$. The term $\Delta(\epsilon, \epsilon')$ indicates conservation of energy. [23, 38]

$$\Delta(\epsilon, \epsilon') = N_q \delta(\epsilon - \epsilon' + v_{ph} q) + [N_q + 1] \delta(\epsilon - \epsilon' - v_{ph} q) \tag{2.68}$$

Here N_q is the phonon occupation number. As phonons are bosons, the occupation number is given by the Bose-Einstein distribution. The first and second terms indicate absorption and emission of a phonon with energy $v_{ph} q$ respectively. In the limit of high temperature $k_b T \gg v_{ph} q$ the above relation may be simplified to read.

$$\Delta(\epsilon, \epsilon') = \frac{2 k_b T}{\hbar \omega_{\mathbf{q}}} \delta(\epsilon - \epsilon') \tag{2.69}$$

To simplify the matter of calculating $W_{\mathbf{k}}^{\mathbf{k}'}$, the phonon coupling is often described as coupling to a *single* effective phonon mode. This eliminates the need to evaluate the sum. The matrix element is given by the following.

$$|\left\langle \mathbf{k}' \right| \mathcal{H}_{\mathbf{q}} \mathbf{k} \rangle|^2 = \left(\frac{\hbar}{2 A \rho \omega_{\mathbf{q}}} \right) q^2 \Xi^2 \cos^2 \left(\frac{\theta_{\mathbf{k}\mathbf{k}'}}{2} \right) \tag{2.70}$$

The term in brackets represents normalization and the physics of scattering and momentum conservation is represented by the remaining terms. Combining these results, it is possible to evaluate the scattering time. Converting sums to integrals, and integrating over energy space (via density of states substitution) and scattering angle one finds that the relaxation time evaluates to the following [23].

$$\frac{1}{\tau(\epsilon)} = \left(\frac{1}{\hbar^3} \frac{\epsilon}{4 v_f^2} \frac{\Xi^2}{\rho v_{ph}^2} \right) k_b T \tag{2.71}$$

And thus one has the important result that the mobility should behave as T^{-1}. [39] It is also important to note that at high temperatures the mobility falls off as ϵ^{-1} such that higher carrier densities the mobility will tend to degrade. Experimental results of mobility measurements both with temperature and carrier density confirm both of these trends predicted by the phonon scattering model. It should be noted that although there are many different scattering mechanisms which can occur in graphene, phonon scattering gives a very good qualitative understanding of what occurs at temperatures relevant for electron devices.

2.3.5 Calculating $\tau(\epsilon_f)$: Charged Impurity Scattering

Acoustic phonon scattering is not the only type of scattering that can occur in graphene. It is also of importance to gain some insight into the behavior of $\tau(\epsilon_f)$ for charged impurity scattering. We start again with Fermi's Golden Rule. As with acoustic phonon scattering our primary interest is to obtain an intuition for the temperature dependence of $\tau(\epsilon_f)$. The only difference from the phonon case will be the matrix element which appears inside the sum over $\mathbf{k}'$. Here we express $\tau(\epsilon_f)$ in full with the sum converted to an integral.

$$\frac{1}{\tau(\epsilon)} = \int \frac{d\mathbf{k}'}{(2\pi^2)} \left[1 - \cos(\theta_{\mathbf{k}\mathbf{k}'})\right] \left\{ \frac{2\pi}{\hbar} \sum |\left\langle \mathbf{k}' \right| \mathcal{V}_{\mathbf{k}\mathbf{k}'} \mathbf{k} \rangle|^2 \delta(\epsilon - \epsilon') \right\} \tag{2.72}$$

Here the term in curly braces is the component coming from Fermi Golden Rule. The $[1-\cos(\theta_{\mathbf{k}\mathbf{k}'})]$ is the Boltzmann term coming out of the assumption of microscopic reversibility. The matrix element $|\left\langle \mathbf{k}' \right| \mathcal{V}_{\mathbf{k}\mathbf{k}'}\mathbf{k}\rangle|^2$ represents scattering from $|\mathbf{k}\rangle$ to $|\mathbf{k}'\rangle$ via the potential caused by an impurity, and the sum can be taken to extend over all possible scattering events via impurities from $|\mathbf{k}\rangle$ to $|\mathbf{k}'\rangle$. Now there may be many kinds of impurities in the lattice, but the potential associated with each type of impurity should the same. If n_i is the surface density of the i-th type of impurity and its one can compact the expression for the carrier lifetime.

$$\frac{1}{\tau(\epsilon)} = \left\{ \frac{2\pi}{\hbar} \sum_i n_i \int \frac{d\mathbf{k}'}{(2\pi^2)} \left[1-\cos(\theta_{\mathbf{k}\mathbf{k}'})\right] |\langle \mathcal{V}_{\mathbf{k}\mathbf{k}'}\rangle|^2 \delta(\epsilon-\epsilon') \right\} \tag{2.73}$$

The next step is to evaluate the matrix element $|\langle \mathcal{V}_{\mathbf{k}\mathbf{k}'}\rangle|^2$. Here we will consider charged impurities, such that we will consider scattering from $|\mathbf{k}\rangle$ and $|\mathbf{k}'\rangle$ by a Coulomb potential. It is important to note that we need the Coulomb potential in $\mathbf{k}$-space rather than in real space. The Fourier Transform of the 2D coulomb potential centered at the origin is.

$$\mathcal{V}_q = \left(\frac{2\pi e^2}{\varepsilon q^2}\right) \tag{2.74}$$

Here $q = |\mathbf{k}-\mathbf{k}'|$. Intuitively, $\mathcal{V}_q$ is small when the vector difference between the incoming and outgoing electron is large. The term ε is the effective dielectric polarizability of the graphene layer. For now this will be treated as the mean dielectric constant between the SiC substrate and air $\varepsilon = (\varepsilon_{SiC}+1)/2.\mathcal{V}_q$ will ultimately determine the probability of momentum transfer. Now one needs to calculate the matrix element for scattering. The states $\mathbf{k}$ and $\mathbf{k}'$ are of course the eigenfunctions of the monolayer Hamiltonian with the appropriate phase factor.

$$\begin{aligned} \left\langle \mathbf{k} \right| \mathcal{V}_q \mathbf{k}'\rangle &= \mathcal{V}_q \left\langle \mathbf{k} \middle| \mathbf{k}' \right\rangle \\ &= \mathcal{V}_q \frac{1}{2}\left(1+e^{i\theta_{\mathbf{k}\mathbf{k}'}}\right) \end{aligned} \tag{2.75}$$

Taking the magnitude squared as required by Fermi's Golden rule gives.

$$|\langle \mathcal{V}_{\mathbf{k}\mathbf{k}'}\rangle|^2 = \left(\frac{\mathcal{V}_q^2}{2}\right)\left[1+\cos^2(\theta_{\mathbf{k}\mathbf{k}'})\right] \tag{2.76}$$

An interesting feature of graphene is the impossibility of pure backscattering $\theta_{\mathbf{k}\mathbf{k}'} = \pi$. At this point, there is destructive interference of electron wavefunctions, and the scattering rate drops to zero. putting everything together, one has for the total scattering rate [23].

$$\frac{1}{\tau(\epsilon)} = \left\{ \frac{2\pi}{\hbar} \sum_i n_i \int \frac{1}{\pi}\frac{d\mathbf{k}}{(2\pi)^2}\delta(\epsilon-\epsilon') \int \left[1-\cos^2(\theta_{\mathbf{k},\mathbf{k}'})\right]\left(\frac{\mathcal{V}_q^2}{2}\right) d\theta_{\mathbf{k}\mathbf{k}'} \right\} \tag{2.77}$$

Which for one type of impurity reduces to the following

$$\frac{\hbar}{\tau(\epsilon)} = \left\{ 2\pi n_i \int \frac{d\mathbf{k}}{(2\pi^2)}\delta(\epsilon-\epsilon') \int \frac{1}{2\pi}\left(\frac{2\pi e^2}{\varepsilon q^2}\right)^2 \left[1-\cos^2(\theta_{\mathbf{k}\mathbf{k}'})\right] d\theta_{\mathbf{k}\mathbf{k}'} \right\} \tag{2.78}$$

One can integrate out the delta function yielding a dependence on the density of states, by a change of variables from $\mathbf{k}$-space to energy space. What remains is an integral over the possible scattering angles.

$$\frac{\hbar}{\tau_i(\epsilon)} = \left\{ 2\pi n_i \rho(\epsilon) \int_0^{\pi} \frac{1}{2\pi}\left(\frac{2\pi e^2}{\varepsilon q^2}\right)^2 \left[1-\cos^2(\theta_{\mathbf{k}\mathbf{k}'})\right] d\theta_{\mathbf{k}\mathbf{k}'} \right\} \tag{2.79}$$

The last issue is to resolve the quantity q in terms of the scattering angle. By trigonometry, one has that

$$\frac{q}{2} = k_f \sin\left(\frac{\theta_{\mathbf{k}\mathbf{k}'}}{2}\right) \tag{2.80}$$

Where k_f is the wavevector at the Fermi energy. By the monolayer dispersion relation, one obtains for q.

$$q = \frac{2\epsilon_f}{\hbar v_f} \sin\left(\frac{\theta_{\mathbf{kk}'}}{2}\right) \tag{2.81}$$

Substituting for q in the integral gives the following where n_m is the carrier density of a monolayer.

$$\frac{\hbar}{\tau_i(\epsilon)} = \left(\frac{n_i}{4\pi n_m}\right)\frac{\eta}{\epsilon_f} \tag{2.82}$$

And thus the essential physics has been captured. In the case of pure coulomb scattering, the scattering lifetime depends on the ratio of the carrier density to the density of impurities. For the zero temperature mobility one has then the following relation [40].

$$\mu = \left(\frac{e}{4\pi^2\hbar\eta}\right)\frac{1}{n_i} \tag{2.83}$$

As the density of impurities increases, then the mobility decreases. *Furthermore, the mobility is independent of carrier density if only charged impurity scattering occurs.* Finally it is useful to look at the integral over scattering angles, which is given by the following.

$$\eta = \int_0^{\pi} \frac{1}{2\pi}\left(\frac{2\pi e^2}{\varepsilon}\right)^2 \left(\frac{\hbar v_f}{2\epsilon_f}\right)^2 \frac{\left[1-\cos^2(\theta_{\mathbf{kk}'})\right]}{\sin^2\left(\theta_{\mathbf{kk}'}/2\right)} d\theta_{\mathbf{kk}'} \tag{2.84}$$

It is interesting to note in inverse dependence of η on the polarizability ε. However, complications can arise when $\varepsilon = \varepsilon(\mathbf{q}, T)$. Generally one may interpret this as a charge screening effect. The analysis is identical with the exception that a Yukawa potential is substituted for the Coulomb potential. Some effort is needed to accurately model the Yukawa potential to get the temperature dependence of the screening. The screening effect is known to introduce a temperature dependence on η and thus μ at high temperatures. It is essential to include charge screening effects in order to be able to calculate scattering lifetimes. Regardless, the model outlined here provides qualitative insight into how impurity scattering translates into macroscopic transport measurements [23, 40].

2.3.6 Conclusions on Scattering Phenomena

The simplest possible model of transport phenomena in graphene builds on considering two models, a model based on acoustic phonon scattering and a model based on *long range* Coulomb scattering. In the phonon model it was found that $\tau(\epsilon_f)$ carried a linear dependence in the temperature, giving rise to a linear increase in the resistivity with temperature. The solution was carried out by evaluating Fermi's Golden Rule and integrating with respect to a single effective phonon mode. Furthermore, the phonon calculation revealed a linear dependence on energy, such that resistivity will tend to increase linearly with the carrier density. The long range charged impurity scattering model paints quite a different picture, as $\tau(\epsilon_f)$ and resistivity are constant with temperature in the case of a bare coulomb potential. In this model resistivity scales linearly with the density of impurities n_i. If one considers the effect of charge screening a temperature dependent effect will manifest. It is important to bear these considerations in mind in the following sections, as simple measurements of resistivity and mobility can generate powerful conclusions regarding the transport properties in graphene.

Chapter 3

Experiments on Epitaxial Graphene

With the majority of the fundamental theoretical aspects of graphene behind us, it is now possible to describe the experimental work we have performed on graphene. All of the experimental work discussed here aims at understanding the transport properties in epitaxial graphene. Epitaxial graphene is grown on SiC, and a variety of test structures are fabricated in order to assess the macroscopic mobility, carrier density, electron velocity, contact resistance, sheet resistivity, and other important parameters. [*] In addition to providing insight into the graphene/SiC as a physical system, the experiments are invaluable for the assessment of graphene on SiC for high-frequency electronics applications.

3.1 Epitaxial Graphene: The Graphene SiC System

Epitaxial graphene is typically grown on commercially grown chemo-mechanically polished semi-insulating 4H-SiC or 6H-SiC. All of the material described in the following sections was grown in a horizontal hot wall CVD reactor[41, 42]. The process of graphene growth relies on the process of *graphitization* in which Silicon atoms are sublimated out of the SiC lattice at high temperature. This leaves the surface of the SiC carbon rich and the excess carbon atoms form sp_2 bonded graphene layers. Growth occurs on the (0001) and $(000\bar{1})$ polar faces of the SiC crystal [42]. These are terminated by Si and C atoms respectively. Although growth temperatures may vary, the material reported in the following experiments was grown at a temperature of $1400°C$.

The high growth temperatures needed for the growth of graphene on SiC reflect the poor solubility of Si and C in graphene. Furthermore, from stoichiometry alone, growth of a single graphene layer must deplete 3.19 bi-layers of the SiC structure such that graphene growth tends to generate a significant Si background pressure [43]. Due to the fact that a non integer number of SiC bilayers is required for one sheet indicates that partial bi-layers of SiC must remain at the SiC graphene interface. This will tend to generate a surface with atomic steps which may influence transport properties. Another important factor in the growth of graphene is growth pressure. Graphene can be grown either in vacuum, or in a background pressure of Ar [44] or SiH_4 with different results for each condition. The objective of a background pressure is to control the uniformity of the graphene, the surface morphology, and the number of graphene layers by controlling the sublimation of Si from the surface. When grown under ultra-high-vacuum background pressures can range from $1 \cdot 10^{-6} \sim 1 \cdot 10^{-5}$ mbar [42, 44].

---

[*] Fabrication of devices is discussed in detail in the following chapter.

The graphene layer grown is nearly lattice matched to the Si via the surface reconstruction of $6\sqrt{30}x6\sqrt{30}R30$ while growth on the carbon face can contain many orientations [45, 43]. This refers to how the graphene lattice lives over the SiC lattice. Specifically, the graphene and SiC reciprocal lattices are aligned every $6\sqrt{3}$ multiple of the SiC lattice vectors. In this reconstruction, the graphene lattice vectors are rotated 30° with respect to the SiC lattice vectors. It is important to note that the $6\sqrt{30}x6\sqrt{30}R30$ reconstruction is not perfect, such that the reciprocal lattice vectors of the graphene are slightly longer than in the pristine arrangement. This may be interpreted as a stretching of the SiC primitive basis vectors which define the graphene unit cell. The primitive lattice vectors are of course, related to the interatomic spacing in graphene, such that one can infer that the graphene lattice is under strain. Often the surface is modeled with a simpler $\sqrt{30}x\sqrt{30}R30$ surface reconstruction in experimental work [46].

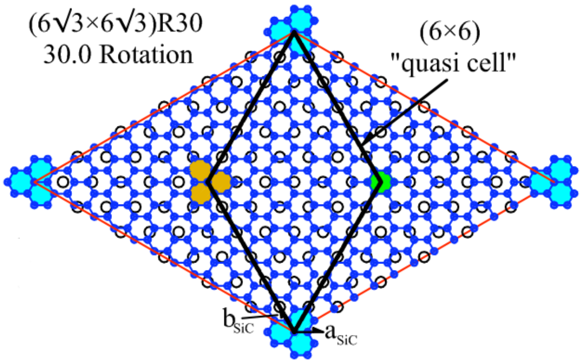

Figure 3.1: A schematic of the $6\sqrt{30}x6\sqrt{30}R30$ surface reconstruction which is most commonly observed in epitaxial graphene on SiC. This diagram is reproduced from p.18 of [43]. The graphene atoms are shown in blue, while open circles represent the underlying SiC lattice structure. Shaded areas represent high symmetry points between the lattices.

The notion of strain can modify the band structure inducing a slight change the coupling coefficient γ which appears in the tight binding Hamiltonian. However, lattice strain in graphene is more important when considering the phonon spectrum. Lattice strain changes the effective spring constant between ionic cores which give rise to phonon modes. [*] From these preliminary considerations it is clear that the graphene-SiC system has the potential to behave much differently than that of theoretical graphene. Nevertheless, many of the concepts presented regarding the band structure and transport can be applied to the graphene-SiC to good approximation.

3.1.1 Hydrogen Intercalation and Quasi-Free Standing Graphene

Graphene grown by graphitization of SiC tends to be strongly coupled to the SiC substrate, and therefore it is expected that the substrate will have a strong influence on the electronic properties of graphene [47]. As was mentioned earlier, graphene growth will generate a terraced surface due to the stoichiometry of graphitization. At high temperature these layers will move to minimize the surface energy of the SiC bulk. Furthermore, the graphene layer will be strongly coupled to the substrate surface. This coupling has the tendency to introduce defects into the graphene layers such that they will be highly irregular. Transport properties are thus expected to be degraded in epitaxial graphene layers. This is especially relavant in the case of a single graphene layer grown on SiC. This highly defected first layer of graphene is usually referred to as *zero layer graphene* or a *buffer layer*. [48, 49]. When multilayer growth is performed, the

---

[*] For this reason lattice strain may induce changes in the Raman spectrum of graphene.

layers above the buffer layer tend to have higher atomic order. It is possible to engineer out the buffer layer by a process known as (H)ydrogen-intercalation. This is done by introducing hydrogen gas at high temperature (typically around $800°C$). When hydrogen is introduced, the buffer layer is isolated from the SiC substrate forming a nearly pristine monolayer[49, 50]. * H-intercalation can be performed by injecting Hydrogen into the growth chamber during the cooling phase of the growth process (i.e. in-situ) or it can be performed in a separate process. In the case of intercalation by a separate process, the intercalation process can be monitored dynamically via Low Energy Electron Microscopy (LEEM) [51]. Several differences are observed between the as-grown and H-intercalated materials. These differences are summarized qualitatively in Table 3.1 [48, 52, 53, 54, 49].

Table 3.1 Values which can be expected from room temperature electron transport measurements. Mobility is shown in cm^2/Vs, sheet resistance in Ω/sq, carrier density in $1x10^{13}/cm^2$, and saturated electron velocity in $1x10^7 cm/s$ [3]. The sign under the carrier density indicates electron (-) or hole (+) conduction.

	μ	ρ_{sh}	n_{sh}	v_{sat}
as-grown	600-1300	1e3-1e4	0.2-0.6(−)	2.0-3.0
H-intercalated	700-2800	2e2-1e3	0.9-2.0(+)	1.5-2.1

H-intercalated material is almost universally heavily p-type, while as grown material is usually found to be n-type. [48] This may be related to the chemistry of intercalation. The bonding between Hydrogen and surface Silicon is a polar bond, such that Hydrogen atoms present a positive potential thus localizing conduction electrons. Since both types of graphene are sensitive to device processing, it is difficult to determine whether variations in transport properties are intrinsic or due to device fabrication. *Most of the experiments described in the following sections focus on the differences in transport properties between as-grown and H-intercalated graphene layers.*

3.1.2 Raman Spectroscopy in Graphene

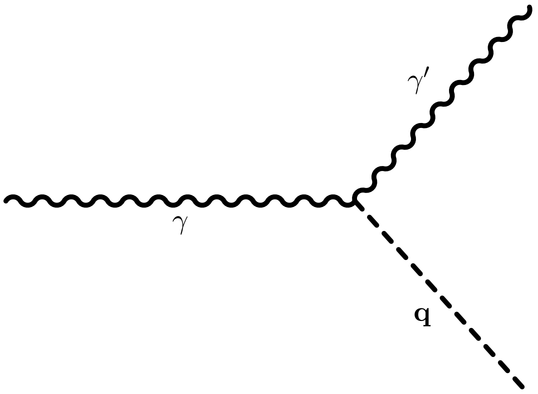

Figure 3.2: A Feynman diagram showing the first order scattering event which generates the G line observed in the Raman spectrum of graphene. An incoming photon scattering inelastically with a zone center phonon.

Since the physics of a monolayer is much different than the physics of a bilayer, it is important to have a method to count the number of layers in graphene. With knowledge of the phonon spectrum (Fig 1.5), the counting of layers may be done with Raman Spectroscopy. Raman spectroscopy is indeed a very rich

---

[*] Thus an H-intercalated zero layer graphene becomes single layer graphene, a single layer becomes a bilayer etc.

topic, and it is useful to outline its fundamental principles. The physics of Raman spectroscopy generally involves the *inelastic* scattering of photons via lattice waves. Consider the general process shown in Fig. 3.2. This process describes a photon with momentum $\mathbf{k}$ and energy $\epsilon_{\mathbf{k}}$ inelastically scattering with a the crystal. A lattice vibration with momentum $\mathbf{q}$ and energy ν is emitted or absorbed. The outgoing photon has a momentum $\mathbf{k}'$ and energy $\epsilon_{\mathbf{k}'}$. By momentum conservation, one has.

$$\hbar\mathbf{k}' = \hbar\mathbf{k} \pm \hbar\mathbf{q} \tag{3.1}$$

In the event of pure backscattering, one has $\mathbf{k}' = -\mathbf{k}$ such that the following holds.

$$0 \leq |\mathbf{q}| \leq 2|\mathbf{k}| \tag{3.2}$$

From the inequality, one has that $\mathbf{q}_{max} = 2|\mathbf{k}|$. Since the photon wavelength (hundreds of nanometers) is much larger than the the lattice constant of the crystal (Angstroms) $\lambda_{\mathbf{k}} \gg \lambda_{\mathbf{q}}$, it follows that $\mathbf{q}$ must be very small on the scale of the Brillouin zone. In general, one may approximate

$$|\mathbf{q}| \approx 0. \tag{3.3}$$

This simple statement is known as the *fundamental Raman selection rule.* [12] It states that Raman scattering may only occur via phonons near which have momenta near the Γ point (i.e. the center of the first Brillouin zone). By energy conservation

$$|\epsilon_{\mathbf{k}'} - \epsilon_{\mathbf{k}'}| = \epsilon_{\Gamma} \tag{3.4}$$

Outgoing photons will thus have an energy shift of $\pm\epsilon_{\Gamma}$. In graphene there are three optical phonons at the Γ point with non-zero energy. One expects to observe three possible energy shifts in the outgoing photon. For photons incident normal to the graphene the electric field points in the xy-plane such that it is only possible to excite lattice waves in the xy-direction. At the Γ point the LO and TO modes have equivalent frequencies ($1580cm^{-1}$). Because of this energy degeneracy, only one shift in the outgoing photon energy is observed. This first order scattering process the origin of the G-peak in the Raman spectrum. The G-peak is doubly degenerate as the LO phonon and TO phonon both produce the same energy shift.

There is a second order optical process which may occur in graphene involving electrons *and* phonons. A photon incident onto graphene may be absorbed forming an electron-hole pair. The electron can of course drop back down into the valence band emitting a new photon, but this photon will have the same energy as the incident photon and no energy shift will be detected. In order to observe a shift, we must cook up scattering process which obeys the Raman selection rule. Given that electrons and holes live near the points K and K' The question naturally arises as to how one may satisfy $|\mathbf{q}| \approx 0$.[13].

Let us begin by considering an electron-hole pair generated in the K valley by an incoming photon with momentum $\mathbf{k} \approx 0$ and energy $\epsilon_{\mathbf{k}}$. Setting the phonon momentum to zero as before, one has by momentum conservation $\mathbf{k}_e = \mathbf{K}$ and $\mathbf{k}_h = -\mathbf{K}$. Energy conservation yields $\epsilon_e = \epsilon_{\mathbf{k}}/2$ and $\epsilon_h = \epsilon_{\mathbf{k}}/2$. In order to generate an energy shift, the electron pair needs to interact with phonons in such a way that the total momentum after scattering is zero. One possibility to satisfy the selection rule is to consider a double resonant process in which two phonons of equal and opposite momentum are involved. When the electron hole pair is created, momentum and energy conservation looks as follows.

$$\begin{aligned} \mathbf{k}_e + \mathbf{k}_h &= 0 \\ \epsilon_e + \epsilon_h &= \epsilon_{\mathbf{k}} \end{aligned} \tag{3.5}$$

Consider the case where the electron and hole both emit a phonon with momentum $-\mathbf{K}$ and $\mathbf{K}$ respectively. The new electron and hole momenta are then.

$$\begin{aligned} \mathbf{k}_{e'} &= \mathbf{k}_e - (-\mathbf{K}) = 2\mathbf{K} = \mathbf{K}' \\ \mathbf{k}_{h'} &= \mathbf{k}_h - \mathbf{K} = -2\mathbf{K} = -\mathbf{K}' \end{aligned} \tag{3.6}$$

After such a scattering event, one finds that the electron hole pair has effectively scattered into the K' valley. A similar analysis for energy conservation yields the following.

$$\begin{aligned} \epsilon_e' &= \epsilon_e - \epsilon_{\mathbf{K}} \\ \epsilon_h' &= \epsilon_h + \epsilon_{\mathbf{K}} \end{aligned} \tag{3.7}$$

The total momentum and energy after scattering is then.

$$\begin{aligned} \mathbf{k}_{e'} + \mathbf{k}_{h'} &= 0 \\ \epsilon_e' + \epsilon_h' &= \epsilon_{\mathbf{k}} - 2\epsilon_{\mathbf{K}} \end{aligned} \tag{3.8}$$

The first statement indicates that this scattering event conserves momentum as required by the selection rule. If the electron-hole pair recombines after scattering then the result will be a photon with energy $\epsilon_{\mathbf{k}} - 2\epsilon_{\mathbf{K}}$. The energy shift will be $2\epsilon_{\mathbf{K}}$ where $\epsilon_{\mathbf{K}}$ is the energy of a phonon at the K point. This process is illustrated in the Feynman diagram in Figure 3.3. [*] The active K phonon for this process is the TO mode, in which case the energy shift one can expect is $\sim 2680cm^{-1}$. This double resonant scattering process is the origin of the $2D$ peak in the Raman spectrum of graphene.

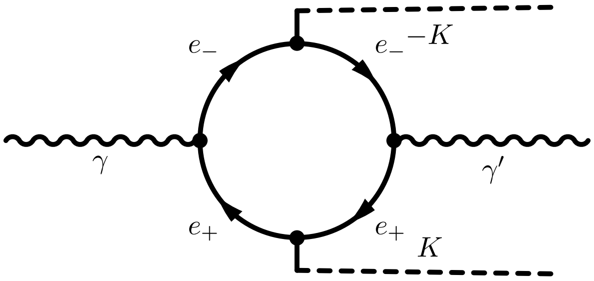

Figure 3.3: A Feynman diagram showing the double resonant scattering even which gives rise to the $2D$ line in graphene. The scattering process conserves momentum via the creation of an electron hole pair. Two scattering events occur with two phonons of equal and opposite momentum at the K and K' points. The total momentum change is zero as required by the Raman selection rule. The $2D$ line is very important for the characterization of the number of layers in graphene.

It should be stated that upon scattering with a phonon, the electron must scatter into a Bloch state with energy $\epsilon_{\mathbf{k}}/2 - \epsilon_{\mathbf{K}}$. Naturally this precludes the electron from scattering into a state at the zone center Γ. Such an event would conserve momentum, but not energy as there is no state near the Γ point with this energy. Therefore the electron must scatter into a K' site. A similar logic applies to the case of the hole scattering events. One should keep in mind that there are many more possible scattering events which can occur in graphene. Here we considered only two processes which conserve momentum. The first order Raman line G arises from ordinary Raman scattering, and the line at $2D$ arises from the strange double resonance in which two phonons of opposite momentum work together with an electron at the point in order to conserve momentum. It is also possible to have *one phonon* scattering events at the K point where a lattice defect takes the role of the second phonon. These defect assisted scattering events produce the so called D line at $\sim 1340cm^{-1}$ [55, 56].

---

[*] The Feynman diagram is the most natural way to represent these scattering events. Holes are the equivalent to positrons in condensed matter theory. Reversing the logic to particle physics, one can say that *the vacuum state is a semiconductor* with $\epsilon_g = 2 * m_e = 1.022MeV$. High energy radiation can decay into electron positron pairs, which behave in a manner very similar to electron hole pairs in solid state theory

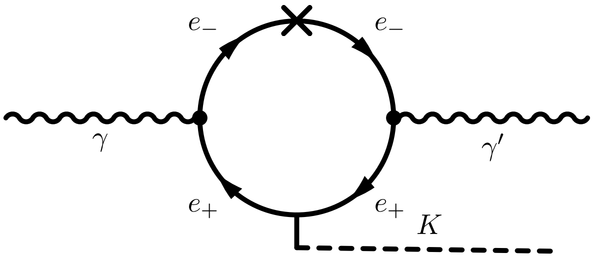

Figure 3.4: A Feynman diagram showing a defect assisted phonon scattering event. A scattering event with a defect takes the place of the one of the phonons in the process shown in Figure 3.3. The D line is thus a good measure of the defects in the graphene lattice. The D line is typically much weaker than the G and $2D$ lines.

Here the Feynman diagram indicates the process for an event which will produce the D line. There is only one phonon involved, so the expected energy shift is only $\epsilon_{\mathbf{k}} - \epsilon_{\mathbf{K}}$. The scattering event with the defect (marked with a cross) is considered to elastic, such that there is a change in momentum, but not in energy. Measuring the D line is a convenient way to assess the quality of graphene layers in terms of the impurity density as a large number of impurities will generate more defect assisted scattering events. It should be kept in mind physically speaking, the G and $2D$ lines have a very different physical origin. There are of course higher order momentum conserving scattering processes as well which involve more phonons.

3.1.3 Layer Counting via the 2D Line

In order to obtain the Raman spectrum of a crystal, one needs a source of photons. Ideally the photons should all have the same energy $\epsilon_{\mathbf{k}}$. For this reason, a narrow linewidth laser is typically used. As laser light is directed onto the surface of the crystal, some of the photons will invariably undergo inelastic scattering events with phonons and electrons producing new photons with shifted energies. The laser light is then passed though a spectrometer to sort out the new energy shifted photons. By analyzing the spectrum of these shifted phonons, the scattering processes which produced them can be inferred. In the case of epitaxial graphene on SiC, one looks for the G, D, and $2D$ lines as a preliminary characterization. There are a few practical difficulties in the case of epitaxial graphene specifically. First, the graphene layer is much thinner than the depth of focus of the optics, such that the graphene spectrum will always come with a background of the SiC spectrum. Careful background subtraction is needed in order to isolate the component of the spectrum due to the graphene. Second, the laser spot must be focused exactly on the surface of the SiC crystal in order to observe the graphene spectrum at all. Since the semi-insulating SiC substrates on which graphene is grown are transparent, achieving good focus of the laser on the surface is challenging.

Despite these issues, Raman spectroscopy has become the *de facto* standard method to count the number of layers in graphene in a non-destructive way. The essence of layer counting involves observing the position and linewidth of the $2D$ Raman line. As the number of layers increases, the $2D$ line tends to broaden. This is connected to the critical difference between monolayers and a bilayers, namely the band structure at the K point. The band structure of a monolayer consists of two bands with a linear dispersion, while a bilayer consists of four bands with parabolic dispersion in the low energy regime and linear dispersion in the high energy regime. Superficially, more bands equates to more allowed $2D$ scattering events and therefore a wider $2D$ Raman line. Figure 3.5 illustrates the origin of broadening in a bilayer.

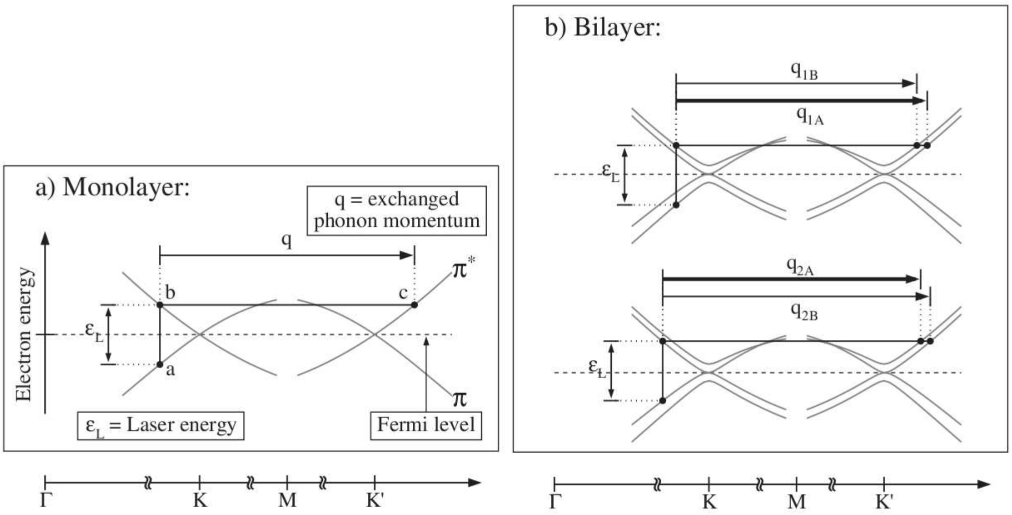

Figure 3.5: A diagram showing the intervalley scattering processes involved in the $2D$ line for a monolayer (left) and a bilayer (right). In a monolayer, there is only one state for K electrons to scatter into in order to satisfy the Raman selection rule. Thus one expects narrow lines in monolayers. In a bilayer, there are more states for K electrons to scatter into such that a broad $2D$ line is observed. Thus a measurement of the Raman spectrum is an indirect measurement of the band structure, which in turn yields information regarding the number of graphene layers. It should be noted that further broadening is observed for multilayer graphene [13].

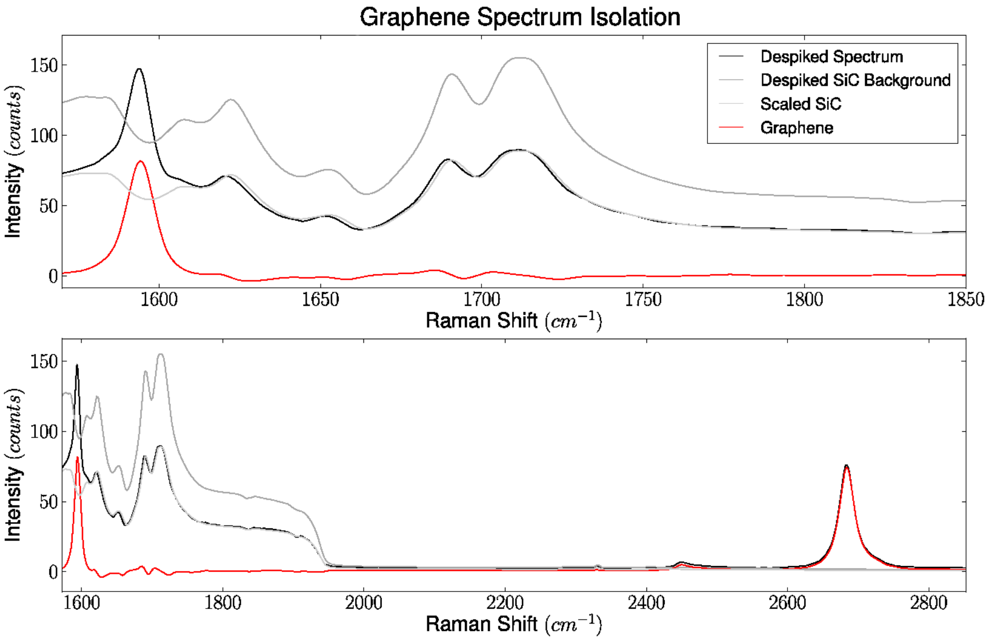

Figure 3.6: A plot of the measured Raman spectrum of H-intercalated epitaxial monolayer graphene on SiC. The region near the G peak (top) and the full spectrum (bottom) are shown. Four spectra are shown in order to demonstrate the complexity of the background subtraction process which is required as the full spectrum contains both a graphene and an SiC component. Accurate background subtraction is especially important for the isolation of the G peak. The final spectrum of graphene is shown in (red). The G peak at $\sim 1580cm^{-1}$ and the $2D$ peak at $\sim 2680cm^{-1}$ are clearly shown in the spectrum.

When an electron hole pair absorbs a photon ϵ_l, there are four possible interband transitions that will conserve momentum via a $2D$ double resonance event. [13, 57] This will, in principle, give four Raman lines which are closely spaced in energy. What will be observed by the spectrometer is the superposition of these four lines, which will manifest as one single wide line. This is slightly different in the monolayer case, where there is only one phonon which can conserve momentum and energy giving rise to a single narrow line. Figure 3.6 shows the G peak and $2D$ peak of monolayer graphene as measured by a $532nm$ semiconductor laser. The SiC background subtraction is also shown. The graphene spectrum is not trivial to isolate. Spikes from cosmic rays are removed by discrete wavelet convolution [58] and the data is smoothed via convolution with a Hanning window. The full spectrum (black) with both graphene and SiC is then scaled to the spectrum of a bare SiC substrate. Finally the SiC component of the spectrum is subtracted leaving the Raman spectrum of graphene shown in red. Background subtraction is especially important for extracting the G peak as there is a strong component of the SiC Raman spectrum at these frequencies. The top subplot shows the G peak isolation, while the bottom plot shows the full spectrum.

From the spectrum, on can see strong G peak corresponding to zone center phonons at $\sim 1580cm^{-1}$. The double resonant $2D$ electron-phonon scattering appears at $\sim 2680cm^{-1}$. Fig 3.7 shows the $2D$ peak of three spectra taken from the same epitaxial graphene on SiC sample shown in Fig. 3.6. The width of the $2D$ peak for regions consisting of a monolayer, a bilayer, and a location where the laser spot is partially on a monolayer region and partially on a bilayer region. From the plot, the broadening associated with bilayer material is very obvious.

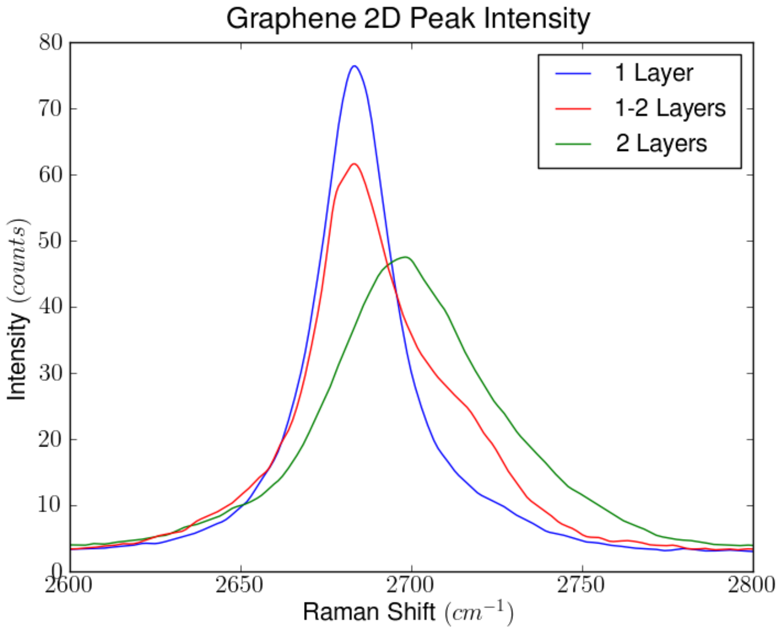

Figure 3.7: A collection of $2D$ peaks taken from several samples. One can clearly see a change in the width of the peak as well as a hardening of the spectrum which is observed for more layers. The 1-2 layer measurement indicates a region where the laser spot lives on the border between monolayer and bilayer regions.

Epitaxial graphene on SiC is peculiar insofar as it consists of many graphene domains with varying numbers of layers. Raman spectroscopy can be used in effect to generate a map of these domains in epitaxial graphene on SiC. From such maps, the domain size, and layer number uniformity can be inferred. Such information is of extreme importance when it comes to characterizing the electronic properties of graphene. In order to characterize graphene on SiC one systematically measures the Raman spectrum of a grid of closely spaced points on the substrate. The G peak and and $2D$ peak can then be extracted and examined separately for each spectrum. These peaks are then fitted to a Lorentzian distribution in order to extract the position, intensity, and linewidth for each point in the array thus generating a map of positions and linewidths.

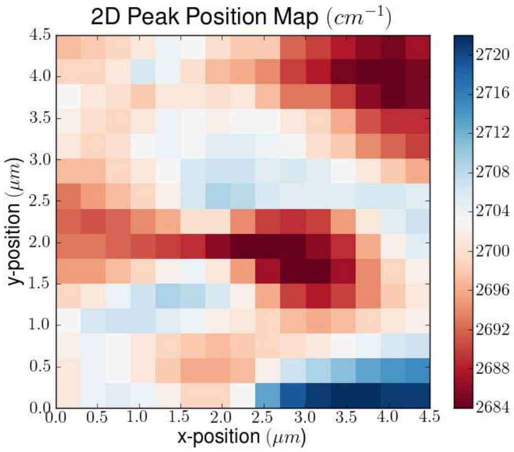

Figure 3.8 *(left)*: A plot showing a map of the position of the center of the $2D$-peak in the Raman spectrum of an epitaxial graphene sample. A small $4.5x4.5\mu m$ region is measured. The laser spot size is $\sim 400nm$ and the step size is $\sim 300nm$

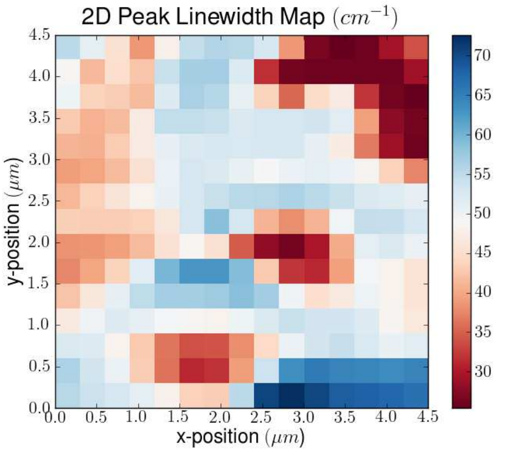

Figure 3.9 *(right)*: An analogous plot to Figure 3.7 where the $2D$ linewidth is mapped. A correlation between the plots emerges in which narrow low energy lines correspond to monolayer regions and wide high energy lines correspond to multilayer regions.

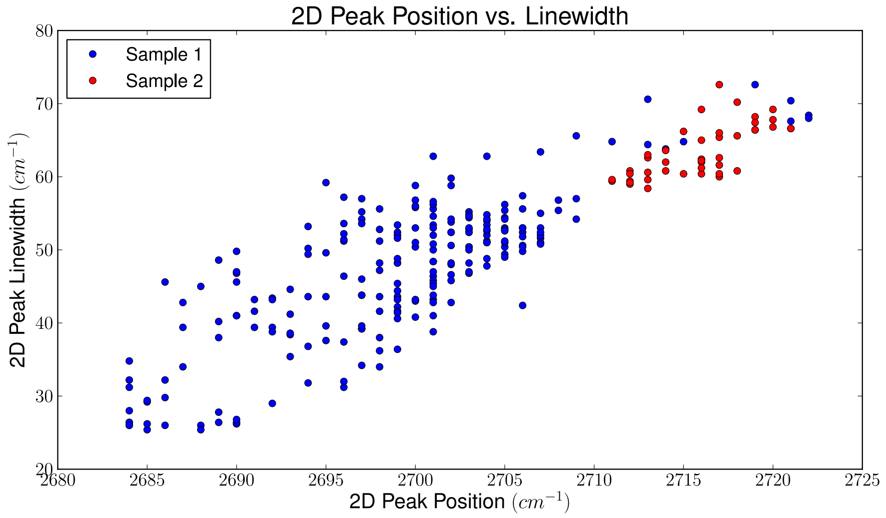

Figure 3.10: A collection of Raman measurements from two samples showing the correlation between linewidth and line position of the $2D$ lines. The lower left corner indicates values typical from monolayer graphene, while the upper right indicates multilayer material.

In Figures 3.8 and 3.9, monolayer material appears in red, bilayer material appears white, and regions corresponding to more layers appear as blue. For this particular sample, it is clear that the number of layers is varying on a scale of μm. It is also interesting to plot the linewidth of the $2D$ peak against its position. Such a plot is shown in Figure 3.10 combining data from two epitaxial graphene samples. An interesting correlation appears between linewidth and peak position. As the linewidth increases (indicating a higher number of layers) one sees a shift of the Raman line position towards higher values. This is a well understood phenomena, as the phonon frequency at the K point is known to be somewhat higher in graphite versus in graphene. On the plot above, *Sample 1* has both monolayer and bilayer regions, whereas *Sample 2* indicates either a highly strained bilayer or multilayer material. [13]

3.2 Mobility Measurements

To first order, there are two dominant modes of scattering in graphene in the context of the Boltzmann transport equation. The first is a long range phenomenon, described by scattering of Bloch waves by a Coulomb potential. In the absence of charge screening, this gives rise to a mobility which is constant with temperature and which scales inversely with the density of ionized impurities. The second mechanism is scattering of Bloch states by acoustic phonons, which gives (in the high temperature limit) a T^{-1} dependence in the mobility as temperature increases. The calculation of the T^{-1} dependence is somewhat naive insofar as it relies on the substitution of a single effective phonon mode in order to avoid summing over the phonon spectrum in the evaluation of Fermi's golden rule. The central point is that decreasing mobilities with temperature are indicative of scattering by acoustic phonons.

3.2.1 Mobility and Resistivity vs. Temperature

The mobility was measured as a function of temperature in one as-grown and one H-intercalated material in a liquid (He)lium cooled cryostat down to $4K$. The measurements were taken on two $100x100\mu m^2$ van der Pauw structures. The results are summarized in the plots below. The as-grown sample is shown in blue, and the H-intercalated sample is shown in red.

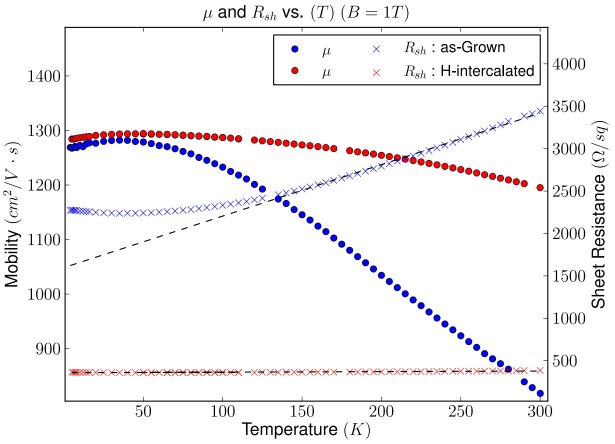

Figure 3.11 *(left)*: A plot of the mobility and sheet resistance measured as a function of temperature on an as-grown (blue) and H-intercalated (red) sample. The as-grown resistivity shows a linear increase in resistivity at high temperatures indicating that phonon scattering is occurring, while the H-intercalated material shown a constant mobility indicating that scattering via the surface optical mode will give rise to saturation.

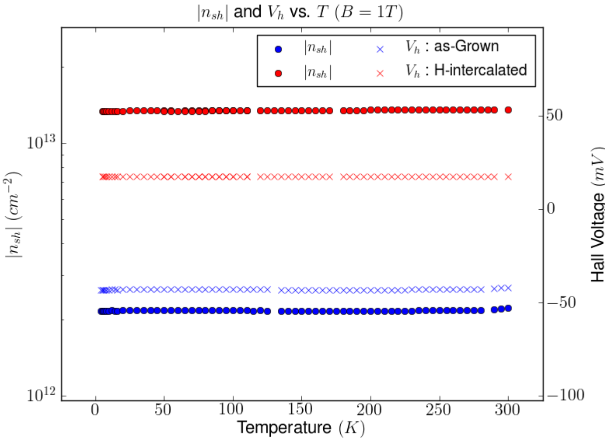

Figure 3.12 *(right)*: Data from the same measurements showing the carrier density and Hall Voltage of as-grown and H-intercalated material. The carrier density is constant in both cases which is indicative of the high Fermi-level regime. The Hall Voltage is negative for as grown material indicating electron conduction, and positive for H-intercalated material indicating hole conduction.

It useful to examine the plots in the context of resistivity. The H-intercalated sample shows a very constant resistance as a function of temperature, while the as-grown sample picks up a linear dependence of resistivity with temperature for high temperatures [39]. Immediately, one can conclude that transport in the H-intercalated sample is primarily limited by long range Coulomb scattering, while in as-grown material, the linear dependence in resistivity with temperature indicates a combination of phonon scattering and Coulomb scattering. Also is shown a plot of the carrier density as a function of temperature along with the corresponding Hall voltage. In both materials the carrier density is essentially constant as a function with temperature as is expected in the case of a high Fermi energy (Figs. 2.5 and 2.6). The Hall voltage in as-grown material is negative indicating that $\epsilon_f > 0$ suggesting electron conduction while in H-intercalated the the Hall Voltage is positive indicating that $\epsilon_f < 0$ suggesting hole conduction. The measured carrier density in as-grown material is $\sim 2.20e12cm^2$ while in H-intercalated material one has $\sim 1.35e13cm^2$.

Due the fact that the carrier density is constant in both materials we will take the *high doping approximation* such that $\epsilon_f(T) = \text{const}$. Calculating the Fermi integral, one has that $\epsilon_f = 171meV$ in as grown material assuming monolayer material, and $\epsilon_f = 248meV$ assuming bi-layer material. [*]

3.2.2 Mobility vs. Carrier Density and Resistivity

The plot below shows a measurement of many $100x100\mu m^2$ van der Pauw structures on two chips of epitaxial graphene on SiC. The first sample is graphene of the as-grown variety (blue), while the second sample is H-intercalated material(red). This measurement is useful as it provides some insight into the statistics of transport properties. Each data point represents a separate Hall measurement.

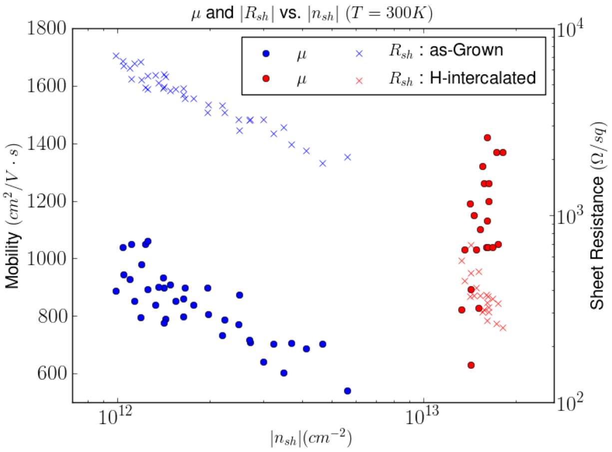

Figure 3.13: Hall statistics taken from many van der Pauw structures fabricated on the same chip. These plots provide insight into the uniformity of the sample. A global mobility can also be estimated by curve fitting. These plots are integral for the extraction of velocity field data.

From the plot, there are several important points which should not escape consideration. First, H-intercalated material has a very uniform carrier density, and a wide dispersion in the measured mobility. Because the mobility in H-intercalated material demonstrates almost no dependence in temperature, transport in H-intercalated samples impurity limited. The immediate conclusion from the above plot then is that the impurity density is varying from structure to structure (and thus generally over the area of the substrate). Because the resistivity demonstrates a factor of three in variation over the area of the substrate, one can assume that the impurity density is varying by a factor of three over the area of the

---

[*] These assumptions are somewhat justified, as these materials were grown in the same conditions. If the intercalated material was a monolayer before intercalation, it would become a bilayer after intercalation as discussed previously.

substrate. This conclusion comes directly from the fact that resistivity scales linearly with the impurity density.

In the as-grown material, one has a strong dependence on the mobility with sheet carrier density. It is important to note that both phonon and impurity scattering pick up a factor which depends on the Fermi energy. In this way, one expects that the mobility varies inversely with the Fermi energy such that higher carrier densities give lower mobility. The resistivity varies inversely with carrier density, such that at higher carrier densities one expects a lower sheet resistance. *From the plot above, it can generally be said that the H-intercalated material is very uniform, whereas the as-grown material demonstrates large variations in the transport properties from structure to structure.*

3.3 The Velocity-Field Characteristic

When an electric field is applied to a graphene sheet, electrons acquire a drift velocity in the direction of the electric field. At low field the velocity of an electron is related to the field via the mobility. For a given temerature and Fermi energy, one can write the following. *

$$\langle \mathbf{v} \rangle = \mu(\epsilon_f, T)\mathbf{E} \tag{3.9}$$

The electron velocity is linear with electric field for a given temperature and Fermi energy. Electron transport is limited by scattering processes described by the relaxation time $\tau(\epsilon_f, T)$ which comes directly out of the Boltzmann Transport equation. However, the velocity of an electron will not tend to infinity as higher-fields are applied. The theoretical maximum velocity that can be achieved is the Fermi velocity $v_f = 1e8cm/s$. This comes directly out of the tight binding Hamiltonian. The electron velocity must somehow saturate at a maximum value of v_f. In general epitaxial graphene demonstrates a high carrier density, such that the maximum velocity v_{sat} will be less than v_f. Generally, to describe this phenomena in the context of the above relation, one introduces a field-dependent mobility $\mu(\epsilon_f, T, |\mathbf{E}|)$ which can be expressed in terms of the low-field mobility $\mu(\epsilon_f, T)$. [59, 1]

$$\mu(\epsilon_f, T, |\mathbf{E}|) = \frac{\mu(\epsilon_f, T)}{\left[1 + \left(\frac{\mu(\epsilon_f, T)|\mathbf{E}|}{v_{sat}}\right)^{\alpha}\right]^{\frac{1}{\alpha}}} \tag{3.10}$$

In this model of the mobility one has that as $|\mathbf{E}| \to \infty$ that $\langle \mathbf{v} \rangle \to v_{sat}$. The physics of the saturation lies in phonons. Electrons can undergo inelastic scattering with the lattice via phonon emission. Higher electron kinetic energies gives rise to more phonons and thus more breaking. These phonons can be either the phonons of the graphene *or* the surface optical phonons of the SiC. If the impurity density is high, then the substrate mode will be the main breaking mechanism. In this case is the surface phonon mode of SiC has an energy $\epsilon_{SO} \approx 115meV$. In impurity dominated samples *surface optical phonon breaking will give rise to velocity saturation as soon as electrons have a kinetic energy of* $115meV$.

In order to measure the velocity field characteristic, $5x10\mu m$ microbridge structures are fabricated on both the as-grown and H-intercalated material presented in the previous section. A pulsed IV approach is taken in order to avoid potential self-heating and charge trapping effects which would otherwise distort the extraction. A measurement of the velocity field characteristic requires four basic steps. First, the geometry of each microbridge must be precisely characterized. This is necessary in order to accurately calculate the electric field in the bridge. Second, the contact resistance must be measured in order to account for the voltage drop across the contacts. This is accomplished by making measurements on TLM structures

---

[*] It should be stated here that μ is related to σ is is therefore most generally a *tensor*. In the case of graphene, the mobility will be treated as not having a dependence on the direction of the field. This assumption may not be valid in epitaxial graphene on SiC as anisotropy may be introduced by step edges.

fabricated on the same chip. * Third, statistics on the transport properties (Fig. 3.13) are needed such that one can estimate the carrier density on a basis of the measured sheet resistance. Finally, pulsed IV measurements are made to obtain the current-voltage curve in the absence of self heating and hysteresis effects. By compiling all of these measurements, it becomes possible to transform the IV characteristic into a velocity-field characteristic. The plots below show an example pulse sequence, and the extracted IV characteristic which is the starting point for the velocity field extraction procedure.

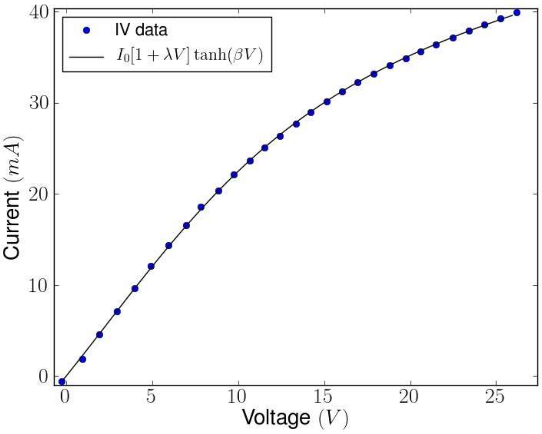

Figure 3.14 *(left)*: The measured IV characteristic extracted from pulsed IV via the convolution method. The IV curve is fitted to Equation 3.9

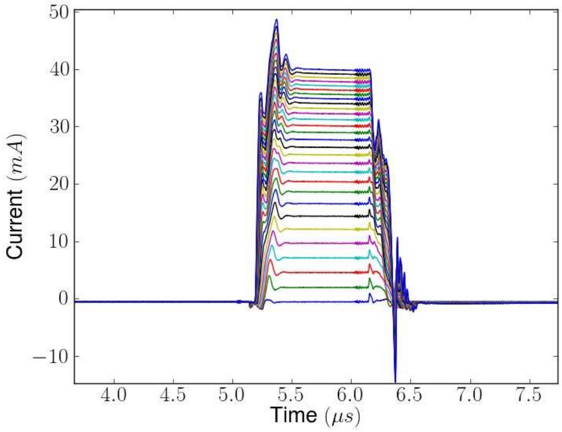

Figure 3.15 *(right)*: The measured current waveforms for applied voltage pulses ranging in amplitude from $0-24V$. Compression in the current pulse ladder at high voltages indicates velocity saturation at high fields.

The current pulses shown above are flat, which indicates that there is minimal self heating for short pulse lengths. For short pulses, the IV characteristic is generally repeatable, and no hysteresis is observed when cycling the voltage amplitude. † The general procedure of extracting the IV characteristic begins by taking the convolution of the current and voltage pulses. An example of a current pulse ladder along with the extracted IV characteristic is shown in Fig. 3.14. For this measurement, voltage pulses from $0V-28V$ are applied and current pulses (Fig. 3.15) are measured. [53]

$$\begin{aligned} \frac{d}{dt}\left[\int V(t)V(t-\tau)d\tau\right] &= 0 \\ \frac{d}{dt}\left[\int I(t)V(t-\tau)d\tau\right] &= 0 \end{aligned} \tag{3.11}$$

These convolutions will generally give triangular waveforms. The time t_0 at the which the convolved waveforms is a maximum will generally be near the center of the real waveforms $V(t)$ and $I(t)$. Then, by selecting $V(t_0)$ and $I(t_0)$ will give a single current point for each voltage. The IV characteristic can then be fitted to the following empirical relationship which is borrowed from MESFET modeling. [60]

$$I = I_0\left[1+\lambda V\right]\tanh\left(\beta V\right) \tag{3.12}$$

The key observation to make here is that the current ladder becomes compressed at high voltages. This is generally indicative of *current saturation* which will translate directly into velocity saturation. One may further interpret the compression in the current ladder at high voltages as a reduction in the carrier mobility at high fields.

---

[*] TLM measurements will be presented in detail in the following section in connection with fabrication technology.

[†] This is quite a contrast to the DC case where a hysteresis is usually observed. The origin of the hysteresis in DC measurements is to this point not well established.

To see how voltages transform into fields, consider the general schematic below which shows the geometry of a microbridge structure. The corner rounding is attributed to photolithography. The geometry will be approximated by the solid lines [61].

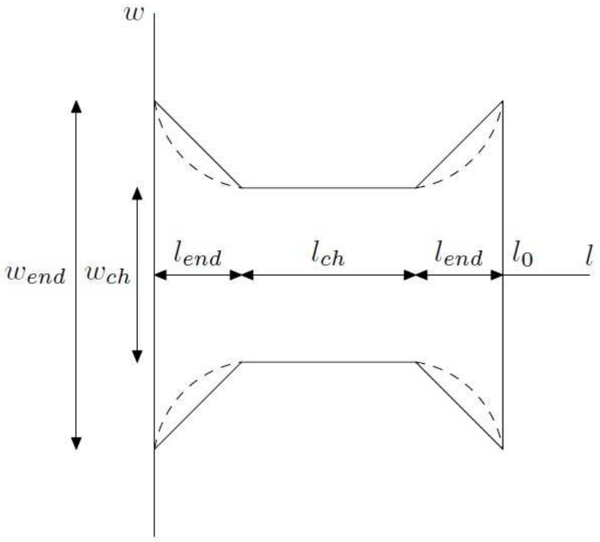

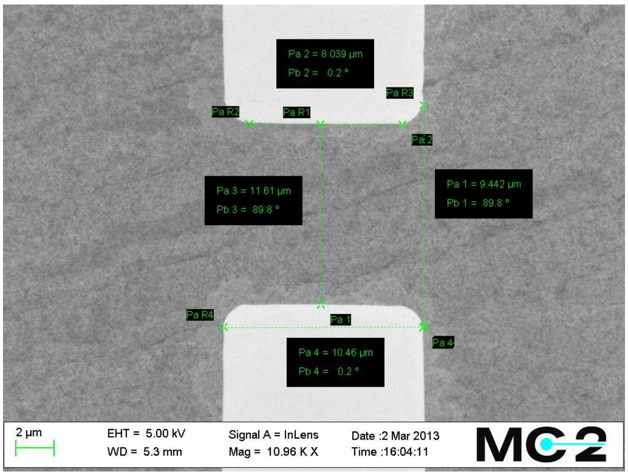

Figure 3.16 *(left)*: The geometry used to estimate the electric field by an integral calculation of Ohms law.

Figure 3.17 *(right)*: A Scanning Electron Microscope image of a graphene microbridge structure before the deposition of contacts.

The calculation of fields begins by considering an integral form of Ohms law. Consider that the *total* resistance can be obtained from the measured IV characteristic.

$$\frac{dV}{dI} = \left\{\lambda I_0 \left[\tanh\left(\beta V\right) + V\beta \mathrm{sech}^2\left(\beta V\right)\right]\right\}^{-1} \tag{3.13}$$

The total resistance has a contribution from the contacts R_c and the graphene microbridge R_{mesa}. Here $R_c = \rho_c/w_c$ is the total resistance of the contact. If the sheet resistance ρ_{sh} is assumed to constant for the entire microbridge structure, then one can express R_{mesa} as an integral over the geometry of the sheet.

$$\frac{dV}{dI} = \left[2R_c + \rho_{sh}\int_0^{l_0} \frac{dl}{w(l)}\right] \tag{3.14}$$

The integral is over the length of the microbridge structure l_0, and $w(l)$ is the varying width of the sheet. The integral on the right hand side behaves as a *form factor* and is a generalization of the number of squares of the sheet. R_c is the contact resistance which is measured on separate TLM structures. Integrating over the geometry shown one has that the sheet resistance. [53]

$$\rho_{sh} = R_{mesa}\left[\frac{2\log(w_{end}/w_{ch})}{\tan(\theta)} + \frac{l_{ch}}{w_{ch}}\right]^{-1} \tag{3.15}$$

Here θ is the *current spreading angle*, which is given by the following. [61]

$$\tan(\theta) = \frac{2l_{end}}{w_{end} - w_{ch}} \tag{3.16}$$

It is useful to consider the *straight channel case* in which $w_{end} = wch$ and $l_{end} = 0$. In this case the sheet resistance simplifies to the familiar form.

$$R_{mesa} = \rho_{sh}\frac{l_{ch}}{w_{ch}} \tag{3.17}$$

As mentioned earlier, one needs to account fully for the geometry of the sheet in order to obtain the correct sheet resistance given the IV data. Finally one can calculate the electric field in the following way. [*]

$$|\mathbf{E}| = \frac{V_0 - 2I_0[R_{end} + R_c]}{l_{ch}} \tag{3.18}$$

Currents can be translated into drift velocities by considering the drift velocity of carriers in a current carrying sheet.

$$v_d = \frac{I}{en_{sh}w_{sh}} \tag{3.19}$$

There is a slight difficulty that v_d depends on the carrier density n_{sh}. However, in the consideration of transforming voltages into electric fields, the sheet resistance was obtained from the IV characteristic. From Hall statistics, it is possible to obtain by curve fitting the relationship between sheet resistance and carrier density $n_{sh} = [e\rho_{sh}\bar{\mu}]^{-1}$. The average mobility can be obtained either by fitting the Hall data, or via microwave reflectivity measurements taken prior to fabrication. Given the sheet resistance, it is thus possible to estimate the carrier density n_{sh}. The assessment of carrier density is especially important in as-grown material due to non-uniformity issues. The closed form expression for the drift velocity in terms of the measured IV characteristic is then given by the following.

$$v_d = I \cdot \left[\frac{\rho_{sh}\bar{\mu}}{w_{ch}}\right] \tag{3.20}$$

As in the case of the field extraction one muse be careful to correct for the geometry. The mobility in the above formula is the low field mobility. This relation assumes that the carrier density remains constant up to high field. Putting everything together one has the velocity field curves. Below is a plot showing the velocity field curves for both as-grown and H-intercalated material as a function of temperature. [53]

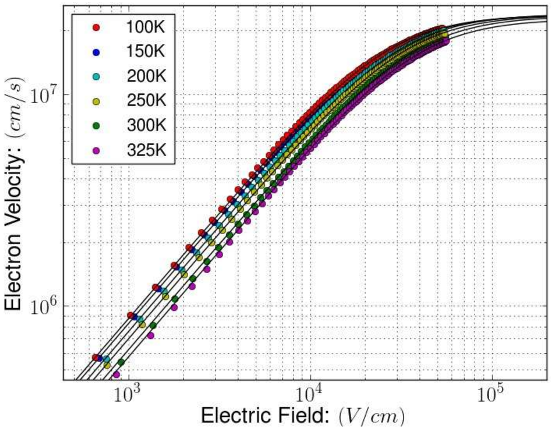

Figure 3.18 *(left)*: The extracted velocity field curves for as-grown material from pulsed IV and ancillary measurements at different temperatures. The plot indicates a temperature dependent mobility and saturated velocity.

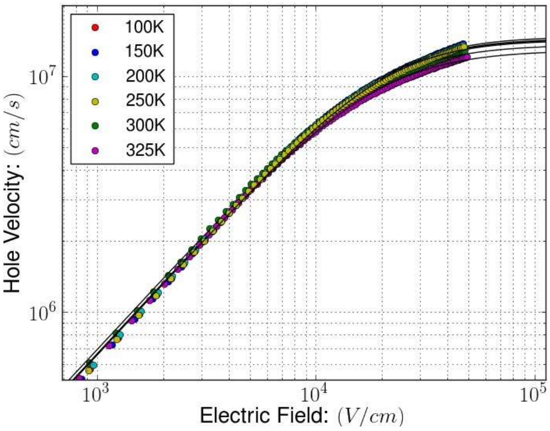

Figure 3.19 *(right)*: The velocity field characteristic of H-intercalated material in analogy to Figure 3.19. Here the mobility and saturated velocity demonstrates a very weak dependence on temperature.

These plots are then fitted to the empirical velocity field model presented at the beginning of the chapter in order to extract a low-field carrier $\mu(T)$ mobility and a saturated velocity $v_{sat}(T)$ of the microbridge. Table 3.2 compares the results of the extraction to the same values in several other semiconductor materials.

---

[*] One should be careful here. The assumption that the contact resistance is constant may not be appropriate at high field. In the extractions which follow, the R_c is assumed to be constant.

Table 3.2: A comparison of the parameters of the above fits to those of other well characterized materials at $300K$. The critical field is also reported indicating the field above which the electron velocity can be considered as saturated. Here v_{sat} is reported in (cm/s), μ in $(cm^2/\cdot s)$ and $\mathcal{E}_{sat}$ in (kV/cm). The data for Silicon corresponds to n-type doping with a carrier concentration of $n = 10^{15} cm^{-3}$. The data for GaN corresponds to n-type doping with a carrier concentration of $n = 10^{17} \sim 10^{19} cm^{-3}$. The values reported for GaAs represent the peak electron velocity and corresponding electric field as GaAs demonstrates a velocity overshoot effect. Figures for GaN are include measurements on AlGaN/GaN heterostructures and bulk GaN substrates. These values also indicate the peak velocity.

	as-Grown [53]	H-int [53]	4H-SiC[61]	AlGaN/GaN[62]	GaN[62]	Si	GaAs[63]
v_{sat}	2.3e7	1.4e7	1.6e7	3.1e7	2.5e7	1.0e7	2.1e7
μ	630	700	130	430	250	1400	7500
$\mathcal{E}_{sat}$	37.0	19.4	123.7	72.0	100.0	7.1	2.8
α	1.80	1.85	-	-	-	2.0	-

Figs. 3.18 and 3.19 indicate the mobility of the H-intercalated material is constant in temperature, while the mobility in as-grown material decreases with increasing temperature. As mentioned earlier, these qualitative effects agree well with the notion that transport H-intercalated material is impurity limited, while transport in as-grown material is phonon limited. In both the case of as-grown and H-intercalated material, one has that $v_{sat} \ll v_f$. Plotting the extracted mobility and sheet resistance versus temperature, one has the following. Note the qualitative similarity to the cryostat measurements presented in Fig 3.11.

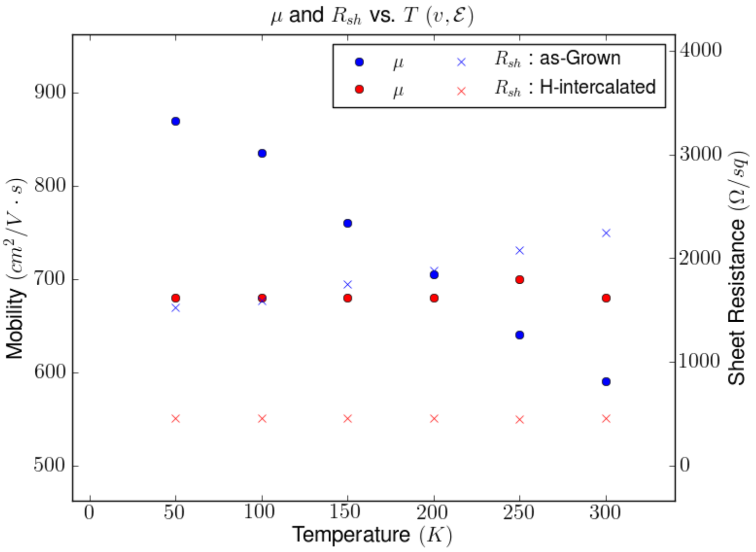

Figure 3.20: The extracted mobility and sheet resistance versus temperature dependence for as grown and H-intercalated materials. This figure should be understood in connection with Figures 3.11 and 3.12.

3.3.1 The H-Intercalated Speed Limit

It is also interesting to examine the temperature dependence of the extracted saturated velocity. In both the case of as-grown and H-intercalated material, the observed temperature dependence is very weak such that $v_{sat}(T) \sim$ const. In the case where one has impurity dominated transport at low-field the mobility is approximately constant $\mu(T) \sim$ const. *It is important to clarify that we are interested in what causes the mobility to change at high field.* Evidently by going to high field, one is inviting scattering events which cannot occur at low field due to energy conservation. Naturally, these high energy processes do contribute to the low field mobility. With a constant low field mobility (the impurity scattering case), it is possible to express the saturation velocity in terms of the surface optical phonon energy ϵ_{SO} in SiC [54, 64, 65].

$$v_{sat} = \frac{2}{\hbar}\frac{\epsilon_{SO}}{\pi\sqrt{\pi n}}\sqrt{1 - \frac{\epsilon_{SO}^2}{4\pi n(\hbar v_f)^2}}\frac{1}{N_{OP}+1} \tag{3.21}$$

N_{OP} is the phonon occupation number which is given by the following. [65, 23]

$$N_{OP} = \frac{1}{e^{\epsilon_f/k_bT} - 1} \tag{3.22}$$

At this point one approaches the notion of substrate limited transport [47, 66, 67]. The model assumes that v_{sat} is limited by elastic emission of optical phonons with energy ϵ_{SO}. It is valid for phonons in the graphene *and* in the substrate. Realistically, it is the lowest energy phonon which must be considered. In the graphene SiC system, the lowest energy phonon is the substrate surface optical mode [68]. When the average kinetic energy of charge carriers becomes high, these modes will be excited effectively turning on velocity saturation [69]. In the event that the chemical potential is high relative to the thermal energy $\epsilon_f \gg k_bT$ then $N_{OP} \approx 0$ so that v_{sat} becomes constant as a function of temperature. For $n \approx 1e13$ then the term under the square root is approximately unity. In this case it becomes possible to extract the surface phonon energy in SiC directly given the measured saturated electron velocity.

$$\epsilon_{SO} = \left(\frac{\pi\sqrt{\pi}}{2}\right)\sqrt{n}\hbar v_{sat} \tag{3.23}$$

The structure of the Eq.3.23 is telling. The $\hbar v_{sat}$ and $\sqrt{n}$ term behave as an energy and an inverse length λ^{-1} respectively. In this way, Eq.3.23 is entirely analogous to the familiar $\epsilon = \hbar c/\lambda$. The prefactor is a geometry term resulting from integration over scattering events in **k**-space.

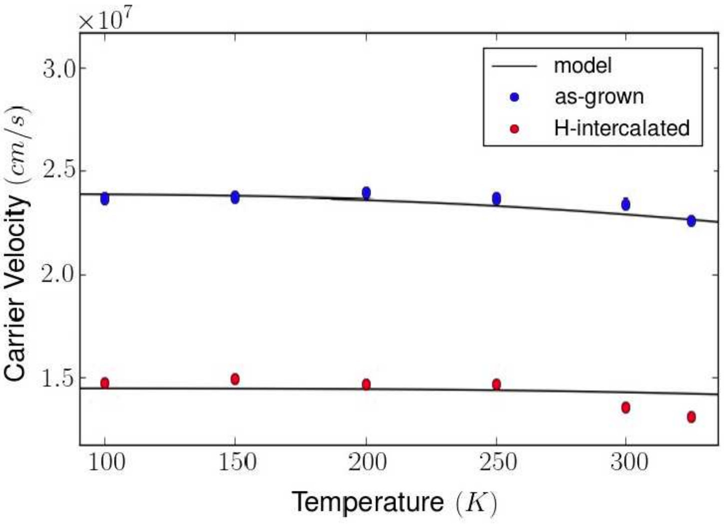

Figure 3.21: A plot of the temperature dependence of the saturated carrier velocities and fits to Eq.3.21. The fitting is used to provide an estimation of the ϵ_{SO} phonon in SiC. The value extracted for H-intercalated material seems to validate the assumption that impurity scattering dominates in H-intercalated material. This assumption is not valid in as-grown material in which mobility data suggests more phonon scattering.

In the case of our H-intercalated sample, the mobility extracted is $\mu = 700cm^2/V \cdot s$. From the Hall statistics it can be seen that this low mobility corresponds to a relatively high carrier density of $2.0e13cm^{-2}$. Substituting these numbers, one finds that $\epsilon_{SO} \approx 115meV$. This is in good agreement with experimental measurements of ϵ_{SO} in SiC [53, 70, 71]. The important point here is that the dominant contribution to the low field mobility in H-intercalated material is from impurity scattering. When n very high, it can be assumed that low field mobility is constant with temperature. In this case, one can directly calculate v_{sat} given n based on the knowledge that $\epsilon_{SO} \approx 115meV$ in 4H-SiC and 6H-SiC. From Eq 3.23, it is clear that the expected v_{sat} should vary inversely with $\sqrt{n}$. The plot below shows the extracted v_{sat} as a function of temperature for both as-grown and H-intercalated material. The solid line shows the full temperature dependent model in the case of an impurity limited low field mobility. The case of as-grown material is interesting. Although the model gives a correct qualitative description of the temperature dependence in the velocity, the SiC phonon energy predicted is $\epsilon_{SO} \approx 95meV$ which is in disagreement with the expected values. This may be understood by noting that the mobility in the as-grown material decreases strongly with temperature (Fig. 3.20) such that the ϵ_{SO} model cannot be applied. Ultimately, the temperature dependence in the velocity is an artifact of decreasing mobility at higher temperatures. Specifically acoustic phonons are also playing a role in generating v_{sat}. In the case of H-intercalated material, there is no strong dependence of μ on temperature suggesting that only the optical phonons are responsible for saturation.

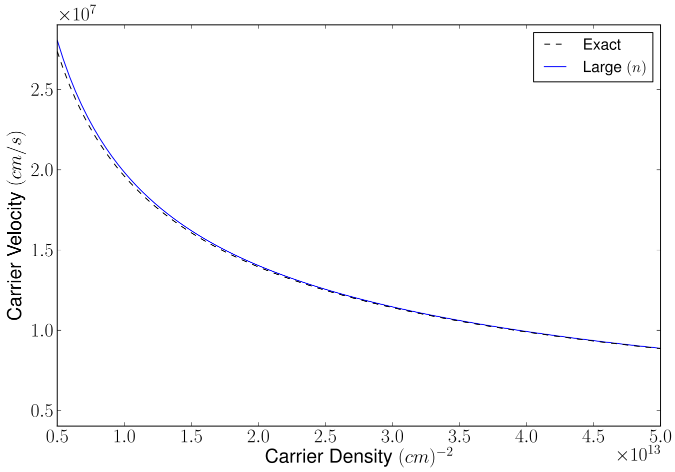

Figure 3.22: A plot of the exact (dashed) and large carrier density approximated (blue) theoretical saturated velocity dependence on carrier density for the case of impurity scattering. All H-intercalated materials measured suggest high impurity densities. *Thus the above plot indicates the expected saturation velocity and thus the expected limit on high frequency performance for gated structures* ($f_t = v_{sat}/2\pi l_g$).

The ϵ_{SO} model is very convenient in the case of H-intercalated material insofar as one can directly predict the saturated velocity v_{sat} simply by performing a simple measurement of the carrier density. The assumption one is making in doing so is that $\mu(T)$ is constant. In the typical case of a carrier density of $n = 1e13$ one expects a saturated velocity of $v_{sat} = 2e7cm/s$. This value is not exceedingly high, and it compares with that of other advanced semi-conductor materials. Figure 3.22 shows the predicted low temperature saturated velocity as a function of carrier density in the case where transport is limited by the surface mode in SiC. The carrier densities shown are those typically observed in H-intercalated samples. The exact model at $T = 300K$ (Eq. 3.21) and large carrier density approximation (Eq. 3.23) are shown. Immediately, one can see a problem for the use of H-intercalated material for high speed devices. One is challenged to find a H-intercalation process which does not introduce a high density of impurities into the graphene layer as higher electron velocities may only be observed in the phonon scattering limit. It should be noted that in the low carrier density/low temperature limit $v_{sat} \to 2v_f/\pi$.

3.4 DC Hysteresis and Time Dependent Phenomena

DC measurements are quite informative in terms of the material properties. Based on the material presented to this point, one expects that a graphene sheet will behave as a normal Ohmic conductor. In this way, the low field IV curve is expected to be linear in the low field regime. However, early measurements on graphene mesas reveal a very interesting hysteresis effect which has of yet not been fully understood [52, 72]. The plot below shows this hysteresis effect for six $2x50\mu m^2$ TLM structures. Three structures are measured on the as-grown material (left), and H-intercalated material (right) [52].

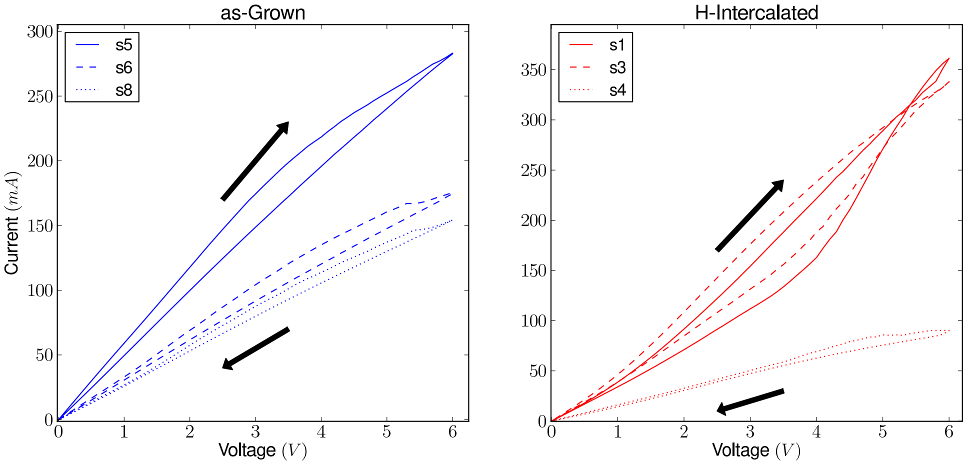

Figure 3.23: DC hysteresis measurements of as-grown (left) and H-intercalated (right) materials. The DC hysteresis is usually observed in epitaxial graphene samples. The hysteresis is generally symmetric about $V = 0$. Its origin is currently under investigation.

For these samples, both the as-grown and H-intercalated materials show a variation in the sheet resistance reflecting the intrinsic variation in the graphene over the surface of the substrate. What is unexpected is that the current during *loading* and *unloading* is significantly different. Hystereses are observed in most graphene samples, though the area enclosed by the loading and unloading traces can differ significantly.

As stated previously the origin of the hysteresis is unclear. It may lie in trap induced non-linearities, or it may be reflect a temperature dependent conductivity. The hysteresis was the original inspiration behind the strategy of pulsed measurements. For short pulse lengths $< 2\mu s$ no hysteresis is observed, while at long pulse lengths the phenomenon begins to appear. The phenomenon may be qualitatively understood in terms of the impurity scattering lifetimes. On the loading curve there appear to be less impurities, while on the unloading curve there appear to be more. Thus during loading, one may assume that carriers are vacated from charged impurity sites, while during unloading, carriers are trapped at impurity sites. The charged impurity density is then lower during loading and higher during unloading. The hysteresis effect is always symmetric about $V = 0$. Such a non-linear effect is very important to be aware of from a device perspective, and will give significant distortion for large signals applied across a graphene mesa.

Chapter 4

Processing Technology

In order to probe the physics of graphene on SiC, a tremendous amount of effort has gone into developing a method of fabricating devices and test structures. The most difficult aspect of processing on graphene is working around the graphene layer itself. Early experiments indicated that processing generally can have a strong effect on the overall transport measurements of both as grown and H-intercalated graphene. In this way, it was decided that the best way to process on graphene was to passivate the material from the beginning. However, passivation itself has proven difficult, as it introduces a second interface. This has a tendency to introduce additional complexity into theoretical models as both the graphene/SiC and the graphene/SiC interface need to be taken into account.

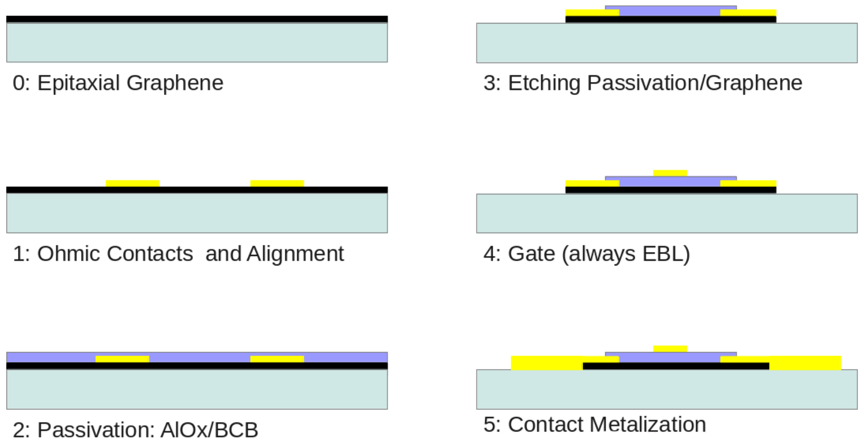
0: Epitaxial Graphene
3: Etching Passivation/Graphene
1: Ohmic Contacts and Alignment
4: Gate (always EBL)
2: Passivation: AlOx/BCB
5: Contact Metalization

Figure 4.1: A general schematic of the process flow used for the fabrication of transistors and test structures on epitaxial graphene.

The general scheme for processing begins with a passivation step and the pattering of Ohmic contacts. Patterning is done by one of three processes: Electron Beam Lithography, Photolithography, and Deep UV Photolithography. The last of these processes is still in the development phase and no conclusive results have been procured. Ohmic contacts are usually patterned prior to passivation as pattering them after introduces an additional etching step. It is desired that the Ohmic contacts are placed directly onto the graphene layer as they are the most critical step. Following these preliminaries, an etching step is performed to isolate active areas of graphene. Then gates are patterned (if required) *. Finally, contact metalization is performed. The general scheme of processing is outlined in Figure 4.1.

Here, the epitaxial layer is shown in black, and the SiC substrate in blue. Passivation is violet, and metalization steps are shown in gold. Generally, metalization is performed via electron beam evaporation and is (Ti/Pt/Au) for the Ohmic contacts and (Ti/Au) for all other steps. The exact process will vary depending on the devices and test structures being processed. What follows below should serve as a general description of the processing procedure that has been developed for epitaxial graphene on SiC.

4.1 Details on Processing

It is helpful to outline the specifics of proceeding in order to gain insight into some of the considerations which must be taken into account when working with graphene. Because the properties of graphene can change during processing, each step must be engineered in order to isolate the surface from processing environments. Passivation also plays a critical role in measurement, as atmospheric water vapor and contaminants can have deleterious effects on unpassivated graphene layers. It is of particular importance to avoid the deposition of resist directly onto the graphene. Early processes utilized C_8H_8 Benzocyclobutene (BCB) as a passivation layer, while later processes rely on Al_2O_3 passivation by thermal oxidation of Al. Future experiments will utilize Atomic Layer Deposition of Al_2O_3 in a H_2O atmosphere for passivation.

4.1.1 Surface Characterization

The epitaxial graphene surface is far from smooth, and surface imaging by SEM and AFM are powerful tools for generating a sense of how the surface looks.

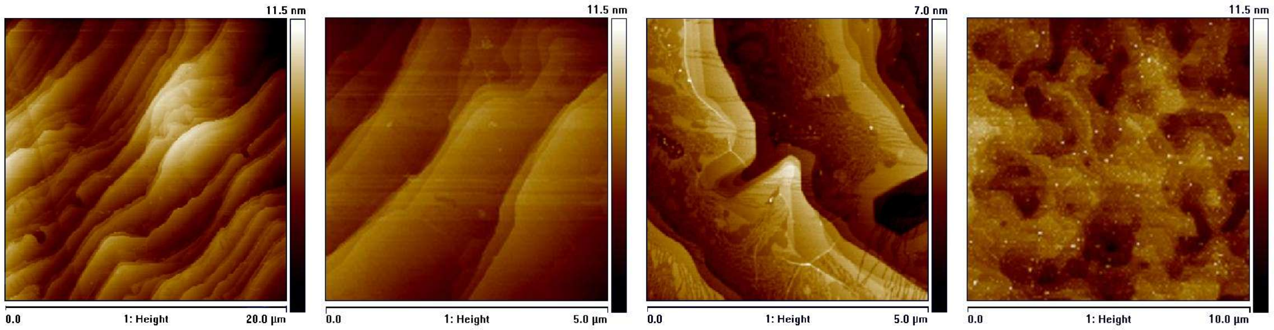

Figure 4.2: Four AFM images showing from left to right: a large area image of an H-intercalated sample, a smaller area of the same sample, a second H-intercalated sample, and an as-grown sample.

What is striking about these images is that the H-intercalated samples typically show a strongly terraced surface structure. At terrace junctions, the continuity of the epitaxial layer is broken. Most of the impurities and lattice defects are likely introduced at these boundaries between terraces. On terraces, the graphene layer is thought to be uniform. The step height of each terrace determines the minimum thickness of passivation which must be grown. In most cases, $10nm$ of passivation should be sufficient, as the terrace height is on the order of a $3 \sim 5nm$. It is also interesting to consider that the as-grown sample does not

---

* All of the results presented in the preceding chapter are for *ungated* devices

exhibit the terracing effect, and instead the surface appears to be highly irregular. From the perspective of growth, one can see that the H-intercalated surface is more uniform. This the possibility of fabricating devices such that they live on or are aligned to terraces in order to improve transport properties.

SEM imaging is another powerful tool for examining the surface morphology of graphene. Again the dependence on growth conditions is evident by examining in the images. The images below show two samples grown in different conditions. Figure 4.3 shows a sample with very wide terraces. The terrace width on the order of $10\mu m$. This sample is also interesting as it demonstrates a very obvious spiral dislocation. Figure 4.3 shows another sample with much more closely packed terraces. In the second sample the terrace width is on the order of $1\mu m$. Both samples were in-situ intercalated with Hydrogen.

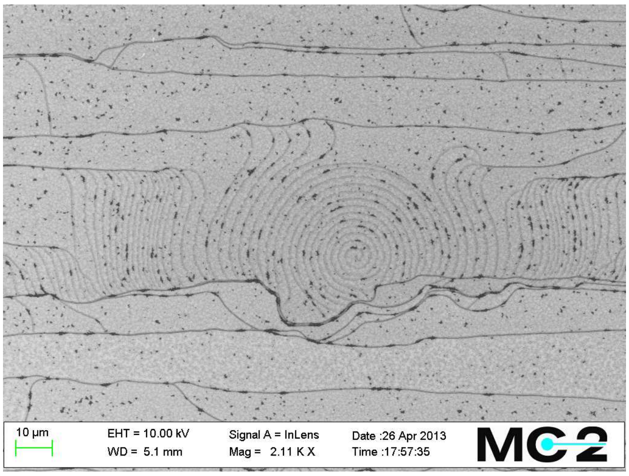

Figure 4.3 *(left)*: A low resolution SEM image of an epitaxial sample with wide terraces grown via a CVD technique

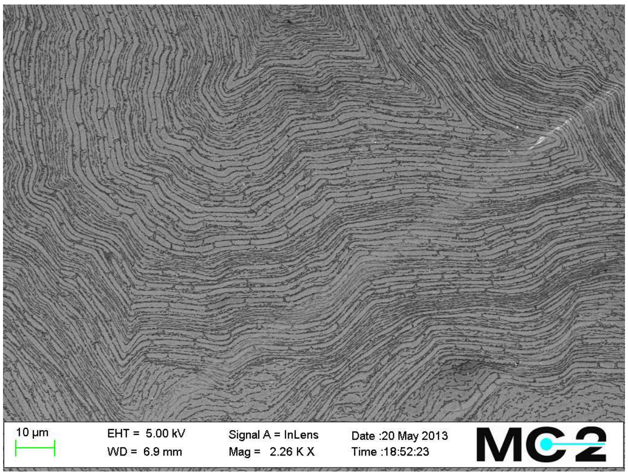

Figure 4.4 *(right)*: A low resolution SEM image of another CVD sample shown with narrow terraces.

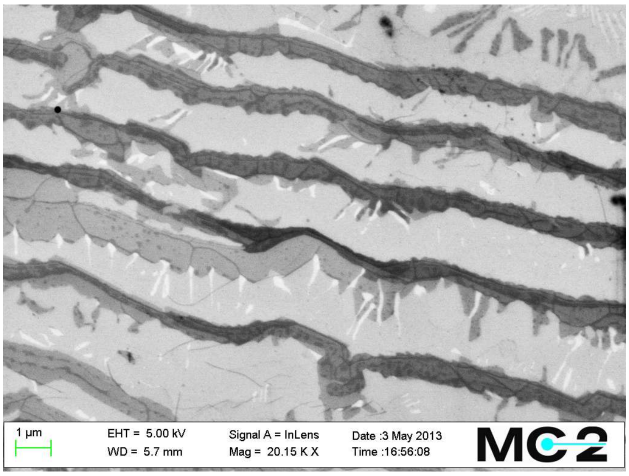

Figure 4.5 *(left)*: A high resolution SEM image of the sample shown in Figure 4.4

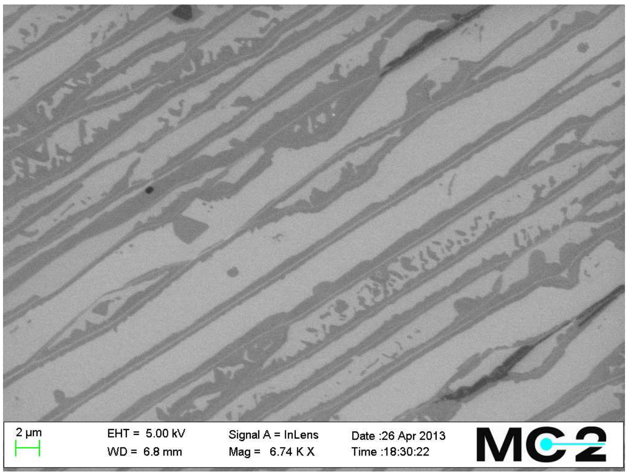

Figure 4.6 *(right)*: A third sample grown via high temperature sublimation in vacuum.

Regarding the second sample, more images were taken at higher magnification (Figure 4.5). This reveals that the terraces are locally parallel, as in the AFM images shown previously. The thickness of the graphene layer can be qualitatively ascertained by examining the darkness of the image, such that one may conclude that the epitaxial layer tends to be thicker near terrace edges.

Figure 4.6 shows an as-grown sample grown by high temperature *sublimation* in vacuum. This sample is morphologically similar to the sample on the left which was grown in a high temperature hot-wall CVD reactor. In the case of the sublimated material, the graphene appears to be more uniform and the thickening of the edges is still observed on this region of the sample. The essential conclusion that needs to be understood by virtue of these images is that the surface of epitaxial graphene is hardly uniform. While the first order physics presented earlier will still give reasonable results, the non-uniformity of the substrate, both in the manner of introducing defects and by introducing non-uniformity in the number of layers can significantly influence device performance. As a simple example, one can infer that there will be an anisotropy in transport properties. One expects better performance in devices aligned parallel to terraces than ones aligned normal to terraces. This in turn introduces a large number of experimental possibilities in working with epitaxial graphene.

4.1.2 Electron Beam Lithography

The EBL patterning steps are all performed with the JEOL JBX-9300FS EBL system. The EBL process begins with the evaporation of $2nm$ Aluminum. This seed layer is then thermally oxidized at $170°C$ for 5min to provide a seed layer of Aluminum Oxide. The AlOx layer also functions as a passivation layer in order to protect the graphene from atmospheric degradation and later processing steps. Processing begins with the patterning of alignment marks and Ohmic contacts with EBL. A bi-layer of $80 : 500nm$ MMA(EL10)/PMMA(A2) is deposited in two steps via spin coating at $3000rpm$ and curing at $170°C$ for $5m$. After exposure, the pattern is developed in a 1:1 solution of MIBK:IPA. The thin native oxide is then etched in a diluted 1:10 solution of BOE:DI. Next, a metal stack of $10 : 10 : 50nm$ of $Ti/Pt/Au$ is deposited via evaporation or DC sputtering and liftoff. The mesa isolation layer is patterned using negative mode resist. A layer of ma-N 2401 is spin coated onto the substrate at $3000rpm$ for $30s$ and cured at $110°C$ for $60s$. After exposure the mesa pattern is developed in ma-D 525 for 50s. The graphene layer is then etched in an O_2 plasma for $60s$ at a pressure of $250mTorr$.

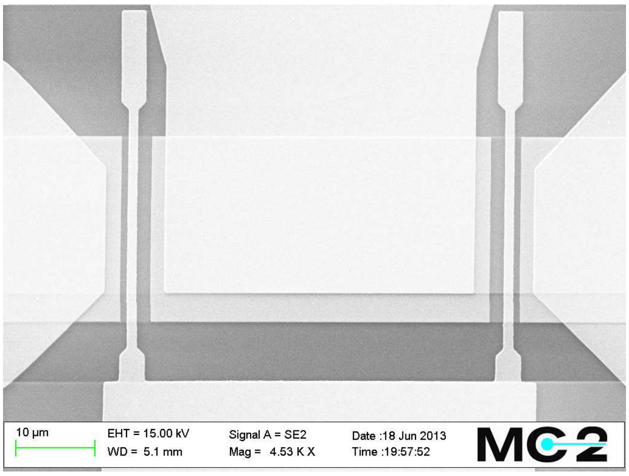

Figure 4.7: A secondary electron SEM image of a transistor fabricated via EBL. This should be compared with Figure 4.1 in connection each general processing step.

Next a thicker AlOx passivation layer $7 \sim 10nm$ is built up via many thermal oxidation steps in order to serve as a crude field oxide. Gates are deposited in a high resolution EBL process. The thickness of the field oxide is chosen in order to achieve step coverage of the intrinsic terracing of the SiC substrate which occurs during graphene growth. If gated structures are needed, A bi-layer of $150 : 500nm$ of ZEP/UV5 is spin coated onto at $2000 : 5000rpm$ respectively the samples and cured at $170°C$ in two steps. Then gates with T geometry and L geometry are patterned using multiple EBL shot ranks. After exposure the a post exposure bake is performed at $130°C$ for $90s$. Care must be taken to minimize the time between exposure and post exposure baking. The UV5 is then developed in MF24-A for $60s$ and a subsequent ashing in $50W/250mTorr$ O_2 plasma is performed. The ZEP layer is developed in o-Xylene for $2m$ and a subsequent low pressure directional ashing $50W/10mTorr$ is performed. The directional etch step attempts to preserve the aspect ratio of the EBL process as it is desirable maintain $100nm$ resolution for narrow gate lengths. Finally a thick contact metalization step is performed in the same manner as the initial Ohmic contact steps via evaporation or DC sputtering. For the metal layer, a $10 : 500nm$ Ti/Au stack is used. In all cases the Ti layer functions as an adhesion layer and the Au layer functions as the primary conductor. In the case of the Ohmic contacts the intermediate Pt layer is used to create a graded work function across the contact. The exposure dose in all cases is $300uC/cm^2$ with the exception of the gate step. Figure 4.7 shows a gated device after EBL processing.

4.1.3 Photolithography

The photolithography (PL) processing occurs in direct analogy to the EBL processing. The alignment marks, mesa, Ohmic, dielectric etch, and contact metalization steps are all performed via photolithography. If gated devices are needed, then the pattering of gate step is performed in a manner identical to the EBL process as it is desirable to have narrow gate lengths for the PL transistor structures. [*] The PL process begins with the same $2nm$ native oxide protection step as was done during the EBL process. All photolithography steps are carried out with a KS MJB3-UV 400 contact photolithography system.

The first step involves the pattering of a Ti anti reflection frame via PL and liftoff. This step has been found to be necessary to obtain $2\mu m$ resolution with the PL method. The need for this arises from the fact that SiC substrates are transparent such that scattered light can can cause significant parasitic exposure of photoresist. Furthermore, every PL step is accompanied by an edge removal step in order to obtain good contact between the pattern mask and the sample. A three step cleaning is performed between each lithography step in Acetone/Methanol/IPA for $5m$ each.

Processing of the test structures then begins with by spin coating AZ-5214E image reversal photoresist at $5000rpm$ for $60s$. The resist is then cured at $110°C$ for $75s$. The alignment pattern is exposed with a dose of $5mW/cm^2$ for $2.5s$. Then the sample is then quickly baked at $120°C$ for $75s$ in order to reverse the image. Following this step is a flood exposure for 60s. The pattern is then developed in a dilute $1 : 5$ solution of AZ-351B developer:DI for $30s$. The alignment marks are then metalized via evaporation or DC sputtering. One important difference between the EBL and PL process is that the AZ-351B developer solution etches the thin native oxide layer protecting the graphene such that pattern development comes with an in-situ etching.

Next, the isolation step is performed via by utilizing AZ-5124 in positive mode. Resist is spin coated onto the sample and cured as in the previous step, and the pattern is exposed with a dose of $5mW/cm^2$ for $10s$. Development proceeds as before. The subsequent Ohmic contact step is performed in a similar manner as the alignment marks with the exception of an additional 5min cleaning step in $CHCl_3$ in order to remove resist residues that exist on the surface. This step is not entirely necessary, but it is thought to be beneficial.

Next, a thicker oxide is deposited by multiple oxidation as during the EBL step. Again $7 \sim 10nm$ of AlOx is deposited in order to ensure step coverage of the SiC surface geometry. Following this procedure, the gate is patterned as described in the EBL process. Finally, contact metalization is performed via PL in the

---

[*] Though results on gated structures are not reported in the previous sections, gated structures will become increasingly important in future work

same manner as the Ohmic contact steps. It should be noted that the field oxide is etched in a solution of 1:10 solution of BOE:DI prior to metalization. In all cases the thickness and types of the metals deposited are identical to those of the EBL process.

4.1.4 BCB Processing

BCB passivation is a potential alternative to passivation with Al_2O_3 in the event that ungated devices are needed. BCB passivation typically takes place after the formation of Ohmic contacts as in the previous processes. One can think of this process being substituted for the growth of the thicker Al_2O_3 passivation layer in the PL and EBL processes. Also, the BCB process is compatible with both PL and EBL processes.

BCB is first diluted in $[1, 3, 5]$-trimethylbenzene $[C_6H_3(CH_3)_3]$ in a $1 : 5$ ratio in order to reduce its viscosity. This dilution step is necessary in order to create a thinner passivation layers of BCB. BCB is spun onto the substrate and cured at $250°C$ for $2.5h$ in a N_2 atmosphere. [73] Next, either EBL resist or PL resist is spun onto the substrate as before, and a $50nm$ Cr hard mask is deposited via evaporation. Following evaporation, the BCB is etched in a $1 : 9$ mixture of $CHF_3 : O_2$ at $50W/50mTorr$ for about $1m$. This leaves the BCB covering only the graphene mesa areas. Finally the Cr hard mask is etched in a $1 : 10$ ratio of $(NH_4)_2Ce(NO_3)_6 : H_2O$ for approximately $3m$.

The effect of BCB can be seen by examining the plot below, which shows the Hall statistics before and after the passivation processing. Sheet resistance is plotted against the *inverse* of the carrier density. The black trace indicates a fitting to the mobility. The data shown here was extracted from the as-grown sample shown on which the temperature dependent velocity field characteristic was measured.

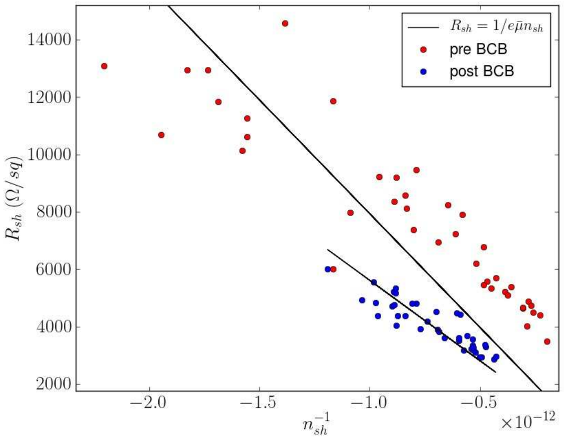

Figure 4.8: Hall statistics taken on a sample before and after deposition of BCB. These statistics are of the same nature as those shown in Figure 3.12.

In this experiment, BCB improves sheet resistance and uniformity properties. These improvements may originate in a surface interaction between the BCB and the graphene layer or they may be an artifact of the heat treatment of BCB. In either case, BCB demonstrates excellent chemical resistance and serves as an adequate passivation both from later process environments and from atmospheric contaminants.

4.2 Contact Resistance and Transport

In addition to providing information about the physics of graphene, contact resistance and transport measurements may also be used in order to assess the success of processing. Hall statistics can provide insight into the uniformity of the sample, and contact resistance measurements yield information which is crucial for accurate measurements of the saturated velocity and electron device models. The measurement of the contact resistance is done via the *Transfer Length Method* (TLM). Graphene mesas are fabricated and the length is varied between the contacts. TLM devices can be fabricated in either series or parallel configurations. The IV characteristic is measured at low voltages in order to extract the total resistance of each structure. In order to avoid the aforementioned hysteresis effects, low voltages are preferred in TLM measurements. Generally one has the following by Ohms law.

$$V = I\left[2R_c + R_m(l)\right] \tag{4.1}$$

Here l is the length between the contacts and $R_m(l)$ denotes that the mesa resistance varies with the length between the contacts. Now, $R_m(l)$ may be expressed in terms of the sheet resistance ρ_{sh} which is assumed to be constant for all structures measured. Note that this assumption can introduce problems in the case of graphene as the sheet resistance can vary from point to point on the substrate. In this case, many structures are measured in order to determine an average sheet resistance, and a range on the contact resistance. Substituting in the sheet resistance, one finds.

$$R = \left(2R_c + \rho_{sh}\frac{l}{w}\right) \tag{4.2}$$

Generally the length l is the parameter which is varied. It is also possible to vary the width of the contacts w to obtain similar results. Differentiating resistance with respect to the length, one finds that the slope yields the sheet resistance.

$$\frac{\partial R}{\partial l} = \frac{\rho_{sh}}{w} \tag{4.3}$$

And evaluating Ohms law at $l = 0$ gives the total contact resistance.

$$R(0) = 2R_c \tag{4.4}$$

The contact resistance is often defined in terms of a resistivity in units of $\Omega \cdot mm$ in which case one has $\rho_c = wR_c$. It is convenient to express the IV characteristic in terms of the number of squares $s \equiv l/w$.

$$V = I\left(\frac{2}{w}\rho_c + \rho_{sh}s\right) \tag{4.5}$$

The point at which the IV characteristic crosses the y-axis gives the contact resistance, and the slope of the IV characteristic gives the sheet resistance.

4.2.1 A Case Study: EBL Sample

The plots below shows the contact resistance and sheet resistance of an H-intercalated sample after fabrication. The TLM extraction is done on multiple structures giving a range on the contact and sheet resistances.

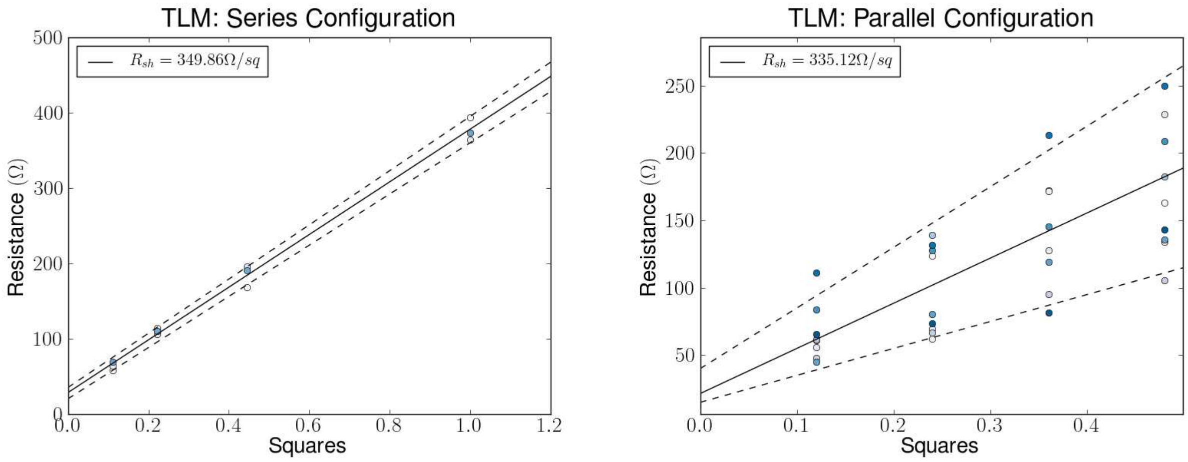

Figure 4.9: TLM measurements of both series oriented (left) and parallel oriented (right) structures. The data presented here indicates the most linear set of a large series of measurements. The above data many be used to estimate the contact resistance shown in Figure 4.10.

The TLM extraction for the data above gives the following contact resistances and sheet resistances for several individual structures. Also is shown the entropy of the linear fit where higher entropies designate structures which are less linear due to variations in ρ_{sh} from structure to structure.

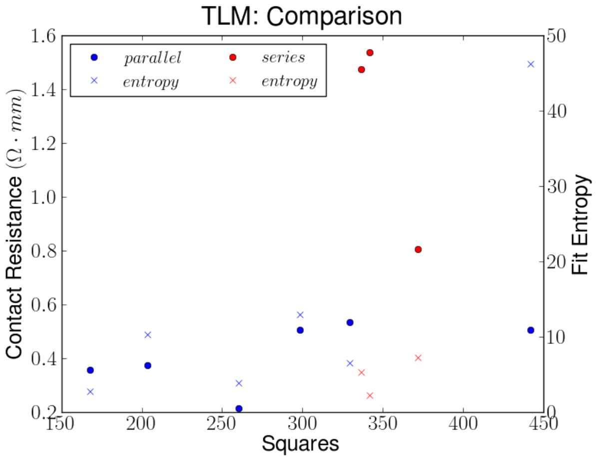

Figure 4.10: Extracted contact resistances from the measurements presented in Figure 4.9. The contact resistance is generally observed to be $< 1\Omega \cdot mm$ with values as low as $0.2\Omega \cdot mm$ being observed on this sample. Values of $< 0.1\Omega \cdot mm$ have been measured and reported in the literature.

The contact resistance generally seems to be lower in the case of parallel configuration structures. This may be an artifact of the processing or a reflection of lower total contact area for the series structures than for parallel structures. For parallel configuration contacts, the contact resistance is reliably between $0.2 \sim 0.5\Omega \cdot mm$. This particular sample was processed via EBL. Generally for EBL fabricated samples, the contact resistance is lower. Values of $< 0.1\Omega \cdot mm$ have been achieved which are comparable to state of the art experiments [74]. PL fabricated samples tend to demonstrate higher contact resistances from $1.0 \sim 2.5\Omega \cdot mm$ [53]. This effect is likely attributed to residues from photoresist. Future experiments on DUV processing will aim to enjoin the EBL like contact resistances with the high throughput of an optical technique.

4.2.2 Annealing, Transport, and Contact Resistance

In this particular process run, an annealing step was performed after fabrication in order to attempt to alleviate the poor contact resistances and sheet resistances found in initial measurements. Annealing steps are not always needed, but in the case where transport properties and poor and TLM measurements are non-linear it may be possible to improve the sample significantly by annealing [3]. The plot below shows the Hall statistics of the EBL sample presented in the previous section.

Prior to annealing, one can see that this H-intercalated sample demonstrates low carrier densities and high sheet resistances. The mean mobility (shown by the black curve) is $\bar{\mu} \sim 2140 cm^2/V \cdot s$. The sample is then annealed at $400°C$ for 30 minutes in a mixture of $1:9$ mixture of $H_2 : Ar$ forming gas. After annealing the carrier density recovers to levels expected of H-intercalated material. The mobility after annealing is unchanged. The sample uniformity (as seen by the amount by which the statistics deviate from the mean mobility curve) is also unchanged after annealing.

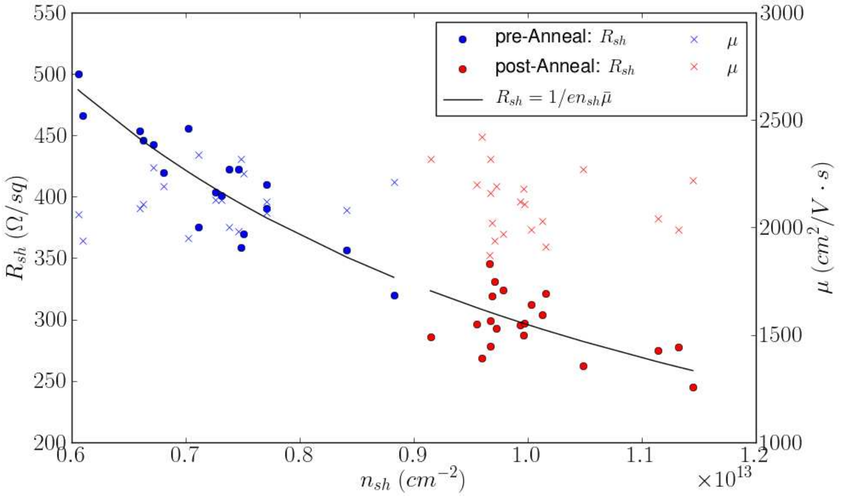

Figure 4.11: The measured Hall statistics on an H-intercalated EBL fabricated sample before and after annealing. The Hall statistics indicate that annealing had a profoundly positive effect on the uniformity of this sample.

The plots in the previous section all show the results after annealing. The TLM data is highly linear and the contact resistances are very low. The sheet resistances observed in the previous section are fairly uniform, and correlate well to the post annealing points in the plots above. These results should be considered in the context of the Figure 4.12, which shows TLM measurements on parallel configuration devices before annealing. Before annealing, there are no linear devices indicating a highly variable sheet resistance from structure to structure. Furthermore, the TLM measurements give a very wide range on the contact resistance as indicated by the dashed red lines. In the case of this sample, annealing was highly beneficial.

Generally speaking, an annealing step is not needed in order to achieve good contact resistance. However, it is thought to be helpful in cases where the contact metalization is poor.[3] An annealing step serves to bring metal atoms at the Ohmic contact into equilibrium proximity to the graphene sheet. Furthermore, annealing has also been demonstrated to improve adhesion of metal contacts to graphene. Annealing in this context may be a good idea. While adhesion of metal to SiC is generally reliable, experience has shown that its adhesion to graphene can be quite poor. Generally, it is thought that there is no incorporation of metal into a pristine graphene lattice, such that the electronic properties of the graphene are more or less preserved after the deposition of contact metalization.

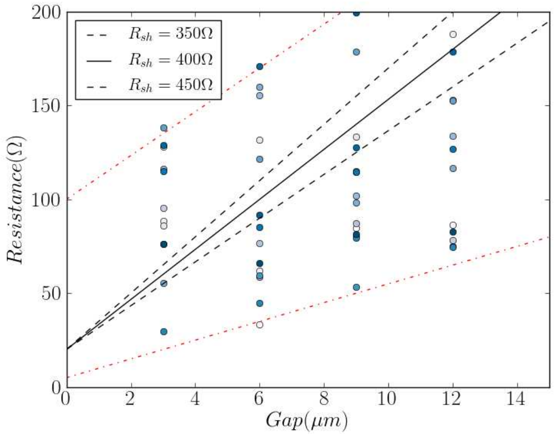

Figure 4.12: The measured TLM data from the data presented in Figure 4.11 before annealing. Due to the poor uniformity, it is not possible to estimate the contact resistance. This should be compared to the case after annealing presented in Figure 4.9 in which respectable contact resistance was achieved.

Afterword

A general overview of the physics of electron transport in graphene has been presented. Our initial work was focused on consolodating the fundamental physical theory of graphene. This was primarily done as in order to provide a solid foundation from which to interpret experimental results. The phonon spectrum was derived to first order which was later reintroduced when considering Raman spectroscopy and the assessment of the number of layers of a given epitaxial layer. A tight binding model was introduced for electron wavefuncitons, yielding the band structure of monolayer graphene. Much of the scientific interest in graphene can be understood as being fundamentally related to understanding the physical consequences of such a band structure in the context of electron devices.

Next, the problem of monolayer graphene was expanded in order to investigate the theoretical properties of a bilayer. It was seen that the physical properties of a bilayer are very different from those of a monolayer. Of particular interest is the possibility of opening a band gap via the application of a vertical electric field. The vertical electric field was observed to break the symmetry of the low energy Hamiltonian giving the possibility of exotic electron devices in a bilayer. Then the Boltzmann transport equations were solved and the case of impurity scattering and acoustic phonon scattering were described in detail, thereby providing powerful insight into what is expected in terms of high temperature transport properties. Many of these properties have been duly confirmed in experimental measurements of the temperature dependence of the carrier mobility.

Experimental work on layer counting/mapping was shown for several epitaxial samples, and data from velocity-field measurements was presented. A simple theoretical description of the graphene/SiC system was also introduced, and several comments were made regarding deviations from the purely theoretical model. The velocity field measurements also included much in the way of transport statistics which in turn was interpreted as a quantitative measurement of the non-uniformity of epitaxial layers. Then the impurity scattering case of H-intercalated material was considered in terms of the velocity field measurements. Connecting these ideas, it was possible to derive a speed limit for electrons moving in highly doped H-intercalated epitaxial layers.

Finally, some comments on the fabrication of devices on graphene was outlined. This section is of vital importance, as without a viable processing technology, electrical measurements and characterization of epitaxial layers would be all but impossible. Also in this section a true picture of the substrate was introduced via AFM and SEM imaging of both as-grown and H-intercalated systems. The highly variable surface morphology of epitaxial substrates, should be understood as a possible origin of the quantitative description of non-uniformity. Finally, contact resistance measurements were presented via the TLM method as a precise knowledge of the contact resistance of test structures is important both for physical characterization and for the engineering of electron devices on epitaxial graphene.

It is useful to connect the measurements and analysis presented to the motivation towards high frequency electronics outlined in the preface. Substituting some optimistic values in expected for epitaxial graphene SiC of $\mu = 2000cm^2/V \cdot s$, $V_{ds} = 1V$ and $l_g = 40nm$ one finds that $f_t = 63GHz$. At higher drain-source voltages experiments show that device performance becomes unreliable due to hysteresis effects. Furthermore, experiments have shown that $V_{ds} = 1V$ is an optimal bias point for devices fabricated on exfoliated material on SiO_2 [75]. In H-intercalated material we have found a speed limit which may be deduced via consideration of remote phonon scattering via the substrate. One can expect $v_{sat} = 2e7$ for H-intercalated material. For $l_g = 0.5\mu m$ one finds that $f_t^{max} = 64GHz$. The H-intercalated speed limit thus severely limits the potential application of epitaxial graphene for high speed devices. It is important to note that the theoretical limit on v_{sat} is the Fermi velocity $v_f = 1e8cm/s$. * If one could attain $v_{sat} = v_f$ then one expects $f_t^{max} = 320GHz$, a quite respectable figure for long channel devices. The problem of the speed limit is immediately clear; in order to achieve $f_t = 320GHz$ short gate lengths are needed such that one introduces a host of processing and modeling related difficulties. $f_t > 300GHz$ has been demonstrated in nanoscale devices by Wu et. al. in exfoliated material on SiO_2 [76].

It is important to consider what is presented above is the expected upper limit on the *intrinsic* value of f_t. What one actually measures is the *extrinsic* f_t which incurs losses due to parasitic source and drain resistances. The output conductance g_d scales linearly with carrier density. In the case of highly doped graphene layers, then one finds the following

$$g_d = \frac{e\mu|n|}{l_g}$$

For H-intercalated epitaxial material, one has $|n| \approx 1e13cm^{-3}$ such that $g_d = 6.4S/mm$ in the context described above. Here R_s and R_d may be interpreted as the sum of the contact resistance and the parts of the active layer not influenced by the gate. Optimistic values obtained from TLM measurements and Hall measurements indicate that $R_s = R_d = 0.1\Omega \cdot mm$ such that one can expect that the maximum *extrinsic* $f_{t,ext}^{max} = 28.0GHz$. The speed limit severely restricts the potential of graphene on SiC. Other work on exfoliated graphene have shown $f_{t,ext}^{max} = 150GHz$ with lower carrier densities and a speed limit of $v_{sat} \approx 4.1cm/s$ [75]. These results should also be considered in the context of recent work on GaN in which $f_{t,ext}^{max} = 454GHz$ was achieved. [77]. Even better performance ($f_t = 688GHz$, $f_{max} = 800GHz$) has been reported on $40nm$ gate length $In_{0.7}Ga_{0.3}As$ MHEMTs [78].

Table A.1: A comparison of f_t and f_{max} which have been realized for various device technologies. The gate length l_g is also reported as a rough indication of scaling. f_t and f_{max} are reported in (GHz), and l_g is reported in (nm). For the DHBT the the emitter base width is reported [79]. Graphene results are for epitaxial graphene on C-face SiC.

	epi-Graphene[80]	GaN HEMT [77]	$In_{0.7}Ga_{0.3}As$ HEMT [78]	InP DHBT [81]	Si CMOS [82]
f_t	110	450	668	551	170
f_{max}	70	440	800	1150	140
l_g	100	20	40	130*	90

While an electron mobility of $2000cm^2/V \cdot s$ is sufficient for achieving reasonable high speed performance, graphene suffers from lower than expected values of v_{sat}, high n, and low g_m due to the lack of a bandgap. Slightly higher saturated velocities are achievable in as-grown epitaxial graphene, but one here trades a bit of electron velocity with poor uniformity characteristics. Despite its attractiveness, epitaxial graphene has a long way to go before it will be able to compete with existing technologies.

As much that was done remains to be done on working with epitaxial layers. It is of particular interest to begin work with gated devices specifically on graphene bilayers owing to its potential field dependent

---

[*] This value comes directly out of the tight binding model for graphene. Specifically, it is the derivative of the graphene energy momentum dispersion relation for electrons.

band gap. By a clever back gating scheme it is, in theory, possible to have a graphene device with switching capabilities. This could be realized by growth of a lowly doped SiC layer prior to graphene growth. Also, further work on the velocity field characteristic is needed in conjunction with a careful in-situ characterization of the uniformity, quality, and number of graphene layers. By coupling experimental knowledge of the electron transport properties with accurate physical models it becomes possible to clearly assess epitaxial graphene in its potential application in a device context. Hysteresis effects also need to be understood in detail by detailed measurements of transport at both low and room temperature, and an accurate physical model of metal/graphene contacts needs to be purveyed. By combining all of these it then becomes possible to build quantitative small signal models of electron devices on epitaxial graphene.

Bibliography

[1] Yuan Taur and Tak K. Ning. Fundamentals of modern vlsi devices. 2009.

[2] J. Liou F. Schwierz. *Modern Microwave Transistors; Theory, Design, and Performance*. Wiley Interscience, 1 edition, 2003.

[3] Joshua A. Robinson, Michael LaBella, Mike Zhu, Matt Hollander, Richard Kasarda, Zachary Hughes, Kathleen Trumbull, Randal Cavalero, and David Snyder. Contacting graphene. *Applied Physics Letters*, 98(5):053103, 2011.

[4] J.-S. Moon, D. Curtis, S. Bui, M. Hu, D.K. Gaskill, J.L. Tedesco, P. Asbeck, G.G. Jernigan, B. L. VanMil, R. L. Myers-Ward, Jr. Eddy, C.R., P.M. Campbell, and X. Weng. Top-gated epitaxial graphene fets on si-face sic wafers with a peak transconductance of 600 ms/mm. *Electron Device Letters, IEEE*, 31(4):260–262, 2010.

[5] J. Kedzierski, Pei-Lan Hsu, P. Healey, P.W. Wyatt, C.L. Keast, Mike Sprinkle, C. Berger, and Walt A. De Heer. Epitaxial graphene transistors on sic substrates. *Electron Devices, IEEE Transactions on*, 55(8):2078–2085, 2008.

[6] W. Strupinski, K. Grodecki, A. Wysmolek, R. Stepniewski, T. Szkopek, P. E. Gaskell, A. Gruneis, D. Haberer, R. Bozek, J. Krupka, and J. M. Baranowski. Graphene epitaxy by chemical vapor deposition on sic. *Nano Letters*, 11(4):1786–1791, 2011.

[7] J.-S. Moon, D. Curtis, M. Hu, D. Wong, P.M. Campbell, G. Jernigan, J. Tedesco, B. VanMil, R. Myers-Ward, C. Eddy, D. K. Gaskill, J. Robinson, M. Fanton, and P. Asbeck. Development toward wafer-scale graphene rf electronics. In *Silicon Monolithic Integrated Circuits in RF Systems (SiRF), 2010 Topical Meeting on*, pages 1–3, 2010.

[8] Edward McCann and Mikito Koshino. The electronic properties of bilayer graphene. *Reports on Progress in Physics*, 76(5):056503, 2013.

[9] J. Hass, R. Feng, J. E. Millán-Otoya, X. Li, M. Sprinkle, P. N. First, W. A. de Heer, E. H. Conrad, and C. Berger. Structural properties of the multilayer graphene/4h-SiC(000$\overline{1}$) system as determined by surface x-ray diffraction. *Phys. Rev. B*, 75:214109, Jun 2007.

[10] M. I. Katsnelson K. S. Novoselov T. J. Booth S. Roth Jannik C. Meyer, A. K. Geim. The structure of suspended graphene sheets. *Nature Letters*, 446:60–63, 2007.

[11] P. Lauffer, K. V. Emtsev, R. Graupner, Th. Seyller, L. Ley, S. A. Reshanov, and H. B. Weber. Atomic and electronic structure of few-layer graphene on sic(0001) studied with scanning tunneling microscopy and spectroscopy. *Phys. Rev. B*, 77:155426, Apr 2008.

[12] J.M. Ziman. *Principles of the Theory of Solids.* Cambridge University Press, 2 edition, 1972.

[13] A. C. Ferrari, J. C. Meyer, V. Scardaci, C. Casiraghi, M. Lazzeri, F. Mauri, S. Piscanec, D. Jiang, K. S. Novoselov, S. Roth, and A. K. Geim. Raman spectrum of graphene and graphene layers. *Phys. Rev. Lett.*, 97:187401, Oct 2006.

[14] L.A. Falkovsky. Phonon dispersion in graphene. *Journal of Experimental and Theoretical Physics*, 105(2):397–403, 2007.

[15] Rasmita Sahoo and RashmiRanjan Mishra. Phonon dispersion of graphene revisited. *Journal of Experimental and Theoretical Physics*, 114(5):805–809, 2012.

[16] C. Kittel. *Introduction to Solid State Physics.* John Wiley and Sons, 8 edition, 2005.

[17] Akin Akturk and Neil Goldsman. Electron transport and full-band electron-phonon interactions in graphene. *Journal of Applied Physics*, 103(5):053702, 2008.

[18] M. Srednicki. *Quantum Field Theory.* Cambridge University Press, 1 edition, 2007.

[19] G. Mahan. *Many Body Physics.* Plenum Publishers, 3 edition, 2000.

[20] A. H. Castro Neto, F. Guinea, N. M. R. Peres, K. S. Novoselov, and A. K. Geim. The electronic properties of graphene. *Rev. Mod. Phys.*, 81:109–162, Jan 2009.

[21] Gilles Montambaux Cristina Bena. Remarks on the tight-binding model of graphene. *New Journal of Physics*, 11(5), 2009.

[22] S. Reich, J. Maultzsch, C. Thomsen, and P. Ordejón. Tight-binding description of graphene. *Phys. Rev. B*, 66:035412, Jul 2002.

[23] S. Das Sarma, Shaffique Adam, E. H. Hwang, and Enrico Rossi. Electronic transport in two-dimensional graphene. *Rev. Mod. Phys.*, 83:407–470, May 2011.

[24] M. Houssa, G. Pourtois, V. V. Afanas'ev, and A. Stesmans. Can silicon behave like graphene? a first-principles study. *Applied Physics Letters*, 97(11):112106, 2010.

[25] M. Sprinkle, D. Siegel, Y. Hu, J. Hicks, A. Tejeda, A. Taleb-Ibrahimi, P. Le Fèvre, F. Bertran, S. Vizzini, H. Enriquez, S. Chiang, P. Soukiassian, C. Berger, W. A. de Heer, A. Lanzara, and E. H. Conrad. First direct observation of a nearly ideal graphene band structure. *Phys. Rev. Lett.*, 103:226803, Nov 2009.

[26] Thomas Seyller Karsten Horn Eli Rotenberg Aaron Bostwick, Taisuke Ohta1. Quasiparticle dynamics in graphene. *Nature Physics*, 3:36–40, 2007.

[27] S. V. Morozov2 D. Jiang1 M. I. Katsnelson3 I. V. Grigorieva1 S. V. Dubonos A. A. Firsov2 K. S. Novoselov, A. K. Geim1. Two-dimensional gas of massless dirac fermions in graphene. *Nature Letters*, 438, Nov 2005.

[28] K. S. Novoselov A. K. Geim. The rise of graphene. *Nature Materials*, 6(3):183–191, 2007.

[29] D.J. Griffiths. *Introduction to Quantum Meachics.* Pearson Prentice Hall, 2 edition, 2005.

[30] Cheol-Hwan Park and Nicola Marzari. Berry phase and pseudospin winding number in bilayer graphene. *Phys. Rev. B*, 84:205440, Nov 2011.

[31] Horst L. Stormer Philip Kim Yuanbo Zhang, Yan-Wen Tan. Experimental observation of the quantum hall effect and berry's phase in graphene. *Nature Letters*, 438:201–204, 2005.

[32] M. Cheli, P. Michetti, and G. Iannaccone. Physical insights on nanoscale fets based on epitaxial graphene on sic. In *Solid State Device Research Conference, 2009. ESSDERC '09. Proceedings of the European*, pages 193–196, 2009.

[33] Caglar Girit1 Zhao Hao Michael C. Martin Alex Zettl1 Michael F. Crommie Y. Ron Shen Feng Wang Yuanbo Zhang, Tsung-Ta Tang. Current saturation in zero-bandgap, top-gated graphene field-effect transistors. *Nature Letters*, 459:820–823, 2009.

[34] A. B. Kuzmenko, I. Crassee, D. van der Marel, P. Blake, and K. S. Novoselov. Determination of the gate-tunable band gap and tight-binding parameters in bilayer graphene using infrared spectroscopy. *Phys. Rev. B*, 80:165406, Oct 2009.

[35] Fengnian Xia, Damon B. Farmer, Yu-ming Lin, and Phaedon Avouris. Graphene field-effect transistors with high on/off current ratio and large transport band gap at room temperature. *Nano Letters*, 10(2):715–718, 2010. PMID: 20092332.

[36] Eduardo V. Castro, K. S. Novoselov, S. V. Morozov, N. M. R. Peres, J. M. B. Lopes dos Santos, Johan Nilsson, F. Guinea, A. K. Geim, and A. H. Castro Neto. Biased bilayer graphene: Semiconductor with a gap tunable by the electric field effect. *Phys. Rev. Lett.*, 99:216802, Nov 2007.

[37] James G. Champlain. A first principles theoretical examination of graphene-based field effect transistors. *Journal of Applied Physics*, 109(8):084515, 2011.

[38] E. H. Hwang and S. Das Sarma. Acoustic phonon scattering limited carrier mobility in two-dimensional extrinsic graphene. *Phys. Rev. B*, 77:115449, Mar 2008.

[39] K. I. Bolotin, K. J. Sikes, J. Hone, H. L. Stormer, and P. Kim. Temperature-dependent transport in suspended graphene. *Phys. Rev. Lett.*, 101:096802, Aug 2008.

[40] Tsuneya Ando. Screening effect and impurity scattering in monolayer graphene. *Journal of the Physical Society of Japan*, 75(7):074716, 2006.

[41] Laura B. Biedermann, Michael L. Bolen, Michael A. Capano, Dmitry Zemlyanov, and Ronald G. Reifenberger. Insights into few-layer epitaxial graphene growth on $4h$-SiC$(000\overline{1})$ substrates from stm studies. *Phys. Rev. B*, 79:125411, Mar 2009.

[42] A. Meyer I.G. Ivanov J.I. Flege S. Watcharinyanon J. Falta L.I. Johansson E. Janzen J. Hassan, C. Virojanadara. Surface evolution of 4h-sic(0001) during in situ surface preparation and its influence on graphene properties. *Materials Science Forum*, 157:740–742, 2011.

[43] J. Hass. *Structural characterization of epitaxial graphene on silicon carbide.* Georgia Institute of Technology, 1 edition, 2008.

[44] H Hibino, S Tanabe, S Mizuno, and H Kageshima. Growth and electronic transport properties of epitaxial graphene on sic. *Journal of Physics D: Applied Physics*, 45(15):154008, 2012.

[45] U Starke and C Riedl. Epitaxial graphene on sic(0001) and sic$(000\tilde{1})$.

[46] K. V. Emtsev, F. Speck, Th. Seyller, L. Ley, and J. D. Riley. Interaction, growth, and ordering of epitaxial graphene on sic0001 surfaces: A comparative photoelectron spectroscopy study. *Phys. Rev. B*, 77:155303, Apr 2008.

[47] Shudong Xiao Masa Ishigami Michael S. Fuhrer Jian-Hao Chen, Chaun Jang. Electronic properties and devices intrinsic and extrinsic performance limits of graphene devices on sio2. *Nature Nanotechnology*, 3:206–209, 2008.

[48] C. Coletti, K. V. Emtsev, A. A. Zakharov, T. Ouisse, D. Chaussende, and U. Starke. Large area quasi-free standing monolayer graphene on 3c-sic(111). *Applied Physics Letters*, 99(8):081904, 2011.

[49] C. Riedl, C. Coletti, T. Iwasaki, A. A. Zakharov, and U. Starke. Quasi-free-standing epitaxial graphene on sic obtained by hydrogen intercalation. *Phys. Rev. Lett.*, 103:246804, Dec 2009.

[50] C Riedl, C Coletti, and U Starke. Structural and electronic properties of epitaxial graphene on sic(0001)- a review of growth, characterization, transfer doping and hydrogen intercalation. *Journal of Physics D: Applied Physics*, 43(37):374009, 2010.

[51] C Virojanadara, A A Zakharov, S Watcharinyanon, R Yakimova, and L I Johansson. A low-energy electron microscopy and x-ray photo-emission electron microscopy study of li intercalated into graphene on sic(0001). *New Journal of Physics*, 12(12):125015, 2010.

[52] Michael Winters et. al. A dc comparison study between h-intercalated and native epi-graphenes on sic substrates. 129:175–191, 2013.

[53] M. Winters, J. Hassan, H. Zirath, E. Janzén, and N. Rorsman. A temperature dependent measurement of the carrier velocity vs. electric field characteristic for as-grown and h-intercalated epitaxial graphene on sic. *Journal of Applied Physics*, 113(19):193708, 2013.

[54] Vincent E. Dorgan, Myung-Ho Bae, and Eric Pop. Mobility and saturation velocity in graphene on sio[sub 2]. *Applied Physics Letters*, 97(8):082112, 2010.

[55] L. G. Cancado, A. Jorio, E. H. Martins Ferreira, F. Stavale, C. A. Achete, R. B. Capaz, M. V. O. Moutinho, A. Lombardo, T. S. Kulmala, and A. C. Ferrari. Quantifying defects in graphene via raman spectroscopy at different excitation energies. *Nano Letters*, 11(8):3190–3196, 2011.

[56] Axel Eckmann, Alexandre Felten, Artem Mishchenko, Liam Britnell, Ralph Krupke, Kostya S. Novoselov, and Cinzia Casiraghi. Probing the nature of defects in graphene by raman spectroscopy. *Nano Letters*, 12(8):3925–3930, 2012.

[57] L.M. Malard, M.A. Pimenta, G. Dresselhaus, and M.S. Dresselhaus. Raman spectroscopy in graphene. *Physics Reports*, 473(5–6):51–87, 2009.

[58] E.O. Sheybani, O.J. Mengshoel, and S. Poll. Removing spikes while preserving data and noise using wavelet filter banks. In *Aerospace Conference, 2010 IEEE*, pages 1–10, 2010.

[59] C. Canali, G. Majni, R. Minder, and G. Ottaviani. Electron and hole drift velocity measurements in silicon and their empirical relation to electric field and temperature. *IEEE Transactions on Electron Devices*, 22:1045–1047, 1975.

[60] I. Angelov, H. Zirath, and N. Rosman. A new empirical nonlinear model for hemt and mesfet devices. *Microwave Theory and Techniques, IEEE Transactions on*, 40(12):2258–2266, Dec.

[61] I.A. Khan and Jr. Cooper, J.A. Measurement of high-field electron transport in silicon carbide. *Electron Devices, IEEE Transactions on*, 47(2):269 –273, feb 2000.

[62] J. M. Barker, D. K. Ferry, D. D. Koleske, and R. J. Shul. Bulk gan and algan/gan heterostructure drift velocity measurements and comparison to theoretical models. *Journal of Applied Physics*, 97(6):063705, 2005.

[63] J. G. Ruch and G. S. Kino. Measurement of the velocity-field characteristic of gallium arsenide. *Applied Physics Letters*, 10(2):40–42, 1967.

[64] A.F. Yound B. Ozyilmaz P. Kim K. L.Shepard M. Inanc, M.Y. Han. Current saturation in zero-bandgap, top-gated graphene field-effect transistors. *Nature Nanotechnology*, 3(11):654–659, 2008.

[65] Massimo V. Fischetti, Deborah A. Neumayer, and Eduard A. Cartier. Effective electron mobility in si inversion layers in metal–oxide–semiconductor systems with a high-kappa insulator: The role of remote phonon scattering. *Journal of Applied Physics*, 90(9):4587–4608, 2001.

[66] D.K. Ferry. Transport in graphene on bn and sic. In *Nanotechnology (IEEE-NANO), 2012 12th IEEE Conference on*, pages 1 –5, aug. 2012.

[67] R S Shishir and D K Ferry. Velocity saturation in intrinsic graphene. *Journal of Physics: Condensed Matter*, 21(34):344201, 2009.

[68] S. Q. Wang and G. D. Mahan. Electron scattering from surface excitations. *Phys. Rev. B*, 6:4517–4524, Dec 1972.

[69] Zhun-Yong Ong and Massimo V. Fischetti. Theory of remote phonon scattering in top-gated single-layer graphene. *Phys. Rev. B*, 88:045405, Jul 2013.

[70] H. Nienhaus, T.U. Kampen, and W. Monch. Phonons in 3c-, 4h-, and 6h-sic. *Surface Science*, 324(1):L328 – L332, 1995.

[71] Aniruddha Konar, Tian Fang, and Debdeep Jena. Effect of high-k gate dielectrics on charge transport in graphene-based field effect transistors. *Phys. Rev. B*, 82:115452, Sep 2010.

[72] Hua Xu, Yabin Chen, Jin Zhang, and Haoli Zhang. Investigating the mechanism of hysteresis effect in graphene electrical field device fabricated on sio2 substrates using raman spectroscopy. *Small*, 8(18):2833–2840, 2012.

[73] G. Roelkens, D. Van Thourhout, and R. Baets. Ultra-thin benzocyclobutene bonding of iii-v dies onto soi substrate. *Electronics Letters*, 41(9):561 – 562, april 2005.

[74] J. S. Moon, M. Antcliffe, H. C. Seo, D. Curtis, S. Lin, A. Schmitz, I. Milosavljevic, A. A. Kiselev, R. S. Ross, D. K. Gaskill, P. M. Campbell, R. C. Fitch, K.-M. Lee, and P. Asbeck. Ultra-low resistance ohmic contacts in graphene field effect transistors. *Applied Physics Letters*, 100(20):203512, 2012.

[75] Graphene transistors author = Frank Schwierz, journal = Nature Nanotechnology, volume = 5, pages = 487-496, year = 2010, doi = doi:10.1038/nnano.2010.89, publisher = Nature Publishing Group.

[76] Yanqing Wu, Keith A. Jenkins, Alberto Valdes-Garcia, Damon B. Farmer, Yu Zhu, Ageeth A. Bol, Christos Dimitrakopoulos, Wenjuan Zhu, Fengnian Xia, Phaedon Avouris, and Yu-Ming Lin. State-of-the-art graphene high-frequency electronics. *Nano Letters*, 12(6):3062–3067, 2012.

[77] K. Shinohara, D.C. Regan, Y. Tang, A.L. Corrion, D.F. Brown, J.C. Wong, J.F. Robinson, H.H. Fung, A. Schmitz, T.C. Oh, S.J. Kim, P.S. Chen, R.G. Nagele, A.D. Margomenos, and M. Micovic. Scaling of gan hemts and schottky diodes for submillimeter-wave mmic applications, 2013.

[78] Dae-Hyun Kim, B. Brar, and J.A. del Alamo. ft = 688 ghz and fmax = 800 ghz in lg = 40 nm in0.7ga0.3as mhemts with gmmax 2.7 ms/um. In *Electron Devices Meeting (IEDM), 2011 IEEE International*, pages 13.6.1–13.6.4, 2011.

[79] Mark J W Rodwell, M. Le, and B. Brar. Inp bipolar ics: Scaling roadmaps, frequency limits, manufacturable technologies. *Proceedings of the IEEE*, 96(2):271–286, 2008.

[80] Zelei Guo, Rui Dong, Partha Sarathi Chakraborty, Nelson Lourenco, James Palmer, Yike Hu, Ming Ruan, John Hankinson, Jan Kunc, John D. Cressler, Claire Berger, and Walt A. de Heer. Record maximum oscillation frequency in c-face epitaxial graphene transistors. *Nano Letters*, 13(3):942–947, 2013.

[81] M. Urteaga, R. Pierson, P. Rowell, V. Jain, E. Lobisser, and M.J.W. Rodwell. 130nm inp dhbts with ft-0.52thz and fmax-1.1thz. In *Device Research Conference (DRC), 2011 69th Annual*, pages 281–282, 2011.

[82] S.P. Voinigescu, T.O. Dickson, R. Beerkens, I. Khalid, and P. Westergaard. A comparison of si cmos, sige bicmos, and inp hbt technologies for high-speed and millimeter-wave ics. In *Silicon Monolithic Integrated Circuits in RF Systems, 2004. Digest of Papers. 2004 Topical Meeting on*, pages 111–114, 2004.

Acknowledgement

I would like to acknowledge support from the Swedish Foundation for Strategic Research (SSF), the Knut och Alice Wallenberg Foundation (KAW), the European Science Foundation (ESF), and our collaborators within EPIGRAT. I also extend my personal gratitude to Herbert Zirath, Niklas Rorsman, Mattias Thorsell, Einar Örn Sveinbjörnsson, and Omid Habibpour for their enduring efforts to further our studies. Finally, I would like to thank Jawad Ul Hassan, Wlodek Strupinski, Rositsa Yakimova and Erik Janzén for providing a steady supply of high quality material for our experiments.